UNIVERSITY
OF OSLO

Vemund Stenbekk Thorkildsen

Resolution analysis and enhancement in geophysical imaging and inversion

Thesis submitted for the degree of Philosophiae Doctor

Department of Geosciences
Faculty of Mathematics and Natural Sciences

2023

Series of dissertations submitted to the
Faculty of Mathematics and Natural Sciences, University of Oslo
No. 2605

ISSN 1501-7710

Cover: UiO.
Print production: Graphics Center, University of Oslo.

To Kristine

Preface

This thesis has been submitted to the Department of Geosciences, Faculty of Mathematics and Natural Sciences at the University of Oslo (UiO) for the degree of Doctor of Philosophy. The research presented here is conducted under the main supervision of Professor Leiv-J Gelius and co-supervision of Professor Tor Arne Johansen, University of Bergen (UiB), and Professor Alfred Hanssen, University of Tromsø (UiT). The work was funded by the research center for Arctic Petroleum Exploration (ARCEx), and was initially also a collaboration with Electromagnetic Geoservices (EMGS).

The main objective of this thesis was to evaluate the applications of electromagnetic (EM) methods in the Barents sea. However, COVID-19 has proved to be a defining factor in this thesis work, as EMGS had to lay off their entire research department. This ultimately led to their withdrawal from the project, and the loss of this essential industry competence resulted in a modified version of the original project plan. Thus, we shifted our investigation to take a more holistic view on the imaging challenges observed in the Barents Sea, with specific focus on resolution. But with EM methods still playing an essential part of the PhD study.

The thesis is a collection of three papers, presented in chronological order. However, the thesis also includes an extensive introductory section, providing background information and supporting materials that could not be part of the publications due to their limited format. I am the first author of all the publications.

Acknowledgements

A PhD project is a journey which cannot be undertaken alone. In my case it is also the culmination of over 20 years of school and studies. Along the way, there have been countless unsung heroes (some call these teachers). However, there are some that I would like to single out.

Firstly, i would like to extend my deepest gratitude to Prof. Leiv-J Gelius. You have been my supervisor for more than 5 years now, and I could not have done this without you. I remember quite well our first interaction. It was while I was still a bachelor student, and we were occupying a room that you had booked (there was a tiny post-it note on the backside of the door). You bluntly asked if I could read (I still believe you were in the wrong here). Thus, I have to admit it was a bit of a rocky start when we started to work together during my master's project. With time, however, I started running to you with questions, and you always made time to answer. These questions were quite simple, and would normally take five minutes to answer. Yet, I regularly found myself leaving an hour later with newfound understanding of everything from geophysics to espionage scandals in the 80's. Once again, thank you for sharing your wisdom, experience and passion for geophysics with me.

I would like to offer special thanks to Prof. Annik Myhre (1951-2020), who have impacted the lives of so many students. Your door was always open, and there was never a problem you would not dive headfirst into to improve the life of any student. I would not be where I am without you, and although you are no longer with us, your unwavering kindness will not be forgotten.

Enders Robinson (1930-2022) was a giant in our field. He is known as the "Father of Deconvolution", and his research paved the way for the digital revolution in geophysics. He was also a true gentleman, and we were honored when he accepted to contribute to our paper "Revisting holistic migration". This publication, like many others, builds on his pioneering work, and his legacy will live on.

I would also like to extend my gratitude to Prof. Tor Arne Johansen for fruitful discussions during my PhD project. A humble thanks should also be extended to Prof. Alfred Hanssen, who was the one who gave me the opportunity to do a PhD in the first place, through the ARCEx project. As mentioned, COVID-19 has been a defining factor in this thesis work. With the loss of essential industry partners, I would also like to thank Dr. Torgeir Wiik for filling the knowledge gap during the start of my PhD project. When carrying out method-based studies, such as the ones presented in this thesis, an exhaustive verification cannot be obtained without proper field data examples. In that regard, I wish to extend my gratitude to EMGS for providing the CSEM data used in this thesis work. Another important contributor is Lundin Norway AS (now AkerBP), who provided the seismic field data used in the first paper of this thesis. Moreover, I owe a huge debt of gratitude to the Lundin team: Dr. Jan Erik Lie, Dr. Andreas Kjelsrud

Evensen, Dr. Aina Juell Bugge, Associate Prof. Odd Kolbjørnsen and Espen Harris Nilsen have provided everything from financial support, theoretical discussions and help with seismic data processing for both my MSc and PhD project.

In fifth grade, all my classmates wanted to be football players or movie stars. It was therefore a bit of a surprise to the teachers and parents when I said that I wanted to become a geologist. It was much later (i.e. eighth grade) that I figured i had a knack for mathematics, and promptly decided that I was going to become a geophysicist. Nonetheless, some of the parents still remember me as "the geologist", but I have long since given up on explaining the difference to the uninitiated. After I decided to become a geophysicist, I have never wavered, but I have had plenty of support along the way. I would like to thank my family for their support, and for allowing me to break the suspension of our car due to overloading it with rocks during our road trips. Another important support through my PhD period was the Bandy team, which helped me stay sane during the dark days of COVID lockdown. My colleagues also deserve all the praise in the world for putting up with my utter nonsense.

Finally, the most important one of all. To my dearest Kristine. You sighed and said "three more years of this" when I was offered the position. Yet, you have always supported me (some would say in sickness and in health) and there is no way I can thank you enough.

Vemund Stenbekk Thorkildsen
Oslo, March 2023

List of Publications

Paper I

Revisiting holistic migration.

Vemund S. Thorkildsen, Leiv-J. Gelius and Enders A. Robinson.

The Leading Edge, Volume 40, issue 10 (2021): 768-777.

Paper II

Electromagnetic resolution - A CSEM study based on the Wisting oil field.

Vemund S. Thorkildsen and Leiv-J. Gelius.

Geophysical Journal International, Volume 233, Issue 3 (2023): 2124–2141.

Paper III

Resolution enhancement of 2D CSEM images by use of PSF inversion.

Vemund S. Thorkildsen and Leiv-J. Gelius.

Submitted to *Frontiers in Earth Science.* Special issue: *Advances in Geophysical Inverse Problems.*

List of related works

Podcast

Seismic Soundoff 131: How to mine old theories for new insights.

Produced by Andrew Geary at 51 Features, LLC for the Society of Exploration Geophysicists (SEG).

Published November 3, 2021. URL: https://seg.org/podcast/Post/13622/Episode-131-How-to-mine-old-theories-for-new-insights

Expanded abstract

Diffraction Separation and Holistic Migration: High-Resolution Imaging beyond Nyquist.

Leiv-J. Gelius. and Vemund S. Thorkildsen

82nd EAGE Annual Conference & Exhibition. European Association of Geoscientists & Engineers. Issue 1 (2020):1-5.

Contents

List of Figures

List of Tables

Chapter 1

Introduction

Geophysics can in broad terms be defined as the study of our Earth by employing principles of physics. Although this discipline, like many other research fields, was not strictly defined before the 19th century, several examples of geophysical measurements can be found in ancient civilisations. The first known practical use of geophysical measurements is likely Zhang Heng's seismograph (Pajak, 2005), which exploits the directivity and displacement of seismic p-waves in order to forecast impending earthquakes. This early warning was important as the fast p-waves have a much lower amplitude than the slower surface waves. In addition, the instrument could give an indication of the origin of the earthquake. Another important (and ancient) invention comes in the form of the compass, which William Gilbert used to prove that the earth itself is magnetic in his book *On the Loadstone and Magnetic Bodies, and on the Great Magnet the Earth*, published in 1600 (Gilbert, 1893). These inventions were made with only a very basic understanding of the underlying physics, and the corresponding observations made can be described as having the most rudimentary resolution. However, the observations and inventions were driven by a desire to gain knowledge about the Earth. In this thesis, we will pursue the same goal by investigating resolution in geophysical imaging and inversion.

The history of early science is littered with misconceptions and superstition. For example, Gilbert's seminal publication also debunks the superstition that a magnet rubbed with garlic will lose its ability to attract iron (Gilbert, 1893; Byrne, 2015). The early discoveries in electromagnetism were based on experimental physics. In 1820, the Danish scientist Hans Christian Oerstad discovered the relationship between electricity and magnetism by placing a current-carrying wire over a compass. Initially not expecting any reaction, the needle jerked rapidly and aligned itself perpendicular to the wire. By reversing the current direction, the needle flipped 180 degrees. These findings were soon confirmed by Francois Arago and André-Marie Ampère. Moreover, the latter verified that a current-carrying wire did not only behave like a magnet, it *was* a magnet. Thus, the connection between magnetism and electricity was made, and electromagnetism was born (Mitolo & Araneo, 2019).

It was now evident that a wire carrying a current will induce a magnetic field. Conversely, was it possible to prove that a magnetic field would produce an electric current? Michael Faraday tried to prove this by placing an inert wire inside the magnetic field of a live wire. The inert wire experienced a brief current when the current in the second wire was turned on and off, but no current was observed when the magnetic field was kept stable. Faraday would later prove that it was not the presence, but the change in magnetic field that creates the electric current. This would later result in the invention of electromagnetic induction, and the birth of the electric generator. By then, the connection between electricity and magnetism was obvious, but it was almost entirely built upon experimental physics. However, the mathematician James Clerk Maxwell would formalize the theory resulting in the famous set of equations now bearing his name (Mitolo & Araneo, 2019). Maxwell's equations can be seen as the most important legacy of 19th century physics, and are (as we shall see in Paper II and III of this thesis) completely fundamental for modern applications of electromagnetic methods in geophysics.

As with the case of electromagnetism, initial discoveries in the fundamentals of wave propagation were made through experimental physics and were intimately linked with the study of optics. The first paper in this thesis considers seismic diffraction imaging. The first written account of diffraction is attributed to Francisco Maria Grimaldi, who observed a new wave mode not obeying the three modes recognized by opticians. He named this wave mode "diffracted" since the waves are scattered into diverse luminous stripes. The reader is referred to Figure 1 of Hoeber et al. (2017) for details regarding Grimaldi's experiment. In 1690, Christiaan Huygens published his seminal book *Traité de la Lumière*, which advocates that each point on a wavefront must be treated as a source of a spherical wave (i.e., diffraction). The wavefront at a later position is then constructed as the sum of the contributions from all these secondary sources, and is known as Huygens principle today. Huygens contribution was made without a proper understanding of interference, which would be provided over a century later by Thomas Young. The next century would include important contributions from Fresnel, Helmholtz and Kirchhoff to the theory of diffracted waves. This would later be formalized by Joseph Keller (Hoeber et al., 2017).

The mathematical formulation of diffraction is intimately linked to the process of seismic migration. One of the most commonly used imaging algorithms is Kirchhoff migration, which in practice works by assuming that each image point is a possible diffraction. The first migrations based on this principle were carried out as early as the 1920s, and was a manual operation using pencil and paper where a reflection can be found from the envelope of these diffraction points (Gray, 2011). This would later lead to the invention of a range of mechanical devices, all of which were built on the concepts formalized by (Hagedoorn, 1954). The computerized version of this technique, which additionally allows for interfering events, is what we know as Kirchhoff migration today.

Creating images of the subsurface can be seen as one of the most difficult imaging tasks, as we are dealing with complex targets with little structural constraint. These images are employed by geologists to interpret the subsurface, and they are crucial for oil exploration, carbon capture and storage, infrastructure projects, and more. However, acquiring geophysical data is associated with considerable cost. Thus, effort should be made to exploit these data to the fullest extent.

Several geophysical processing steps are also associated with high computational demand, and lowering the processing cost might therefore make several processes more achievable. This will be a topic of this thesis.

1.1 Motivation

About two thirds of the undiscovered petroleum resources on the Norwegian Continental Shelf are assumed to be located in the Barents Sea. However, the drilling success rate has been rather low in recent years. As an example, Equinor drilled 17 wells in the Barents Sea from 2013-2017 but made only three discoveries. None of them were large enough to merit an independent development. In 2017, 17 test wells were drilled, three times as many as the year before. The largest discovery made that year was the Filicudi project of Lundin, but its expected resources are less than five percent of those of Johan Sverdrup. In 2018, the high level of activity continued with another 13 wells being drilled, but since then most of the oil and gas industry seem to doubt the economic viability of Barents Sea expansion. In 2021, only six companies (including Equinor and AkerBP) remained interested in new areas in the Barents Sea. Nine years earlier, 36 companies raced for exploration licences. Due to the complexity of the Barents Sea, especially the Western part, the use of unconventional data types is employed in order to improve basic understanding. Such supplementary geophysical data can be satellite gravity measurements, airborne magnetic measurements, diffraction seismic, as well as passive and active electromagnetics (EM). Especially the EM data are assumed to be of significant value due to the occurrence of shallower plays in the Barents Sea.

Seismic data are very sensitive to lithology and provide controls on the structure of the subsurface. However, the method may fail to identify oil-water contacts and is mostly sensitive at low hydrocarbon saturation. On the contrary, active EM or Marine Controlled Source Electromagnetics (CSEM) is very sensitive to fluids and provides an estimate of bulk resistivity and therefore the presence or absence of conductive brine. Such data are also most sensitive to high hydrocarbon saturation, complementing the seismic method.

Seismic reflection data may also fail to give a well-resolved image of important structural information on the subsurface (such as faults and wedges/pinchouts). However, by separating weaker diffractions from the stronger reflections, an improved reconstruction with higher resolution can be obtained. Paper I gives an example of such methodology applied to a gas hydrate from the Barents Sea.

1.2 Scope of the thesis

This study constitutes a part of the *Research Centre for Arctic Petroleum Exploration* (ARCEx) which is a collaboration between academia and the industry with support from the Norwegian Research Council and Norwegian authorities. As mentioned in the previous section, the aim of this project has been to address the complex imaging challenges in the Barents Sea by using unconventional geophysical methods to add new information.

As a first step, we investigated holistic migration as a method to achieve high-resolution images from severely undersampled data. Holistic migration was introduced more than 25 years ago (Neidell, 1997; Robinson, 1998), but lacked proper data examples and did not account for the noise introduced due to undersampling. Thus, we proposed furthering the method by employing diffraction-separated data. We also introduced a novel noise removal method based on median filtering of the Kirchhoff migration operators. The feasibility of the proposed approach was demonstrated on both synthetic and field data. Moreover, we expand upon this method with several data-based examples in the main body of this thesis (Chapter 3).

Next, we investigated the feasibility of undersampling CSEM data while retaining the resolution of the inversion. As there are major differences between the imaging process of seismic and CSEM data, we proposed subsampling based on the resolution matrices associated with inversion. The resolution matrices can be computed from well-known inversion theory (Menke, 2012), and give access to several quantities that can be used for determining the resolving power of a particular dataset or the importance of specific datapoints. In this study, we developed a framework for how these quantities can be employed efficiently. In order to make such a study feasible, this also included developing a user interface which integrates the full workflow into one software.

Finally, we considered the deblurring of CSEM inversions through point spread function (PSF) inversion extracted from the model resolution matrix, by analogy with work carried out on seismic data (Hu et al., 2001; Sjoeberg et al., 2003; Yu et al., 2006; Takahata et al., 2013; Yang et al., 2022). This work included the non-trivial task of creating a space-varying blur matrix. The PSF inversion is not computationally demanding, but it is sensitive to input parameters, such as the proper choice of PSFs. The study therefore included the creation of a user interface that allows for rapid testing of user-determined input parameters.

1.3 Thesis outline

This thesis is organized as follows. In Chapter 2, the relevant resolution criteria for seismic and electromagnetic data are described. In the chapter that follows, the basic concepts of optical and seismic holography, diffraction separation, and holistic migration are discussed. Chapter 3 also includes some additional results for holistic migration, where different undersampling strategies for diffraction separated data are further investigated in addition to some data examples of reflection data. In Chapter 4, the basic theory of CSEM is introduced, followed by a discussion of the resolution matrices and derived quantities. This is followed by a brief discussion of the main features in the open-source MARE2DEM software employed in this PhD study, along with a more thorough description of our own user interface. The final part of Chapter 4 includes the basic theory of image deblurring based on PSF inversion. Finally, a summary of the three papers is given before a discussion section finalizes the thesis with an outlook toward new applications of the methods presented.

Chapter 2

Resolution in geophysical imaging/inversion

2.1 Resolution in seismic imaging

The starting point is the Porter-Bojarski equation, discussed in more detail in Section 3.1.2 (cf. Equation 3.8). Figure 3.5 shows a schematic of the acoustic experiment discussed in this section. We specialize here in the case of weak scatterers, which simplifies Equation 3.8 as follows (ideal aperture):

$$\begin{aligned} p_{bp}(\mathbf{r}, \mathbf{r_s}, \omega) &= \frac{1}{i\omega\rho} \int_V \alpha(\mathbf{r_0}) k_0^2 G_h(\mathbf{r}, \mathbf{r_0}, \omega) p_i(\mathbf{r_0}, \mathbf{r_s}, \omega) dV \\ &= - i\omega \int_V \alpha(\mathbf{r_0}) \frac{1}{\kappa} G_h(\mathbf{r}, \mathbf{r_0}, \omega) p_i(\mathbf{r_0}, \mathbf{r_s}, \omega) dV, \end{aligned} \tag{2.1}$$

where p_{bp} is the scattered or backpropagated wavefield, $\kappa = \rho c_0^2$ is the bulk modulus or incompressibility, α is the scattering potential, p_i is the incident wavefield, and G_h is the homogeneous Green's function. Note that Equation 2.1 is valid within a Born approximation. Employing a U/D type of imaging condition (e.g., assuming a scatterer exists where the first arrival of the downgoing (incident) wave is time-coincident with the upgoing wave (Claerbout, 1971)), an estimate of the scattering potential can be obtained from use of Equation 2.1 (integrating over the available frequency band $\Delta\omega$),

$$\begin{aligned} \langle \alpha(\mathbf{r}) \rangle &= \int_{\Delta\omega} \frac{p_{bp}(\mathbf{r}, \mathbf{r_s}, \omega)}{p_i(\mathbf{r}, \mathbf{r_s}, \omega)} d\omega \\ &= - \int_V \alpha(\mathbf{r_0}) \left[\int_{\Delta\omega} \frac{i\omega}{\kappa(\mathbf{r_0})} G_h(\mathbf{r}, \mathbf{r_0}, \omega) \frac{p_i(\mathbf{r_0}, \mathbf{r_s}, \omega)}{p_i(\mathbf{r}, \mathbf{r_s}, \omega)} d\omega \right] dV \\ &\equiv \int_V \alpha(\mathbf{r_0}) PSF(\mathbf{r}, \mathbf{r_0}) dV, \end{aligned} \tag{2.2}$$

where PSF is the resolution function or Point-Spread Function (PSF) of the image when a "t = 0" image condition is applied. Since the homogeneous Green's function G_h is "singular" when $\mathbf{r} = \mathbf{r_0}$, it is feasible to set $p_i(\mathbf{r_0}, \mathbf{r_s}, \omega)/p_i(\mathbf{r}, \mathbf{r_s}, \omega) \cong 1$ in the expression for the resolution function (local imaging), i.e.

$$PSF \cong - \int_{\Delta\omega} \frac{i\omega}{\kappa(\mathbf{r_0})} G_h(\mathbf{r}, \mathbf{r_0}, \omega) d\omega, \tag{2.3}$$

with G_h representing the governing part of the point-spread function. For a monochromatic case, understanding the role of G_h automatically gives a good idea of the resolving power of an integral-equation type of migration, as in Equation 2.2. Such migration is also called holographic imaging because a 3D wavefield is reconstructed based on 2D measurements. Equation 2.3 is only valid in the case of an ideal aperture (i.e. receivers uniformly distributed across the surface S). The homogeneous Green's function G_h being the backbone of the point-spread function has causal and anticausal parts and can be written explicitly as

$$G_h(\mathbf{r}, \mathbf{r_0}, \omega) = G_0(\mathbf{r}, \mathbf{r_0}, \omega) + G_0^*(\mathbf{r}, \mathbf{r_0}, \omega), \tag{2.4}$$

with G_0 being the Green's function of the background and G_0^* being its complex conjugated counterpart. The formulation shown in Equation 2.4 represents a superposition of a time-advanced and time-retarded Green's function. Due to the causal and anticausal parts of G_h, backpropagation of the recorded field will give a diffraction-limited focus. Consider now a locally homogeneous background model (also monochromatic). The homogeneous Green's function now takes the form (3D):

$$\begin{aligned} G_h =& i\omega \left[\frac{e^{ik_0|\mathbf{r}-\mathbf{r_0}|}}{4\pi|\mathbf{r}-\mathbf{r_0}|} - \frac{e^{-ik_0|\mathbf{r}-\mathbf{r_0}|}}{4\pi|\mathbf{r}-\mathbf{r_0}|} \right], \\ =& -\frac{\omega k_0 sinc(k_0|\mathbf{r}-\mathbf{r_0}|)}{2\pi}, \qquad k_0 \frac{\omega}{c_0} = \frac{2\pi}{\lambda_0}, \end{aligned} \tag{2.5}$$

where k_0 is the wavenumber, c_0 is the locally uniform background velocity, and λ_0 is the corresponding wavelength. From Equation 2.5, it is clear that the focusing point is described by a sinc function. Assuming that the size of this focus point is primarily defined by one main lobe of the radial sinc function, its diameter d can be approximated as

$$d \cong 2|\mathbf{r} - \mathbf{r_0}| = \lambda_0, \tag{2.6}$$

which is analogous to the focused beam size limit of imaging optics as determined by the diffraction of light. For an axial symmetric optical system, the formula of the resolution limit can be obtained from the classical diffraction theory for electromagnetic waves, i.e., the Rayleigh criterion (Born & Wolf, 1999):

$$\Delta = \frac{0.61\lambda_0}{N_{apt}}, \tag{2.7}$$

where Δ is the focused beam size and N_{apt} is the numerical aperture that describes the angle range in which the imaging system can accept or emit light. In the theoretical limit of $N_{apt} \to 1$ (i.e., ideal aperture), the focused beam size Δ will tend towards $0.61\lambda_0$. The superposition in equation 2.5 can be further visualized by use of a simple example. Consider a point source embedded in a homogeneous background medium surrounded by 1600 evenly distributed receivers. The velocity of the background medium is 2000 m/s, and the source pulse is defined by a finite frequency band (10-50 Hz) Ricker wavelet with a center frequency of 20Hz. Figure 2.1 shows G_h in the time-domain after Fourier synthesis over the frequency band at five different backpropagation times (snapshots). The non-causal parts of the kernel G_h can be observed in Figures 2.1a and b. These contributions are non-physical, as they appear at negative travel times. Figures 2.1d and e show the causal parts of G_h, representing the diverging (and physical) wavefield. It is clear that the focus point (at $t = 0$) is defined by one main lobe (Figure 2.1c), as opposed to an ideal spike (due to lack of evanescent waves). This focus point is caused by interference between the converging and diverging wavefields, and has a size of approximately one half of the central wavelength.

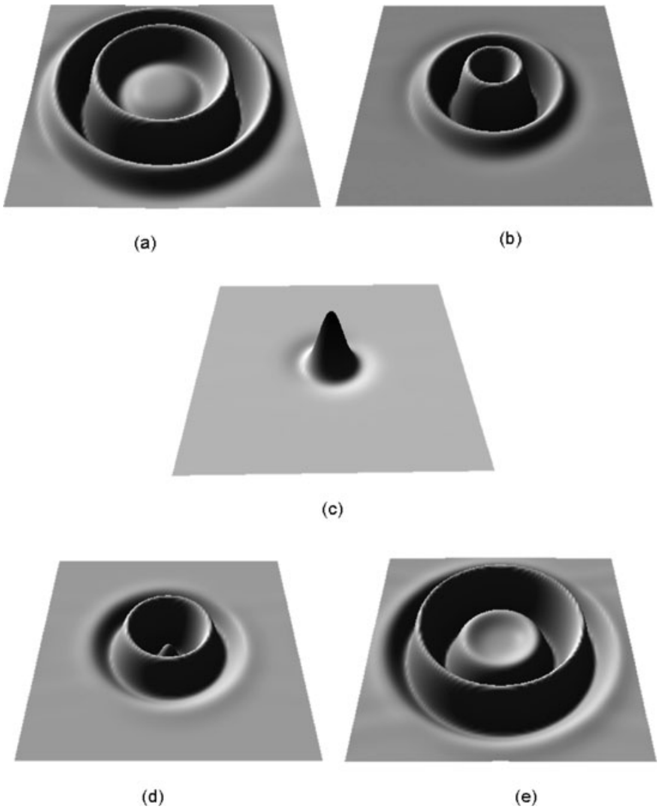

Figure 2.1: *The backpropagated kernel G_h at different backpropagation times: (a) t=-0.060s, (b) t=-0.032s, (c) t=0.0s, (d) t=0.032, (e) t=0.060s. Example taken from (Gelius & Asgedom, 2011)*

Unless there is an infinite frequency band and an ideal aperture, a subsurface point will be blurred when seismic data are imaged (diffraction-limited focus). In case of a non-ideal aperture, the homogeneous Green's function G_h in Equation 2.3 is replaced by a general backpropagation kernel $\mathbf{B}$ and the focus will be even more distorted. For further details, the reader is referred to Gelius & Asgedom

(2011).

Seismic data are reflection dominant. In order to improve the resolution of finer details of the earth model (e.g., faults, pinchouts, or wedges), diffractions need to be employed. However, the majority of these diffractions are masked by stronger reflections. In Section 3.2, a technique for diffraction separation will be discussed. Such an approach will amplify weak diffractions and increase the resolving power of seismic imaging. Another useful characteristic of diffractions is that they scatter over a large aperture, which is different from the local character of a reflection. Thus, it should be possible to significantly decimate a dataset of diffractions and still obtain well-resolved images of the subsurface. This is the topic of paper I in this thesis.

2.1.1 Diffractions versus scattering

In the physics literature on light, diffraction is considered as a phenomenon observed only in waves, but scattering is associated with both waves and particles. Diffraction is further defined as a property of propagating waves, whereas scattering is a property of wave interaction.

In the seismic case, which is relevant for this thesis work, both concepts are commonly used in a pragmatic way to describe a phenomenon where an incident wavefield interacts with a local inhomogeneity in the medium. Note also that in the seismic literature, diffractions are sometimes limited to the ideal cases of a point (tip wave) or an edge. In the latter case, the diffraction is characterized by a phase change of 180 degrees on either side of the diffraction edge. However, in a practical case where diffractions are separated from reflections (c.f., Section 3.2), such phase shifts are not observed. This observation also supports the idea that diffractions (and scattering) are mainly caused by local inhomogeneities associated with faults, pinch-outs, and similar geological structures.

2.2 Resolution in diffusive electromagnetic imaging/inversion

In the seismic case, the effect of absorption is less pronounced, and the center wavelength may serve as a good indicator of the resolving power. After imaging, the optimal focus of a scatterer will be in the order of half a wavelength since evanescent waves are not measured (too far away from their origin) (Gelius & Asgedom, 2011).

A major part of this work addresses diffusive electromagnetic waves with emphasis on (frequency-domain) CSEM, as discussed in more detail in Chapter 4. Different from seismic waves, the diffusive EM waves employed in CSEM will be of guided mode type. Since the diffusive EM waves discussed here correspond to the use of very low source frequencies (i.e quasi-static approximation), using wavelength as a measure of resolution in the image domain does not yield similar meaningful information as in the seismic case. In addition, due to the complex imaging condition caused by the guided modes, use of migration is not very practical. Although some examples of electromagnetic migration can be found in the literature (e.g. Mittet et al. (2005)), it is most common to employ full inversion. After inversion, well-known quantities from general inversion theory can be used to quantify the resolution of the inverted model by analogy with the PSF discussed in the seismic case. However, since forward modelling is the backbone of every inversion algorithm, it represents a natural starting point for our further discussion.

In the following, we will specialize in the case of a 2D electric earth model with possible anisotropy. In CSEM inversion, we need to solve Maxwell's equations on a discrete grid. In the frequency domain, the continuous versions of these equations read:

$$\nabla \times \mathbf{E} - i\omega\mu\mathbf{H} = 0 \tag{2.8}$$

and

$$\nabla \times \mathbf{H} + i\omega\bar{\bar{\varepsilon}}_c\mathbf{E} = \mathbf{J_s}, \tag{2.9}$$

where $\mathbf{E}$ and $\mathbf{H}$ represent respectively the electric and magnetic field strengths, ω is the angular frequency, μ is the permeability, and $\mathbf{J_s}$ represents the electric source. Let x define the strike direction, and assume a 2D electrical model $\bar{\bar{\varepsilon}}_c(y, z)$ where the complex permittivity is defined as

$$\bar{\bar{\varepsilon}}_c = \bar{\bar{\varepsilon}} + i\frac{\bar{\bar{\sigma}}}{\omega}, \tag{2.10}$$

and where $\bar{\bar{\varepsilon}}$ is the permittivity tensor, $\bar{\bar{\sigma}}$ is the conductivity tensor, and ω is the angular frequency. EM sounding of resistivity (or conductivity) is associated with a diffusive wave characteristic and thus a higher degree of attenuation than seismic data, and the seismic resolution criterion represented by the wavelength does not carry the same meaning as already mentioned. However, one commonly used metric, describing the absorption of EM waves in a homogeneous medium, is the skin depth d. It can be explicitly defined as (in meters) (Simpson & Bahr, 2005):

$$d \approx 503.3\sqrt{\frac{\rho}{f}}. \tag{2.11}$$

where ρ is the resistivity $[\Omega m]$ and f is the frequency $[Hz]$ of the propagating wave. Consider now a half-space with a representative background resistivity of $\rho = 5\Omega m$ and a probing frequency of $f = 10Hz$. The associated skin depth would in this case be only $d \approx 350m$. Moreover, from Equation 2.11 it is clear that higher frequencies are associated with high absorption. Thus, in order to be useful as an exploration method, CSEM uses very low probing frequencies.

Equation 2.10 can be therefore be approximated by (quasi-static assumption, $\bar{\bar{\sigma}} >> \omega\bar{\bar{\varepsilon}}$)

$$\bar{\bar{\varepsilon}}_c \simeq i\frac{\bar{\bar{\sigma}}}{\omega}, \tag{2.12}$$

where the conductivity takes a diagonal form in case of a transverse isotropic earth model:

$$\bar{\bar{\sigma}} = \begin{bmatrix} \sigma_x & 0 & 0 \\ 0 & \sigma_y & 0 \\ 0 & 0 & \sigma_z \end{bmatrix}. \tag{2.13}$$

Equation 2.9 can now be simplified as

$$\nabla \times \mathbf{H} - \bar{\bar{\sigma}}\mathbf{E} = \mathbf{J_s}. \tag{2.14}$$

Since x represents the strike direction (no variation in electric properties), a spatial Fourier transform can be applied with respect to this coordinate. The 3D problem is then simplified to that of 2.5D, where for each wavenumber k_x, a 2D forward problem is solved. After application of a spatial Fourier transform along the strike direction, Equations 2.8 and 2.14 can be written on component form:

$$\frac{\partial E_z}{\partial y} - \frac{\partial E_y}{\partial z} = i\omega\mu H_x, \tag{2.15}$$

$$\frac{\partial E_x}{\partial z} - ik_x E_z = i\omega\mu H_y, \tag{2.16}$$

$$ik_x E_y - \frac{\partial E_x}{\partial y} = i\omega\mu H_z, \tag{2.17}$$

$$\frac{\partial H_z}{\partial y} - \frac{\partial H_y}{\partial z} = \sigma_x E_x + J_{sx}, \tag{2.18}$$

$$\frac{\partial H_x}{\partial z} - ik_x H_z = \sigma_y E_y + J_{sy}, \tag{2.19}$$

$$ik_x H_y - \frac{\partial H_x}{\partial y} = \sigma_z E_z + J_{sz}. \tag{2.20}$$

From Equations 2.17 and 2.19, H_z and E_y can be expressed as functions of H_x and E_x:

$$H_z = \frac{1}{k_{ty}^2}\Big(\sigma_y \frac{\partial E_x}{\partial y} - ik_x \frac{\partial H_x}{\partial z} + ik_x J_{sy}\Big), \tag{2.21}$$

$$E_y = \frac{1}{k_{ty}^2}\Big(- ik_x \frac{\partial E_x}{\partial y} - i\omega\mu \frac{\partial H_x}{\partial z} + i\omega\mu J_{sy}\Big), \tag{2.22}$$

where $k_{ty}^2 = k_x^2 - i\omega\mu\sigma_y$. From Equations 2.16 and 2.20, H_y and E_z can be similarly expressed as functions of H_x and E_x:

$$H_y = \frac{1}{k_{tz}^2}\Big(- \sigma_z \frac{\partial E_x}{\partial z} - ik_x \frac{\partial H_x}{\partial y} - ik_x J_{sz}\Big), \tag{2.23}$$

$$E_z = \frac{1}{k_{tz}^2}\Big(- ik_x \frac{\partial E_x}{\partial z} + i\omega\mu \frac{\partial H_x}{\partial y} + i\omega\mu J_{sz}\Big), \tag{2.24}$$

where $k_{tz}^2 = k_x^2 - i\omega\mu\sigma_z$. Substituting Equations 2.22 and 2.24 into Equation 2.15 gives Equation 2.25. Similarly, substituting Equations 2.21 and 2.23 into Equation 2.20 gives Equation 2.26. The main result can now be summarized by two coupled equations for the strike parallel field strengths E_x and H_x:

$$\begin{aligned} & \frac{\partial}{\partial y}\Big(\frac{\sigma_y}{k_{ty}^2}\frac{\partial E_x}{\partial y}\Big) + \frac{\partial}{\partial z}\Big(\frac{\sigma_z}{k_{tz}^2}\frac{\partial E_x}{\partial z}\Big) \\ & +ik_x\Big(- \frac{\partial}{\partial y}\Big(\frac{1}{k_{ty}^2}\frac{\partial H_x}{\partial z}\Big) + \frac{\partial}{\partial z}\Big(\frac{1}{k_{tz}^2}\frac{\partial H_x}{\partial y}\Big)\Big) - \sigma_x E_x \\ = \quad & J_{sx} - ik_x\Big(\frac{\partial}{\partial y}\Big(\frac{J_{sy}}{k_{ty}^2}\Big) + \frac{\partial}{\partial z}\Big(\frac{J_{sz}}{k_{tz}^2}\Big)\Big) \end{aligned} \tag{2.25}$$

and

$$\begin{aligned} & i\omega\mu\Big(\frac{\partial}{\partial y}\Big(\frac{1}{k_{tz}^2}\frac{\partial H_x}{\partial y}\Big) + \frac{\partial}{\partial z}\Big(\frac{1}{k_{ty}^2}\frac{\partial H_x}{\partial z}\Big)\Big) \\ & +ik_x\Big(- \frac{\partial}{\partial y}\Big(\frac{1}{k_{tz}^2}\frac{\partial E_x}{\partial z}\Big) + \frac{\partial}{\partial z}\Big(\frac{1}{k_{ty}^2}\frac{\partial E_x}{\partial y}\Big)\Big) \\ = \quad & i\omega\mu\Big(- \frac{\partial}{\partial y}\Big(\frac{J_{sz}}{k_{tz}^2}\Big) + \frac{\partial}{\partial z}\Big(\frac{J_{sy}}{k_{ty}^2}\Big)\Big), \end{aligned} \tag{2.26}$$

where $k_{ty}^2 = k_x^2 - i\omega\mu\sigma_y$ and $k_{tz}^2 = k_x^2 - i\omega\mu\sigma_z$. The corresponding transverse field strengths can then be calculated through a post processing step employing Equations 2.21 through 2.24. Let $\hat{\mathbf{d}}$ represent CSEM data calculated by the use of Equations 2.25 and 2.26. If $\mathbf{m}$ represents the corresponding electric earth model, we can formally write:

$$\hat{\mathbf{d}} = F[\mathbf{m}]. \tag{2.27}$$

to represent the forward modelling step. In general, the inversion algorithm aims to find a model where $\hat{\mathbf{d}}$ is as close as possible to the actual measurements $\mathbf{d}$. The process of inversion denotes finding the most optimal model according to a misfit criterion or so-called cost function. In CSEM inversion, it is common to solve for the optimal model that minimizes the data misfit in a least squares sense. However, there is no direct way of finding this model. Thus, the system is solved by use of an iterative model update. Such a model update can be written as

$$\mathbf{m}_{k+1} = \mathbf{J}_w^{-g}\mathbf{W_d}\mathbf{d}_k, \tag{2.28}$$

where $\mathbf{W_d}$ is a data weighting matrix and $\mathbf{d_k}$ (cf. Equation 2.31) is the modified data vector from iteration k. Moreover, $\mathbf{J}_w^{-g}$ is the generalized inverse matrix (Menke, 2012), which takes the form

$$[\mathbf{J}^\dagger\mathbf{W}_d^\dagger\mathbf{W}_d\mathbf{J} + \alpha\mathbf{W_m}^\dagger\mathbf{W_m}]^{-1}\mathbf{J}^\dagger\mathbf{W}_d^\dagger, \tag{2.29}$$

with $\mathbf{J}$ being the Jacobian matrix of first derivatives, and $\mathbf{W_m}$ describing the regularization of the inversion. Note that we only state the main result here; for a more in depth discussion, the reader is referred to Chapter 4. Let $\mathbf{m}_k$ denote the model obtained from the final (k-th) iteration of an inversion cycle. By assuming that model $\mathbf{m}_k$ is linearly close to the true earth model $\mathbf{m}_{true}$, we can write

$$\mathbf{d} = \mathbf{F}[\mathbf{m}_{true}] + \mathbf{n} \approx \mathbf{F}[\mathbf{m}_k] + \mathbf{J}(\mathbf{m}_{true} - \mathbf{m}_k) + \mathbf{n}, \tag{2.30}$$

where $\mathbf{n}$ denotes noise. By use of Equation 2.30, the modified data vector for iteration k can be approximated as

$$\mathbf{d}_k = (\mathbf{d} - \mathbf{F}[\mathbf{m}_k] + \mathbf{J}\mathbf{m}_k) \approx \mathbf{J}\mathbf{m}_{true} + \mathbf{n}. \tag{2.31}$$

Combining Equations 2.28 and 2.31 yields

$$\mathbf{m}_{k+1} = \mathbf{R_M}\mathbf{m}_{true} + \mathbf{J}_w^{-g}\mathbf{W}_d\mathbf{n}. \tag{2.32}$$

In Equation 2.32, $\mathbf{R_M}$ is the *model resolution matrix* (Menke, 2012), and is explicitly given as:

$$\mathbf{R_M} = \Re\left[\left[\mathbf{J}^\dagger\mathbf{W}_d^\dagger\mathbf{W}_d\mathbf{J} + \alpha\mathbf{W}_m^\dagger\mathbf{W}_m\right]^{-1}\mathbf{J}^\dagger\mathbf{W}_d^\dagger\mathbf{W}_d\mathbf{J}\right], \tag{2.33}$$

where $\Re$ indicates taking the real part. The columns of the model resolution matrix can be recognized as point spread functions (PSFs), and indicate how a delta-like perturbation in the model will spread across the model space. Figure 2.2a shows a schematic representation of the computational relationship between the model resolution matrix, the unobtainable true model, and $\mathbf{m}_{k+1}$ (c.f., Equation 2.32 with $n = 0$). Note that this relationship is shown for a 1D model. In the case of a 2D model, the resolution matrix takes a different form because the 2D model vector is reshaped into a 1D model vector. However, by proper reorganization, PSFs can still be recovered in the model space, as shown in Figures 2.2b and c. These examples show respectively the PSF for a well-resolved model parameter (Figure 2.2b) and a poorly resolved model parameter (Figure 2.2c).

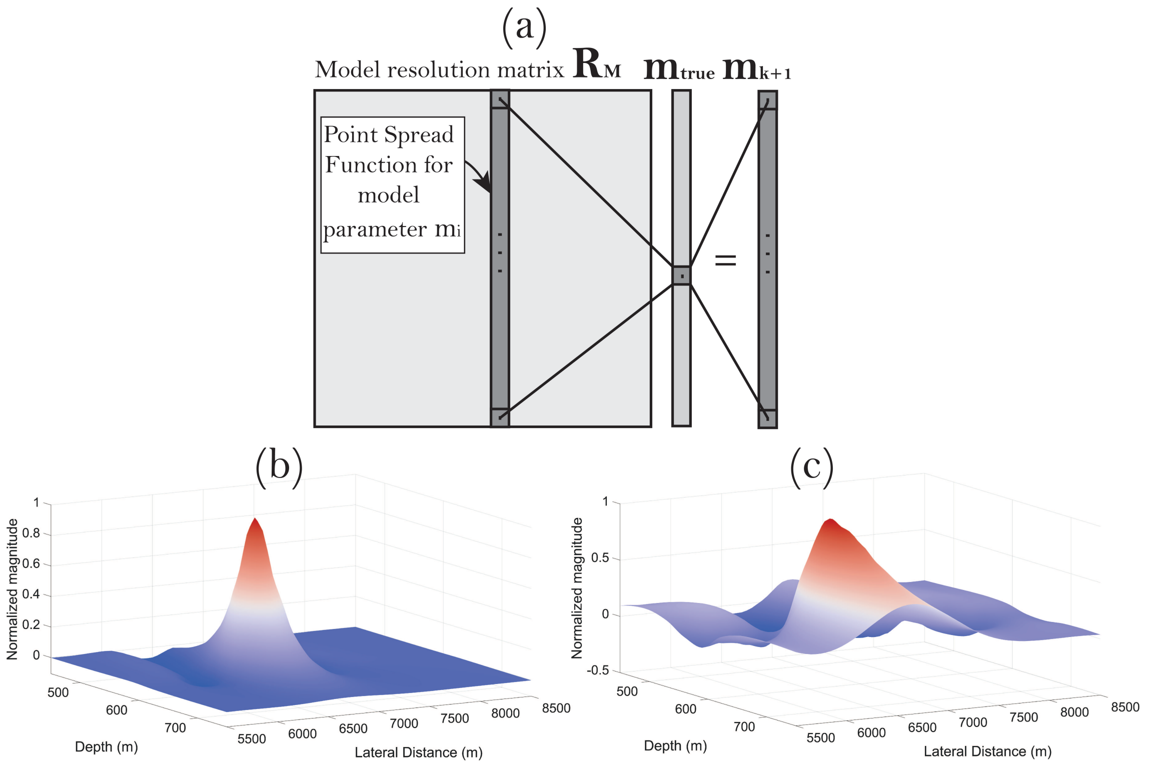

Figure 2.2: *The relationship between the true model* $\mathbf{m}_{true}$ *and the preferred inversion model* $\mathbf{m}_{k+1}$ *expressed by the PSF (1D case). (b) and (c) are examples of a PSF for a well-resolved and poorly resolved 2D case respectively. Both PSFs have been normalized to one for presentation purposes.*

Chapter 3

Seismic holography and diffraction separation

In this chapter, the concepts of optical holography and seismic imaging (acoustic holography) will be compared and discussed. In addition, the methodology of diffraction separation will be introduced and carefully analyzed. However, we start by introducing the basic concepts of optical holography.

3.1 Optical holography vs seismic imaging

3.1.1 Basics of optical holography

Dennis Gabor laid the foundation of modern holography in his landmark paper from 1948. In this work, Gabor tried to improve the resolution of electron microscopes. Laser light had not even been invented yet when he wrote the paper. Further development of holography in the 1950s stifled because light sources were not coherent. However, with the introduction of laser light in 1960, new progress was achieved. The first recording of a 3D optical hologram was produced in 1962. In the following, we will see that interference and diffraction serve as primary principles of optical holography. To illustrate basic concepts, the in-line type of holography is considered. Its simplified setup is given in Figure 3.1, where a reference plane-wave beam u_r and a scattered (object) wave u_s interfere, with the interference pattern recorded by a photographic plate associated with a scatter point P.

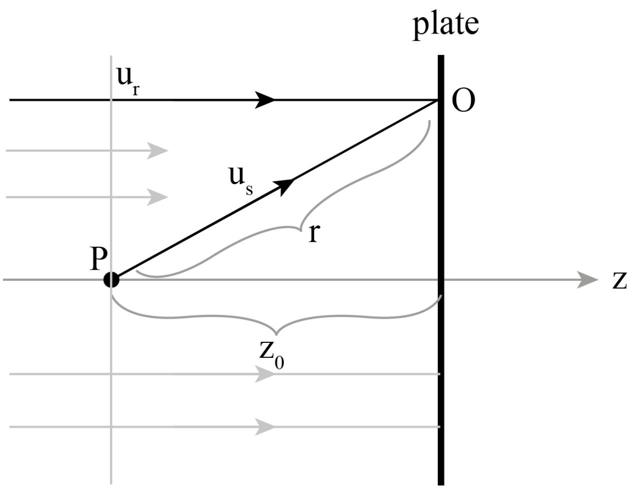

Figure 3.1: *Basic concept of in-line optical holography.*

The reference wave is a monochromatic plane wave which can be expressed mathematically as (with phase reference to point P and omitting ωt dependence)

$$u_r = u_{r_0} e^{ikz_0} \qquad , k = \frac{2\pi}{\lambda}, \tag{3.1}$$

where z_0 is the normal distance from the object point P to the plate and λ is the wavelength of the monochromatic wave. The corresponding scattered wave from object point P measured at O is then (spherical wave)

$$u_s = \frac{u_{so}}{r} e^{ikr}, \tag{3.2}$$

Thus, the resultant field at O is

$$u = u_r + u_s, \tag{3.3}$$

Introducing the transmittivity, T, of the photographic plate, the recorded interference pattern is given by $T = kI$, with I being the total intensity and k is a constant. By use of Equations 3.1 and 3.2, an explicit expression for this recording can be obtained:

$$\begin{aligned} T = kI &= k|(u_r + u_s)|^2 = k(u_r + u_s)(u_r + u_s)^* \\ &= k(u_r u_r^* + u_r u_s^* + u_s u_r^* + u_s u_s^*) \\ &= k\left[|u_{r_0}|^2 + \frac{u_{r_0} u_{s_0}^*}{r} e^{ik(z_0 - r)} + \frac{u_{r_0}^* u_{s_0}}{r} e^{ik(r - z_0)} + \frac{|u_{s_0}|^2}{r^2} \right]. \end{aligned} \tag{3.4}$$

In this case, the interference pattern will take the form of a Fresnel zone lens with a constructive ring pattern, where the l-th ring has a radius given by the expression (cf. Figure 3.2)

$$r_l^2 = (z_0 + l\lambda)^2 - z_0^2 = 2z_0 l\lambda + l^2\lambda^2 \cong 2z_0 l\lambda, \tag{3.5}$$

since $z_0 >> \lambda$ in case of a laser. Differentiating Equation 3.5 with respect to the order l gives an expression for the distance between the neighbouring rings:

$$\Delta r_l \cong \frac{z_0\lambda}{r_l} = \sqrt{\frac{z_0\lambda}{2l}}. \tag{3.6}$$

Thus, this distance is shrinking with increasing order l. From Figure 3.2, we can easily see that information about scattering point P is distributed over the entire photographic plate. Thus, access to only parts of the hologram still gives enough information to virtually reconstruct P. This is the underlying idea of the broken hologram discussed in Section 3.1.3.

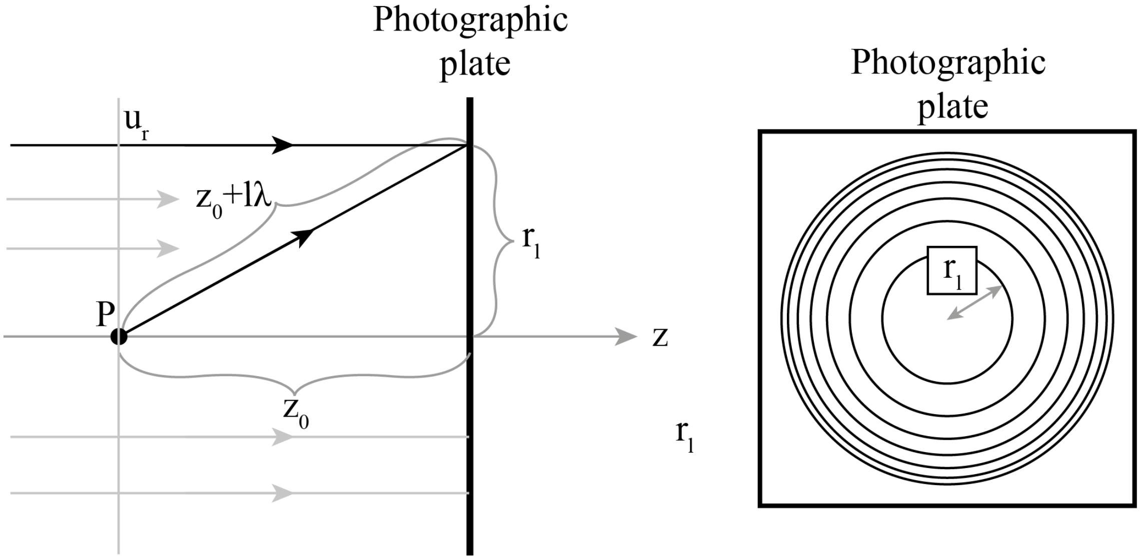

Figure 3.2: *Recording of an in-line hologram (Fresnel zone lens)*

By illuminating the 2D interference pattern on the photographic plate with the reference beam, a 3D virtual image of the object can be obtained:

$$\begin{aligned} Tu_r = & \left[ku_{r_0}^2 + \frac{k|u_{s_0}|^2}{r^2}\right] u_{r_0} e^{ikz_0} + \frac{ku_{s_0}|u_{r_0}|^2}{r} e^{ikr} \\ & + \frac{ku_{r_0}^2 u_{s_0}^*}{r} e^{i(2k_{z_0} - kr)} \end{aligned} \tag{3.7}$$

From Equation 3.7, we can identify three main contributions:

- The direct wave, which is identical to the reference wave except for an overall change in amplitude.

- The object wave, which is a spherical wave but with a change in intensity modulated by the recording and developing processes. This contribution is also known as the virtual image.

- The conjugate wave, which is a spherical wave collapsing to a point at a distance z_0 to the right of the hologram (cf. Figure 3.3)

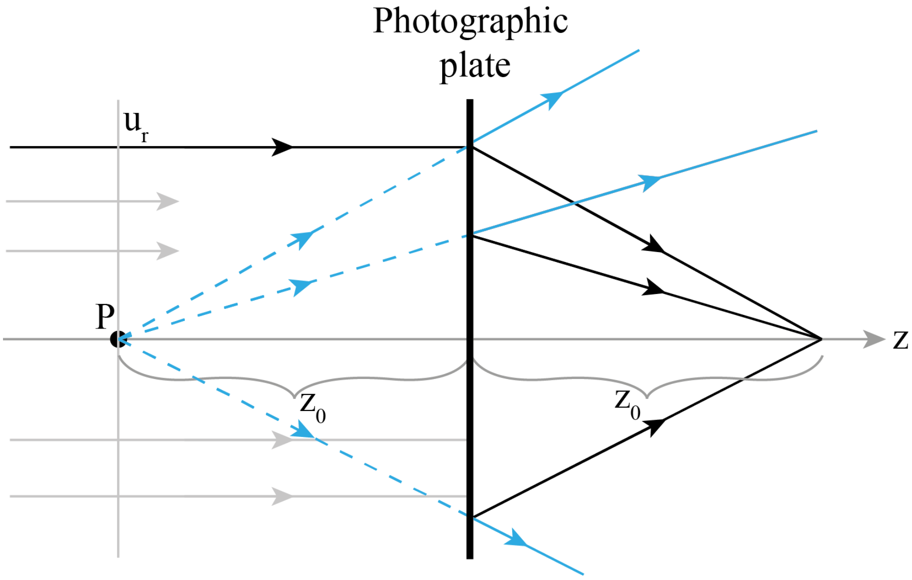

Figure 3.3: *Reconstruction of a real and virtual image point.*

The acquisition setup discussed here represents an idealized case of optical holography with only one scatterer. In a real world case, the image consists of a large number of scatterers, each of them inducing ring-like patterns in the photographic plate (cf. Figure 3.2). Note that in practical application, off-axis holography is employed to avoid the superposition of the virtual image and the conjugate image (Leith & Upatnieks, 1965). By tilting the reference wave (or shifting the object), it is possible to spatially separate the virtual image, conjugated image, and the illuminating wave. Thus, Figure 3.4 is more representative of respectively the recording (Figure 3.4a) and reconstruction of a hologram (Figure 3.4b).

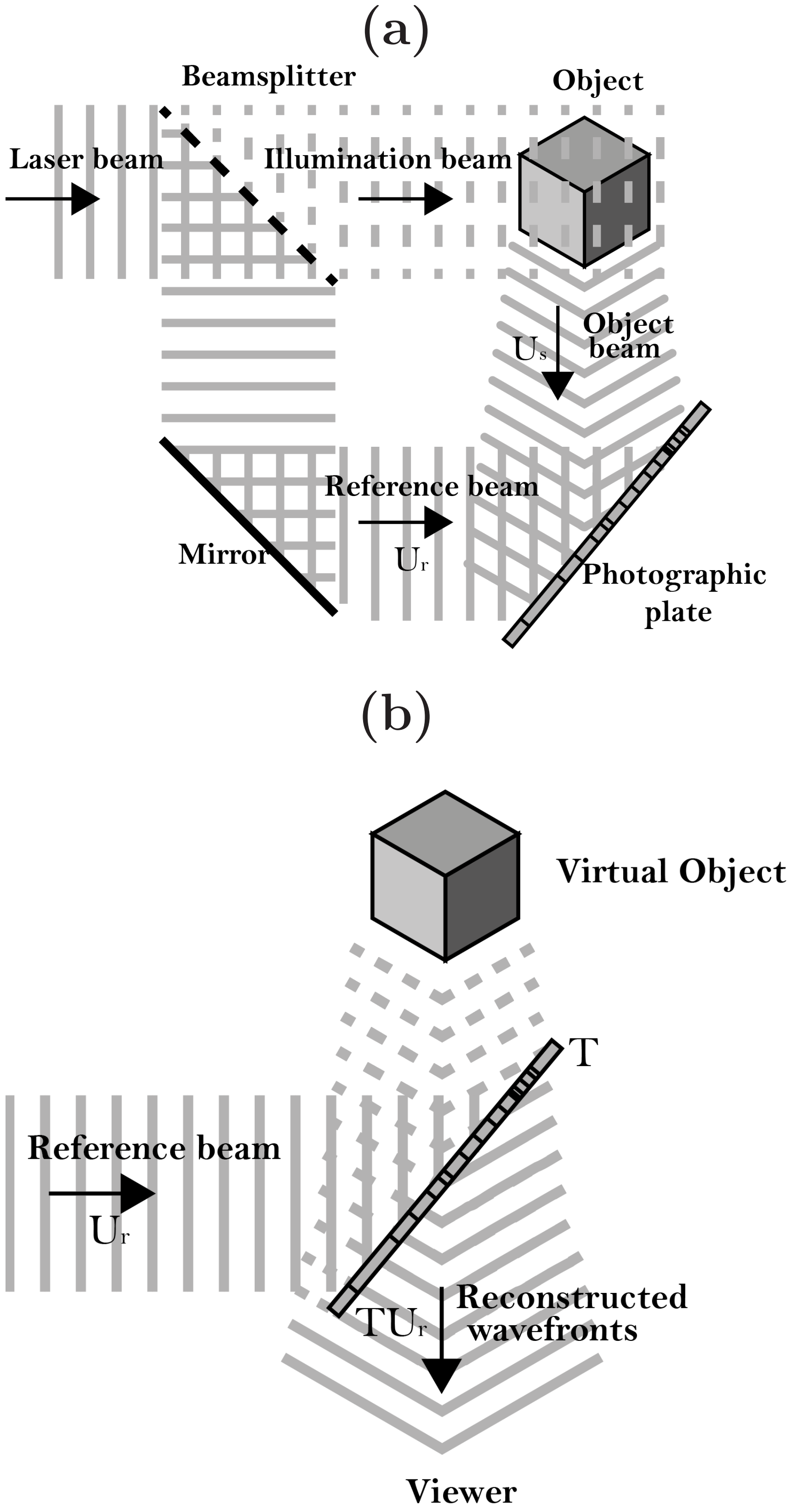

Figure 3.4: *Schematic showing (a) the recording and (b) the reconstruction of a hologram.*

3.1.2 Acoustic holography (seismic imaging)

We are now in a position to compare the recording process of, respectively, a hologram and a seismogram. The basis of a hologram has already been discussed and summarized in Figure 3.4. The corresponding seismic experiment is shown schematically in Figure 3.5. As in the optical case, the object is illuminated (or insonified), and the scattered waves are recorded. However, there is no need for a reference field because both amplitude and phase information are measured. In Figure 3.5, we have assumed an ideal acquisition aperture with receivers evenly distributed across the surface S defining a volume V of space. In a practical case, this aperture will be limited to a plane (or line in 2D) similar to the photographic plate used in optical holography. As already discussed, holography can reconstruct a 3D object based on 2D data (cf. Figure 3.4b). The image is, however, virtual, and is formed in the (human) brain of the viewer. In case of seismic or acoustic holography, a 3D reconstruction of the subsurface can be similarly obtained from 2D data. However, the image is now formed in the computer based on advanced wave-theory concepts.

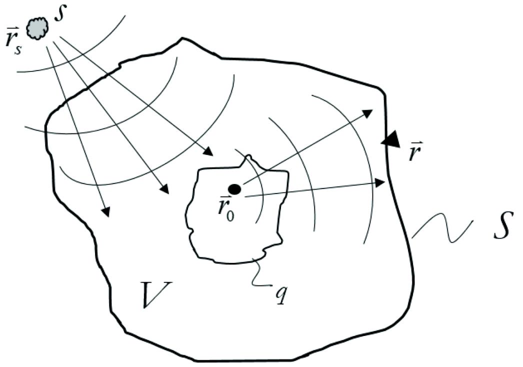

Figure 3.5: *Basic model and acquisition geometry for acoustic holography. We assume an ideal acquisition aperture with receivers evenly distributed across the closed surface S, which defines a volume V. A point source S (located at* $\mathbf{r_s}$ *outside the volume V) illuminates the scatterers q, which generate a scattered field (denoted p_s in the main body of the text), measured by the receivers across S.*

Returning again to Figure 3.5, a point source S is located outside V at a position $\mathbf{r_s}$. It illuminates the scatterers q embedded in the (possible) non-uniform background medium. (One such scattering point is indicated at the location $\mathbf{r_0}$ in Figure 3.5). If the Green's theorem is combined with solutions involving both time-advanced and time-retarded Green's functions, the Porter-Bojarski equation employed in (generalized) holography can be obtained (Porter, 1970; Bojarski, 1983; Thorkildsen et al., 2021):

$$
\begin{aligned}
p_{bp}(\mathbf{r},\mathbf{r_s},\omega) = &\frac{1}{i\omega\rho}\int_s \left[\frac{\partial}{\partial n}G_0^*(\mathbf{r},\mathbf{r}^{''},\omega)p_s(\mathbf{r}^{''},\mathbf{r_s},\omega) - G_0^*(\mathbf{r},\mathbf{r}^{''},\omega)\frac{\partial}{\partial n}p_s(\mathbf{r}^{''},\mathbf{r_s},\omega)\right]dS^{''}\\
=&\frac{1}{i\omega\rho}\int_V G_h(\mathbf{r},\mathbf{r}^{'},\omega)q(\mathbf{r}^{'})dV^{'} \qquad\qquad \forall\mathbf{r}\in V,
\end{aligned}
\tag{3.8}
$$

where G_0 is the Green's function of the background medium, G_0^* its complex conjugated counterpart, $G_h = (G_0 + G_0^*)$ is the homogeneous Green's function, and p_{bp} denotes the back propagated (scattered) wavefield. The physical interpretation of Equation 3.8 is as follows: the illuminating field generated by a point source placed outside the volume V in Figure 3.5 generates a scattered field p_s due to the inhomogeneities embedded in the smooth non-uniform background model. Sensors evenly distributed across the closed surface S (cf. Figure 3.5) measure this scattered field and its gradient, thus assuming an **ideal acquisition aperture**. These measurements can now be propagated back in time to an arbitrary sensor location $\mathbf{r}$ inside the closed volume by use of time-reversed (complex conjugated in the frequency domain) monopole sources G_0^* and dipole sources $\frac{\partial G_0^*}{\partial n}$. In the case of an ideal acquisition aperture, this back-propagated field can also be described analytically by a volume integral involving the homogeneous Green's function G_h and the scatterer distribution q. This relationship breaks down in the case of a limited acquisition boundary commonly employed in seismic acquisition, as discussed by Gelius & Asgedom (2011). For details regarding the derivation of Equation 3.8, the reader is referred to Appendix A in Paper I attached to this thesis. Note that this result is only valid in the absence of evanescent waves.

In the following, we will consider the more realistic case of a limited acquisition aperture. We will then approximate the backpropagation operation by use of the surface integral in Equation 3.8, which is known as the Kirchhoff integral in the seismic literature (Schneider, 1978; Wiggins, 1984; Langenberg, 1987; Esmersoy & Oristaglio, 1988; Schleicher et al., 2007). This surface integral can be further approximated as:

$$
\begin{aligned}
p_{bp}(\mathbf{r},\mathbf{r_s},\omega) = &\frac{1}{i\omega\rho}\int_s \left[\frac{\partial}{\partial n}G_0^*(\mathbf{r},\mathbf{r}^{''},\omega)p_s(\mathbf{r}^{''},\mathbf{r_s},\omega) - G_0^*(\mathbf{r},\mathbf{r}^{''},\omega)\frac{\partial}{\partial n}p_s(\mathbf{r}^{''},\mathbf{r_s},\omega)\right]dS^{''}\\
\cong&\frac{2}{i\omega\rho}\int_s \left[\frac{\partial}{\partial n}G_0^*(\mathbf{r},\mathbf{r}^{''},\omega)p_s(\mathbf{r}^{''},\mathbf{r_s},\omega)\right]dS^{''}\\
\cong&-\frac{2}{\rho}\int_S \left[\frac{|cos[\beta(\mathbf{r}^{''})]|}{c_0(\mathbf{r}^{''}}G_0^*(\mathbf{r},\mathbf{r}^{''},\omega)p_s(\mathbf{r}^{''},\mathbf{r_s},\omega)\right]dS^{''},
\end{aligned}
\tag{3.9}
$$

where $\beta(\mathbf{r}^{''})$ is the angle between the normal to $S^{''}$ at $\mathbf{r}^{''}$ and the ray from $\mathbf{r}^{''}$ to the receiver point $\mathbf{r}$. If we assume a smooth inhomogeneous model, only one such ray exists. The first approximation introduced in Equation 3.9 is valid for a smooth surface $S^{''}$ surrounded by a homogeneous medium. It has been further simplified by the introduction of a high-frequency and far-field assumption.

By analogy with Section 2.1, we assume that the scattering potential can be estimated from a U/D type of imaging condition (assuming limited aperture and "t=0" imaging condition) (shot point migration):

$$\begin{aligned}\langle \alpha(\mathbf{r}) \rangle &= \int_{\Delta\omega} \frac{p_{bp}(\mathbf{r}, \mathbf{r_s}, \omega)}{p_i(\mathbf{r}, \mathbf{r_s}, \omega)} d\omega \\ &= -\frac{2}{\rho} \int_S \int_{\Delta\omega} \left[\frac{|cos[\beta(\mathbf{r}^{''})]|}{S(\omega) c_0(\mathbf{r}^{''})} \frac{G_0^*(\mathbf{r}, \mathbf{r}^{''}, \omega) p_s(\mathbf{r}^{''}, \mathbf{r_s}, \omega)}{G_0(\mathbf{r}, \mathbf{r_s}, \omega)} \right] d\omega dS^{''},\end{aligned} \tag{3.10}$$

where we have assumed an incident wave on the form

$$p_i(\mathbf{r}, \mathbf{r_s}, \omega) = S(\omega) G_0(\mathbf{r}, \mathbf{r_s}, \omega), \tag{3.11}$$

with $S(\omega)$ being the source spectrum. Introducing now the high-frequency assumption and representing the Green's function in the form of (dynamic raytracing):

$$G(\mathbf{r}, \mathbf{r_0}, \omega) \cong A(\mathbf{r}, \mathbf{r_0}) e^{-i\omega t(\mathbf{r}, \mathbf{r_0})} \tag{3.12}$$

with A being the amplitude and τ being the travel time. Combining Equations 3.10 and 3.12 yields

$$\langle \alpha(\mathbf{r}) \rangle \cong -\frac{2}{\rho} \int_S \int_{\Delta\omega} \left[\frac{|cos[\beta(\mathbf{r}^{''})]|}{S(\omega) c_0(\mathbf{r}^{''})} A(\mathbf{r}^{''}, \mathbf{r_s}) e^{i\omega\tau(\mathbf{r}^{''}, \mathbf{r_s})} p_s(\mathbf{r}^{''}, \mathbf{r_s}, \omega) \right] d\omega dS^{''}, \tag{3.13}$$

where $A = A_r(\mathbf{r}, \mathbf{r}^{''}) A_s(\mathbf{r}, \mathbf{r_s})$ is the combined amplitude and $\tau = \tau_r(\mathbf{r}, \mathbf{r}^{''}) + \tau_s(\mathbf{r}, \mathbf{r_s})$ is the total travel time (from source to scatterer and back to receiver). Finally, Equation 3.13 can be written as (inverse Fourier transform at $t = 0$):

$$\langle \alpha(\mathbf{r}) \rangle \cong -\frac{2}{\rho} \int_S \left[\frac{|cos[\beta(\mathbf{r}^{''})]|}{S(\omega) c_0(\mathbf{r}^{''})} A(\mathbf{r}^{''}, \mathbf{r_s}) p_s(\mathbf{r}^{''}, \mathbf{r_s}, \tau) \right] dS^{''}. \tag{3.14}$$

The travel time τ in Equation 3.14 defines the migration operator or diffraction curve. A complete reconstruction can be obtained by also integrating over all source positions. By assuming coincident sources and receivers (zero-offset condition), a corresponding post-stack migration algorithm can be established.

3.1.3 The broken hologram and undersampled seismic data

During the illumination phase of optical holography, each point on the object acts as a diffraction point and generates scattering waves propagating in all directions. These scattered waves, associated with one diffractor, will then spread across the photographic plate. Thus, a single point on the measurement surface has contributions from all points on the object. This implies that a subset of the hologram contains the necessary information to reconstruct a virtual image of the full object. Figure 3.6 shows an example of a broken hologram. It is clear that each subset of the broken hologram can reconstruct the full object. However, it is important to note that some distortions are present.

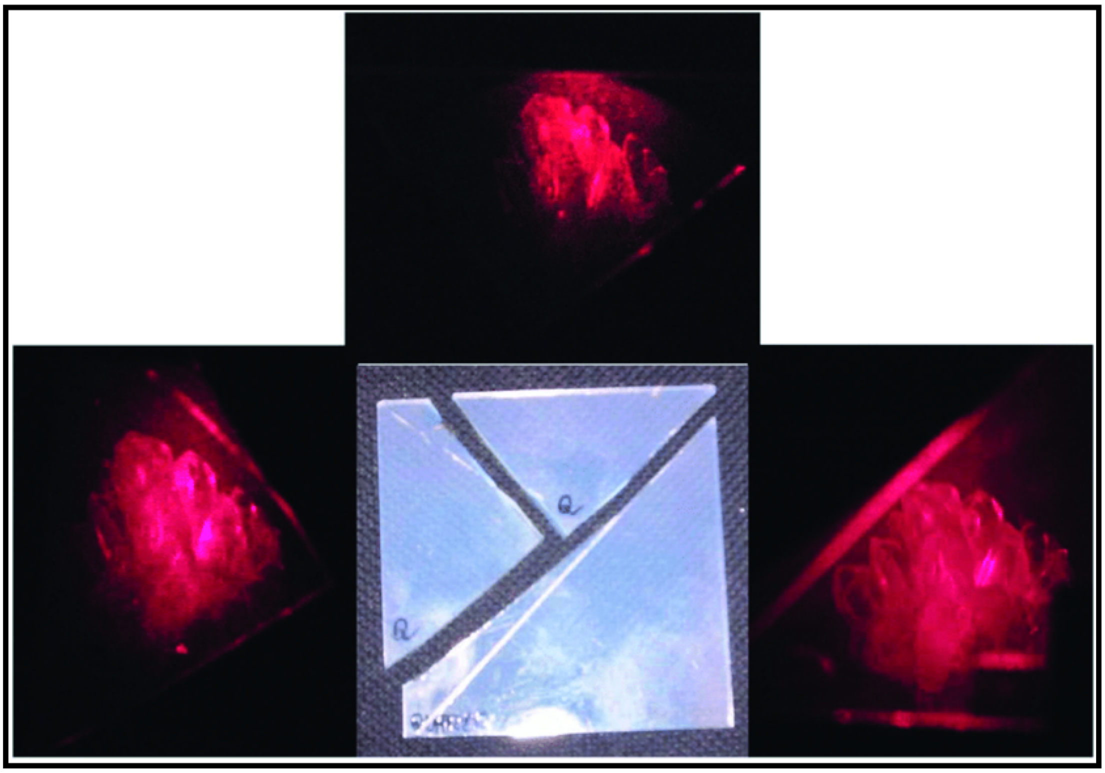

Figure 3.6: *Each piece of the broken hologram contains the necessary information to reconstruct the original virtual object but from slightly different points of view.*

The broken hologram (Figure 3.6) is an example of decimated input data and illustrates that a subset of the original holographic plate can reconstruct the full object. This is due to the fact that the hologram is diffraction dominated. When acquiring seismic data, however, reflections tend to dominate. Thus, in order to achieve a corresponding data decimation employing seismic data, we propose using diffraction-separated data.

3.2 Diffraction separation

Diffractions can be seen as representing the limit of resolution in seismic imaging (cf. Section 2.1). Although it has been pointed out that diffractions carry important information when imaging the subsurface, they are often overlooked in the seismic imaging sequence (Neidell, 1997). This is mostly due to the fact that these events are relatively much weaker than the reflected events. As a consequence, several methods of diffraction separation have been developed. These methods can largely be divided into two groups. One commonly used approach tries to suppress the reflected events directly as part of the migration process (Moser & Howard, 2008; Klokov & Fomel, 2012; Dafni & Symes, 2017). The other main group of techniques attempts to separate the diffractions explicitly before migration (Fomel, 2002; Berkovitch et al., 2009; Asgedom et al., 2012), by use of e.g. plane-wave destruction filters (Fomel, 2002) or diffraction stacking techniques (Berkovitch et al., 2009; Dell & Gajewski, 2011; Asgedom et al., 2012).

In this work, the diffraction-stacking approach has been chosen as the preferred method. Separation of diffractions before migration leaves the user with more flexibility, especially with regards to the choice of imaging algorithm. This technique takes advantage of the fact that reflected and diffracted waves have a distinct and different moveout. By stacking data along diffraction-tailored time operators, the weak diffractions will be enhanced compared to stronger reflections.

Figure 3.7 gives a schematic representation of the difference in moveout for a reflection (black) and diffraction (red) as a function of midpoint and offset. Top right shows a Common Midpoint (CMP) gather taken at a midpoint coinciding with the apex of the diffraction. In this gather, the diffraction behaves like a slow event, with a strong offset-dependent moveout. The same diffraction can be seen to have a much weaker offset-dependent moveout (bottom right), in case the midpoint of the CMP gather does not coincide with the diffraction apex. In addition, direct comparison between the reflected event as seen in the two gathers clearly demonstrates that the moveout of the reflection is virtually unaffected (with exception of the changes in moveout caused by a different intercept time).

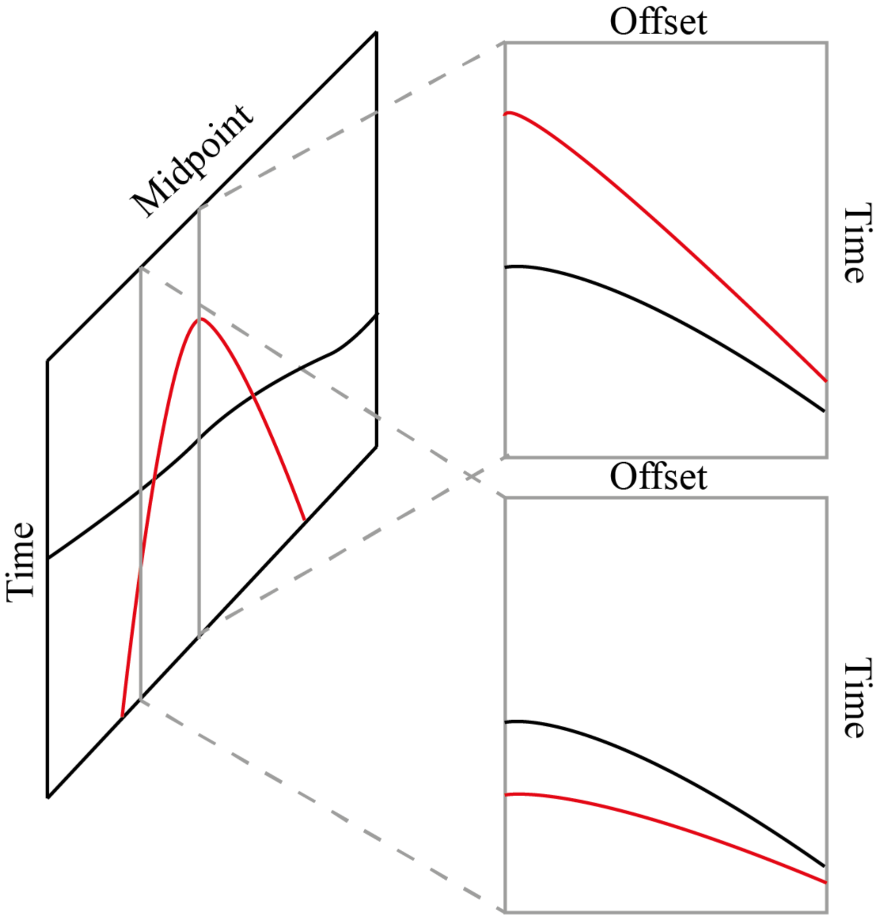

Figure 3.7: *Schematic showing the moveout difference of a reflection (black) and diffraction (red) in a constant velocity medium (offset-midpoint domain).*

As already mentioned, the main idea behind diffraction stacking is to stack the data along travel time curves tailored for diffractions. Several diffraction-tailored moveout equations can be found in the literature (Berkovitch et al., 2009; Dell & Gajewski, 2011; Faccipieri et al., 2016). In this work, the well known Double-Square-Root (DSR) equation has been employed. This is a particularly attractive choice, as it provides an exact solution to the moveout of a diffraction in a homogeneous medium. Moreover, the DSR operator has been shown to perform better than other diffraction-tailored moveout expressions (Faccipieri et al., 2016). In the next section, we start by deriving the DSR equation for the case of a homogeneous medium. We then generalize this result to an effective medium described by an NMO-velocity model and straight rays. Finally, an analytical link between the parameters is introduced to increase the robustness of the separation algorithm.

3.2.1 The Double-Square-Root (DSR) equation

Consider a scatterer embedded in a homogeneous medium with velocity V (Figure 3.8). The travel time moveout measured by a source-receiver pair with midpoint

m and half offset h is then

$$t(m,h) = \sqrt{\frac{(m_d - m - h)^2 + d^2}{V^2}} + \sqrt{\frac{(m_d - m + h)^2 + d^2}{V^2}}, \tag{3.15}$$

where m_d and d describe respectively the lateral location and depth of the scatter point. The first term in Equation 3.15 is the travel time from the source point down to the scatter point, while the second term describes the corresponding travel time from the scatter point back to the receiver. In case of a coinciding source and receiver pair (zero-offset, ZO), Equation 3.15 simplifies to

$$t_0(m_0, h = 0) = 2\sqrt{\frac{(m_d - m_0)^2 + d^2}{V^2}}. \tag{3.16}$$

This equation defines a ZO reference ray, i.e the travel time for a ray going from m_0 to the scatter point and back to m_0 (cf. Figure 3.8).

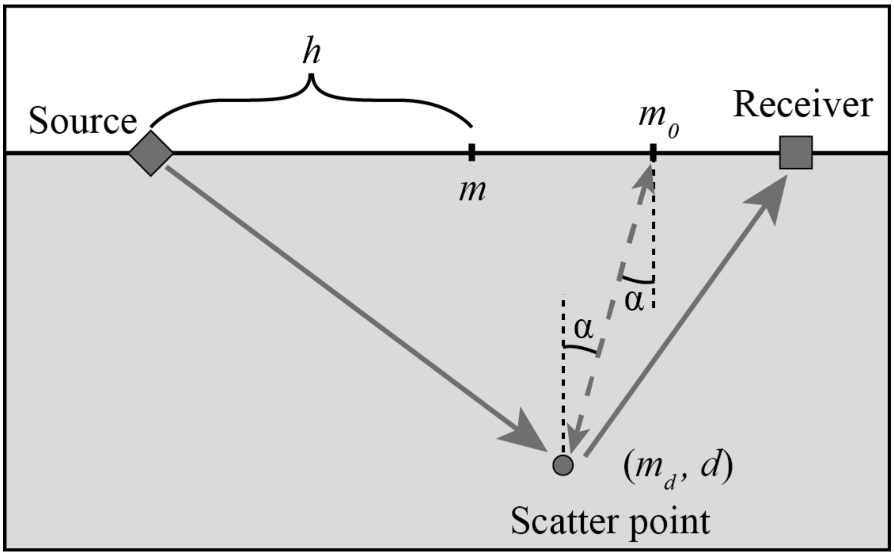

Figure 3.8: *A scatter point at (m_d, d) embedded in a constant velocity medium with velocity V. The lateral midpoint of the source and receiver pair is defined by m, and the half offset is given by h. The dashed line defines a ZO reference ray, which is associated with an emergence angle α.*

By introducing the notation $\Delta m = m - m_0$, we can rewrite Equation 3.15 as

$$\begin{aligned} t(m,h) = &\sqrt{\frac{(m_d - m_0)^2 - 2(m_d - m_0)(\Delta m - h) + (\Delta m - h)^2 + d^2}{V^2}} \\ &+ \sqrt{\frac{(m_d - m_0)^2 - 2(m_d - m_0)(\Delta m + h) + (\Delta m + h)^2 + d^2}{V^2}}, \end{aligned} \tag{3.17}$$

which can be further simplified by use of Equation 3.16

$$
\begin{aligned}
t(m,h) = &\sqrt{\frac{t_0^2}{4} - 2\frac{(m_d - m_0)(\Delta m - h)}{V^2} + \frac{(\Delta m - h)^2}{V^2}} \\
&+\sqrt{\frac{t_0^2}{4} - 2\frac{(m_d - m_0)(\Delta m + h)}{V^2} + \frac{(\Delta m + h)^2}{V^2}}.
\end{aligned}
\tag{3.18}
$$

Introducing now a parameter A defined as (α being the emergence angle of the ZO reference ray in Figure 3.8):

$$
A = 4\frac{(m_0 - m_d)}{t_0 V^2} = \frac{2 sin\alpha}{V},
\tag{3.19}
$$

in Equation 3.18 gives:

$$
\begin{aligned}
t(m,h) = &\frac{1}{2}\sqrt{t_0^2 + 2At_0(\Delta m - h) + \frac{4(\Delta m - h)^2}{V^2}} \\
&+\frac{1}{2}\sqrt{t_0^2 + 2At_0(\Delta m + h) + \frac{4(\Delta m + h)^2}{V^2}} \\
&=\frac{1}{2}\sqrt{t_0^2 + 2At_0(\Delta m - h) + A^2(\Delta m - h)^2 + (\frac{4}{V^2} - A^2)(\Delta m - h)^2} \\
&+\frac{1}{2}\sqrt{t_0^2 + 2At_0(\Delta m + h) + A^2(\Delta m + h)^2 + (\frac{4}{V^2} - A^2)(\Delta m + h)^2}
\end{aligned}
\tag{3.20}
$$

Finally, by introducing source and receiver coordinates explicitly through the definitions $\Delta s = \Delta m - h$, $\Delta g = \Delta m + h$, we obtain

$$
t(m,h) = \frac{1}{2}\sqrt{\Big[t_0 + A\Delta s\Big]^2 + C\Delta s^2} + \frac{1}{2}\sqrt{\Big[t_0 + A\Delta g\Big]^2 + C\Delta g^2},
\tag{3.21}
$$

which is the well-known DSR operator for a constant medium, with C defined as (also making use of Equation 3.19):

$$
C = \frac{4}{V^2} - A^2 = \frac{4}{V^2}\Big(1 - sin^2\alpha\Big) = \frac{4}{V^2}cos^2\alpha.
\tag{3.22}
$$

Equation 3.21 describes the moveout of a diffraction event based on the two stacking parameters A and C. From Equation 3.22, it follows that the two parameters A and C are linked through an analytical expression. This relationship is, however, only valid for a homogeneous overburden. We now consider a generalization to an effective medium model based on NMO-velocity and straight rays. We follow (Asgedom et al., 2012) and make the substitution

$$
C = \frac{4}{V_{nmo}^2}cos^2\alpha,
\tag{3.23}
$$

where V_{nmo} is the NMO-velocity. Equation 3.23 does allow for an inhomogeneous overburden. However, it does not account for the effects of dipping reflectors. The reflectors, which are generally much stronger than the diffractions, will dominate the velocity analysis. Thus, in the case of dipping reflectors, the obtained velocity will be an apparent velocity. This distortion can be accounted for by correcting the velocity by the Levin factor (Levin, 1971):

$$C = \frac{4}{(V_{nmo} cos(\theta))^2} cos^2\alpha, \tag{3.24}$$

with θ being the dip angle. Although this relationship still depends on two parameters (emergence angle α and the Levin factor), the parametric link increases the robustness of the search significantly. Moreover, the parametric search can be further narrowed by using general knowledge of the area. Consider a stratigraphic earth model, i.e., $cos(\theta) = 1$, and assume that the velocity obtained in the velocity analysis is close to the NMO-velocity. It then follows from equation 3.24 that $C = \frac{4}{(V_{nmo}/cos\alpha)^2}$, where it can be seen that the velocity is modified by the emergence angle of a possible diffraction. This modification of the velocity is important in order to find the most optimal stacking parameters for the flanks of the diffractions.

The diffraction time-operator given by equation 3.21 represents the travel time, t, of a nearby paraxial ray to the ZO reference ray with travel time t_0 and midpoint m_0. As it appears, this operator allows for a nearby ray with a displaced midpoint $(m - m_0)$ and a finite offset h. The two stacking parameters to be determined, A and C, are defined by Equations 3.19 and 3.24. Note that the velocity V in Equation 3.19 is the surface velocity (water velocity in marine seismic) since α is the emergence angle at the surface. We assume that a conventional velocity analysis has been carried out, so that the NMO-velocity V_{nmo} in Equation 3.24 is already known. It then follows from Equations 3.19 and 3.24 that the stacking parameters can be parametrized by use of the emergence angle α and dip angle θ.

The optimal set of stacking parameters are selected based on a coherency measure. However, the parametric search can be affected by several user-defined input parameters. The most obvious of these is the range of values we allow the emergence angle α and dip angle θ to take. An equally important user-defined input parameter is related to the aperture in midpoint (Δm) and half-offset (h). Faccipieri et al. (2016) found that use of a large aperture (equal in offset and midpoint, and constrained by the NMO stretch) will generally provide a better separation result in the case of diffraction enhancement employing the DSR operator (3D case). Moreover, by employing a small aperture, it is more likely that the stronger reflections will dominate the parameter search. Thorkildsen (2019) did a similar study of stacking apertures, and found that the separation algorithm was more sensitive to an increase in offset aperture than midpoint aperture, with results quickly deteriorating for large offset apertures. Thus, we have adopted the strategy of using a large midpoint aperture, and a comparatively smaller offset aperture.

3.2.2 Coherency measure

The stacking parameters can be found by testing all possible combinations of parameters and select the most optimal set based on a coherency measure. In this work, we have employed the well-known semblance criterion, which can be stated as (Neidell & Taner, 1971):

$$S = \frac{\sum_{i=k-N/2}^{k+N/2} \left(\sum_{j=1}^{M} f_{ji} \right)^2}{M \sum_{i=k-N/2}^{k+N/2} \sum_{j=1}^{M} f_{ji}^2}. \tag{3.25}$$

In Equation 3.25, S is the semblance value, k denotes a central time index in a time window defined by the window size N, M is the total number of traces in the data volume, and f_{ji} is the sample value at time index i and trace number index j. In essence, semblance gives a measure of the energy in the stack compared to the total input energy (Yilmaz, 2001). Thus, a low signal-to-noise ratio will result in a low semblance value. However, as the semblance criterion yields a high value (close to 1) for all coherent events, the operator can be tricked by coherent noise and multiples. In order to extract weak events, such as diffractions, it is important to employ a large data volume. This will inevitably lead to an increase in computational time when expanding the data volume. Evaluating Equation 3.21 in its original form reveals that the stacking surface is two dimensional, with dimensions of offset and midpoint. However, the semblance value is actually calculated based on a three-dimensional data volume, as the semblance value is calculated in a time window (cf. Equation 3.25). One possible way to decrease the computational time is to adopt a pragmatic search approach, where the different stacking parameters are found in separate domains (i.e midpoint or offset domain).

3.2.3 Workflow for diffraction separation

The full workflow for diffraction separation used in this work is outlined in Figure 3.9. It is important to note that the midpoint search with the analytical link (Equation 3.24) is carried out employing the zero-offset counterpart of Equation 3.21, which can be written explicitly as

$$t(m, h = 0) = \sqrt{\Big[t_0 + A\Delta m\Big]^2 + C\Delta m^2}. \tag{3.26}$$

Moreover, this processing step is followed by a refining search in midpoint and offset domains employing the full DSR equation (Equation 3.21). However, due to the pragmatic search approach, the most optimal stacking parameters cannot be guaranteed in a global sense. Subsequently, the data are stacked with the refined stacking parameters along the stacking surface calculated from Equation

3.21. Even after creating the diffraction-enhanced stack, some artifacts may be present. An effective method of minimizing such artifacts is to introduce a threshold based on the semblance value of the extracted stacking parameters.

One simple way of performing this thresholding can be to weight the diffraction enhanced stack with the semblance value (i.e the thresholded stack is the product of the diffraction-enhanced stack and the semblance panel). Another possible approach is to discard all data points below a certain semblance value. The first approach is preferred for simpler datasets, as the data alteration is comparatively less destructive. For more difficult datasets, such an approach can lead to an unsatisfactory separation result; in this case the second approach should be employed.

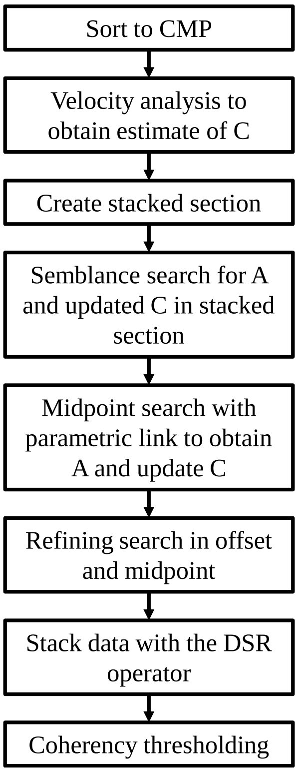

Figure 3.9: *Workflow for diffraction separation by diffraction stacking employing the DSR operator.*

3.2.4 Data example

The seismic field data presented in this section were provided by Lundin Norway (now AkerBP), and are from the southwestern Barents Sea. This survey was acquired with an unconventional marine split-spread geometry denoted as TopSeis. For a description of the TopSeis acquisition geometry in general and the dataset employed in this work specifically, the reader is referred to Vinje et al. (2017) and Thorkildsen (2019) respectively.

As briefly mentioned, the first steps of the diffraction separation workflow includes the forming of a zero-offset stack (cf. Figure 3.9). Direct comparison between the NMO stack (Figure 3.10a) with the corresponding DSR stack (Figure 3.10b) reveals that a large number of diffractions are masked by reflections in the conventional NMO stack. The DSR stack was obtained by using a large midpoint aperture ($\approx \pm 1800$m, constant in time) and a small half-offset aperture ($\approx$ 200-700m, time varying). The emergence angle α was set to vary within a large range of ± 80 degrees, while the dip angle θ was allowed to vary between 0 and 10 degrees. However, due to the abundance of diffractions, the diffraction-enhanced stack has a smeared and blurred appearance. Note that the DSR stack in Figure 3.10b is plotted with the absolute value for display purposes. In order to avoid the artifacts seen in the raw diffraction-enhanced stack, we now introduce a thresholding based on semblance.

Each search for the stacking parameters A and C in the different domains (i.e midpoint domain or midpoint-offset/multi domain) is accompanied by its own coherency measure. Thus, each of these coherency maps can be employed to threshold the final output stack. However, from experience gained using the field data, application of the coherency map measured during the midpoint search only gave the overall best thresholding result. The initial parameters, obtained through a midpoint search employing the analytical link (cf. Equations 3.19 and 3.24), are updated in the refining multi-domain search. We therefore perform a final hi-fi midpoint search, forming a closed loop to ensure maximum separation. However, even after employing the closed loop workflow described above, thresholding with the refined midpoint semblance (Figure 3.10c) gave an unsatisfactory separation result. By closely examining Figure 3.10c, it is clear that the apexes of the diffractions are characterized by high semblance. However, the flanks of the diffractions are characterized by a much lower semblance. As briefly mentioned, the amplitude of an event will impact its corresponding semblance value, and the comparatively weaker flanks will therefore be associated with a lower semblance value. Thus, there is no single optimal thresholding value for the entire image.

As a pragmatic approach, we propose to normalize the semblance panel by use of Automatic Gain Control (AGC), and employ this type of semblance panel for thresholding. Figure 3.10d shows the AGC type of semblance panel (20ms time window), while Figure 3.10e shows a thresholding mask calculated by setting a cutoff of 1.015 in Figure 3.10d. The thresholded stack is now formed as the elementwise (Hadamard) product of the raw DSR stack and the thresholding mask (cf. Figures 3.10b, e and f).

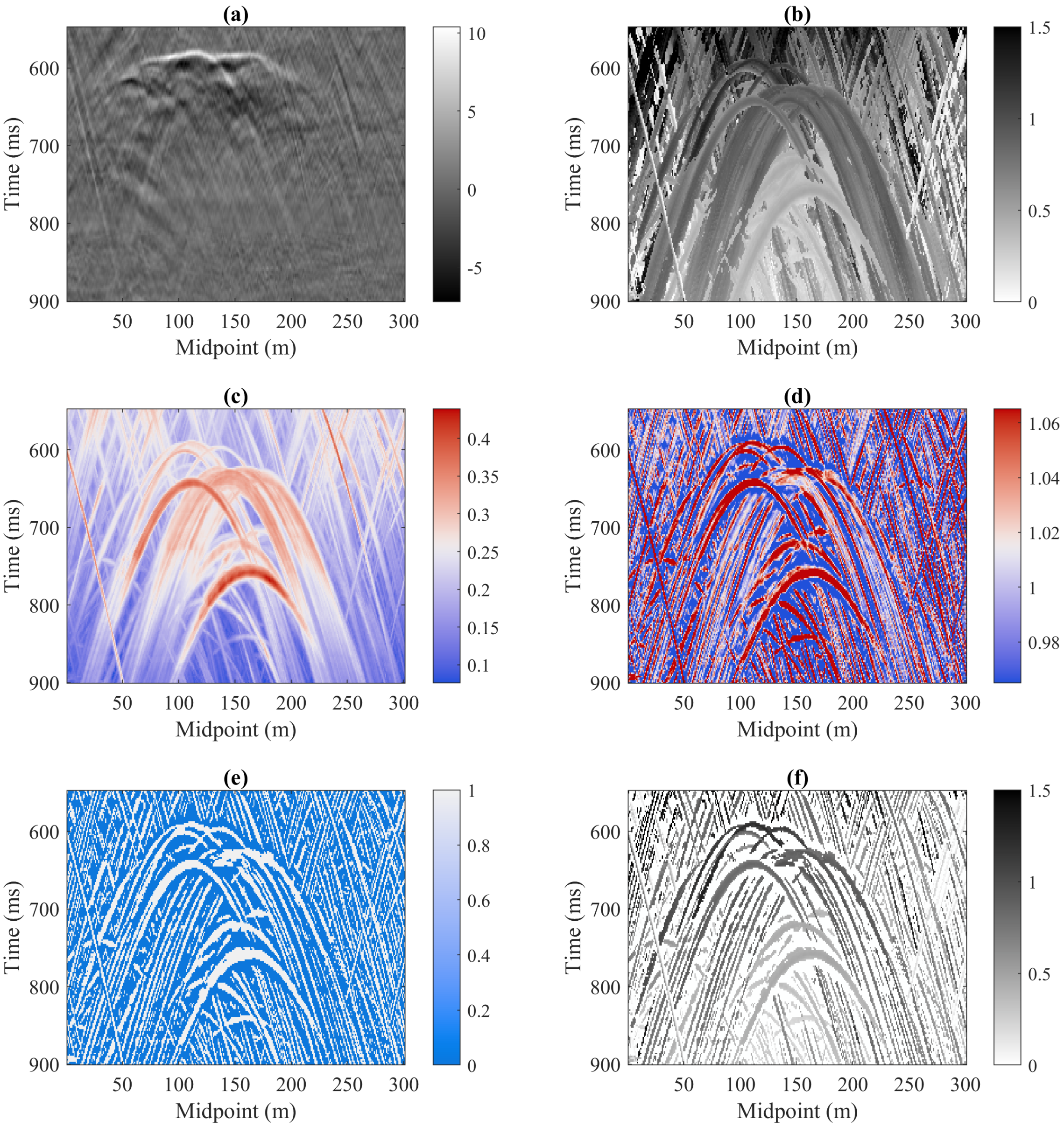

Figure 3.10: *(a) NMO stack, (b) DSR stack (absolute value), (c) Semblance after a refining midpoint search, (d) the corresponding midpoint Semblance after employing AGC (Automatic Gain Control), (e) thresholding mask, and (f) DSR stack (absolute value) after thresholding employing the mask shown in (e). The DSR stack was obtained by using a midpoint aperture of* $\approx \pm 1800m$ *(constant in time) and a half-offset aperture of* $\approx$ *200-700m (time-varying).*

3.3 Holistic migration in practice

Seismic holography is based on the Porter-Bojarski integral formulation of back-propagation. It is known within the seismic community as Kirchhoff migration. Each point in the reconstruction is then obtained by adding parts of the input data along a curve determined by the migration operator (pre- or post-stack). In the following, we will consider 2D post-stack migration only, although the basic concept can be easily extended to 3D and pre-stack data as well. The ZO migration operators (gray dashed curves in Figure 3.11a) are in practice found by treating each image point as a potential scatterpoint, and calculating its travel time to the surface by use of a velocity model. The most common "filtering" used in a conventional Kirchhoff implementation is to limit the aperture of the migration operators. By taking the data that falls along the travel-time curves for all image points corresponding to a vertical image trace, it is possible to form a migration operator panel (cf. Figure 3.11b) (after horizontalization of the time coordinate). Formation of migration operator panels is not commonly done. However, due to imperfections in velocities, possible multipathing, and model complexity, use of filtered and selected parts of the operator may lead to improvements in imaging (Tabti et al., 2004). It is also possible to suppress noise directly in the image domain by weighting the migration with the semblance (cf. Section 3.2.2) of the migration operators (Schwarz, 2019). The imaged trace can be formed by horizontal summation of the migration operator panel (Figures 3.11b and c). Note that the imaged trace contains both operator noise and a false event in addition to the real seismic events. As previously mentioned, unless there is an infinite frequency band and an ideal aperture, a diffraction-limited focus will always be the result from seismic imaging. Moreover, the operator noise in the imaged trace can also be seen as a consequence of the frequency band and aperture.

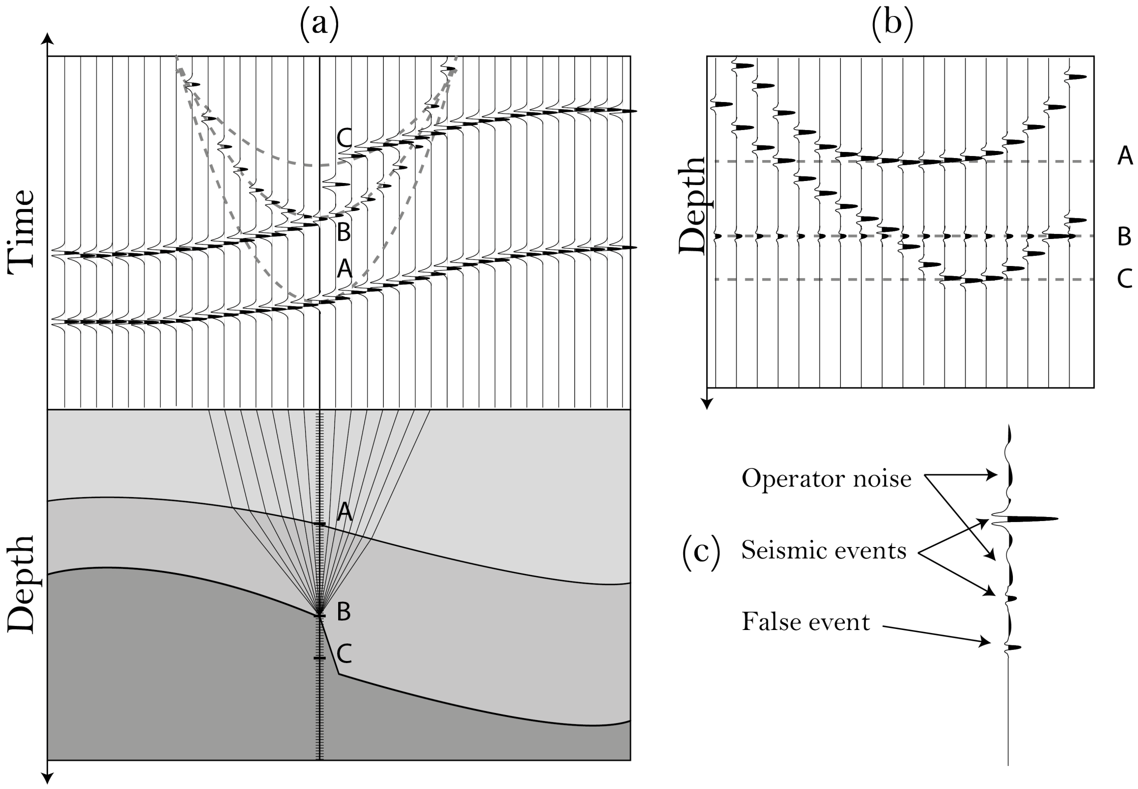

Figure 3.11: *(a) Depth model (bottom) with the corresponding zero-offset seismic. The Kirchoff migration algorithm treats each image point as a potential scatterpoint. The image is formed by summation of data falling along this diffraction curve. By taking the data that falls along the travel time curves for all image points in one trace, it is possible to form a migration operator panel (b) (after horizontalization of the time coordinate). Horizontal summation of the data in this gather forms the image trace (c). Note also the three events (A, B, and C) indicated in the depth model. The travel time curves associated with scatterpoints at these locations are indicated by the gray dashed curves in the zero offset time section and the migration operator panel.*

Figure 3.12 shows an example of a Kirchhoff migration where we have introduced a regular spatial undersampling. By directly comparing Figures 3.11 and 3.12, it is clear that the regular undersampling results in fewer traces in the migration operator panel, which further results in an imaged trace with more operator noise. Note that even though we have undersampled the input data, this undersampling does not necessarily carry over to the image domain. In other words, it is possible to migrate sparsely sampled input data onto a densely sampled image domain. In the literature, this process is denoted holistic migration (Robinson, 1998, 2018). Schwarz (2019) shows a simple data example of holistic migration with emphasis on diffractions. This work seems to be carried out independently, as it makes no mention to the previous publications.

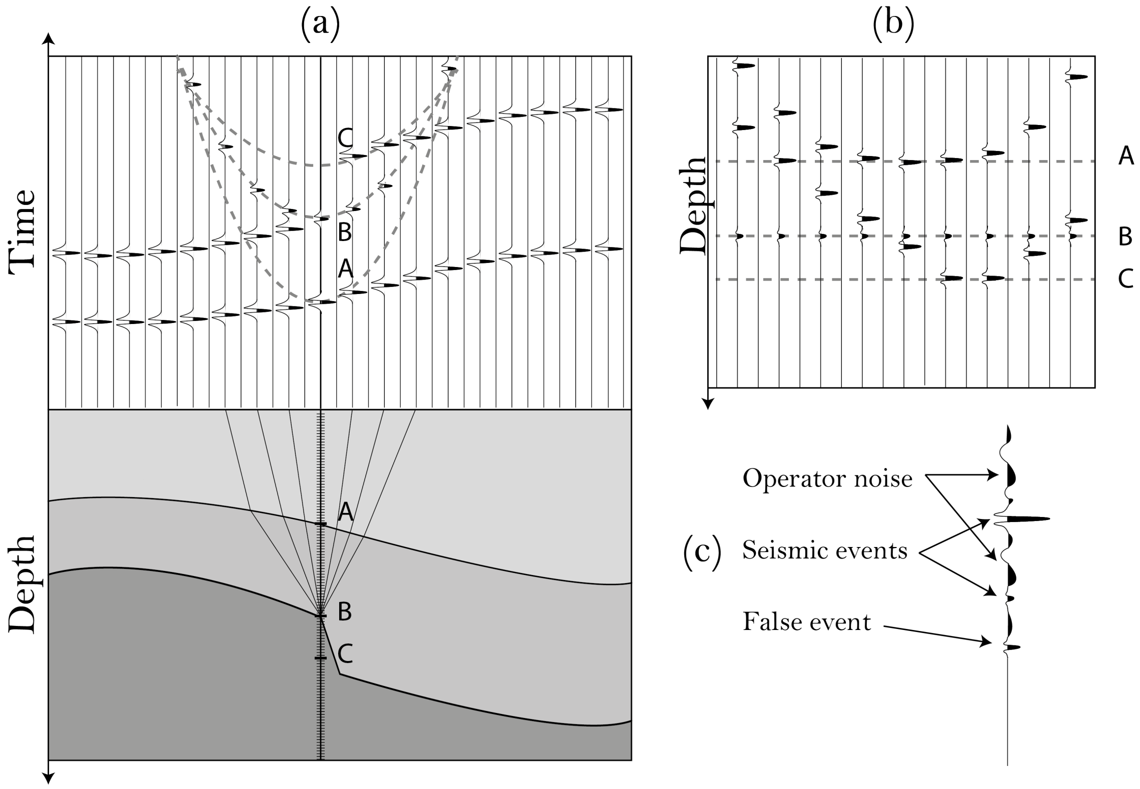

Figure 3.12: *Schematic showing the concept of holistic migration.*

In the schematic example of holistic migration shown in Figure 3.12, we propose a regular undersampling of the input data. However, the working principle behind holistic migration and the effects of undersampling is most easily explained by the use of a simple data example. Consider a single diffractor with the corresponding well-sampled ZO section as shown in Figure 3.13a. Application of acoustic holography (e.g., Kirchhoff migration) gave the well-focused image shown in Figure 3.13b where both the input and reconstructed image were sampled at 6.25m. It should however be noted that the reconstruction contains some artifacts around the well-focused diffractor due to the limited aperture. In a conventional migration, with a more complex model, such artifacts will mostly be covered by other events. This observation also highlights that Kirchhoff migration relies on the destructive interference of events out of focus, and constructive interference of focused events. By increasing the number of input traces, these artifacts will be reduced. However, due to the limited acquisition aperture and frequency band, such artifacts will always be present when imaging seismic data.

Figure 3.13c shows the input data in Figure 3.13a regularly subsampled by a factor of 16 (100m). Application of the basic idea of holistic migration gave the image shown in Figure 3.13d, where the seismic image (output) is computed with a dense sampling of 6.25m. Direct comparison between conventional and holistic migration reveals a well-focused diffraction in both cases (cf. Figures 3.13b and d). However, due to the regular undersampling, the holistic migration also shows superimposed coherent noise (Figure 3.13d). In order to more properly evaluate the effects of undersampling, we also show an example of random decimation (cf. Figures 3.13e and f). In the cases of both regular and random decimation, severe artifacts are present. However, these artifacts manifest differently. The noise pattern obtained by regular undersampling is symmetric, while the random undersampling is less coherent as expected.

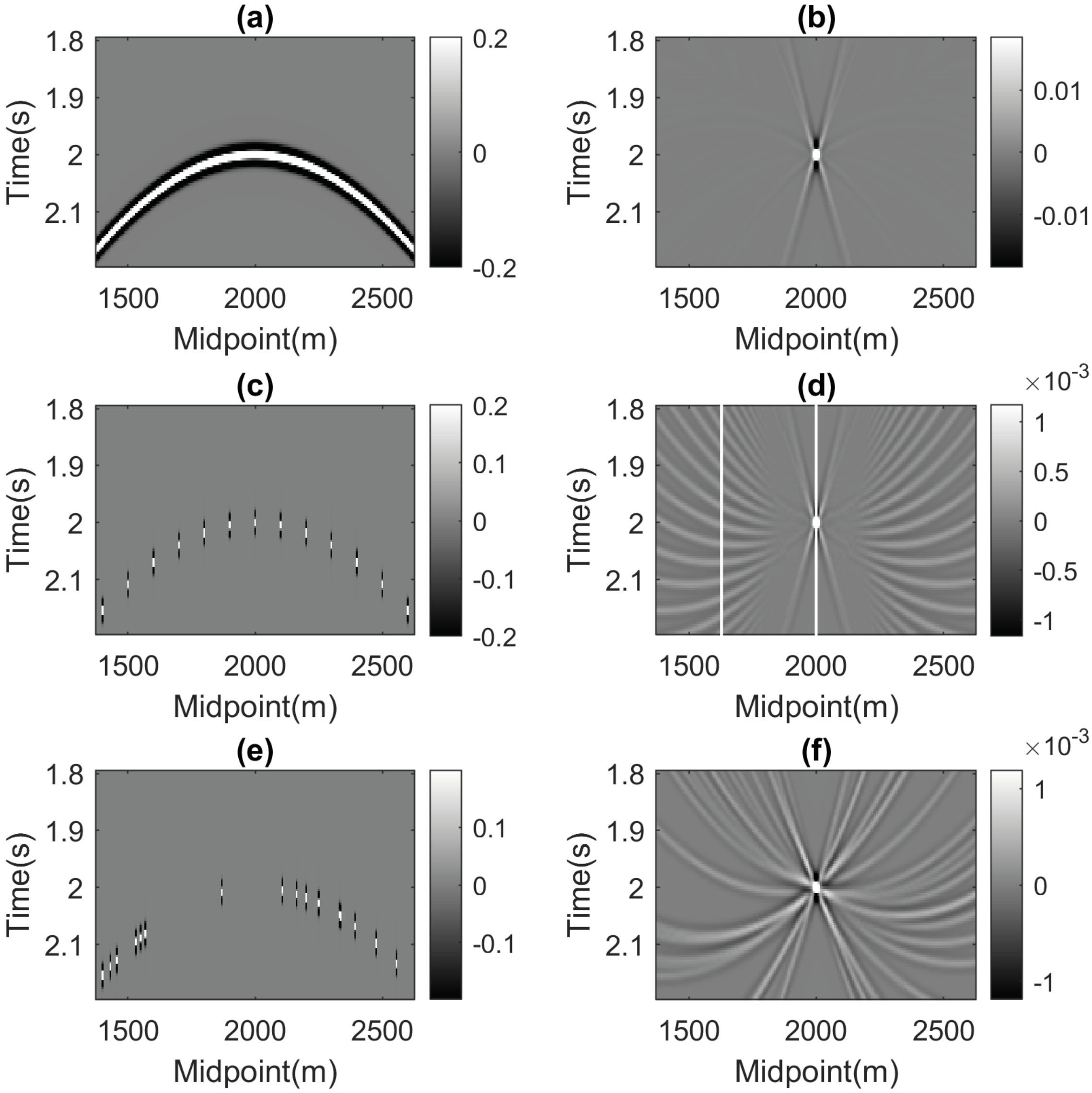

Figure 3.13: *Input data (left column) and imaged section (right column) for a conventional migration (a and b), holistic migration with regular undersampling (c and d) and holistic migration with random undersampling (e and f). All migrations are carried out employing the full aperture of (*$\pm 2000m$*).*

Figure 3.14 shows four examples of holistic migration with varying aperture and subsampling scheme. The top row (Figures 3.14a and b) shows the images obtained from the regular and random subsampling respectively (cf. Figures 3.13c and e), but with a limited aperture ($\pm 1000m$). Figures 3.14c and d show the images obtained by employing the same data selection as the top row, but with an absolute aperture of $500m$.

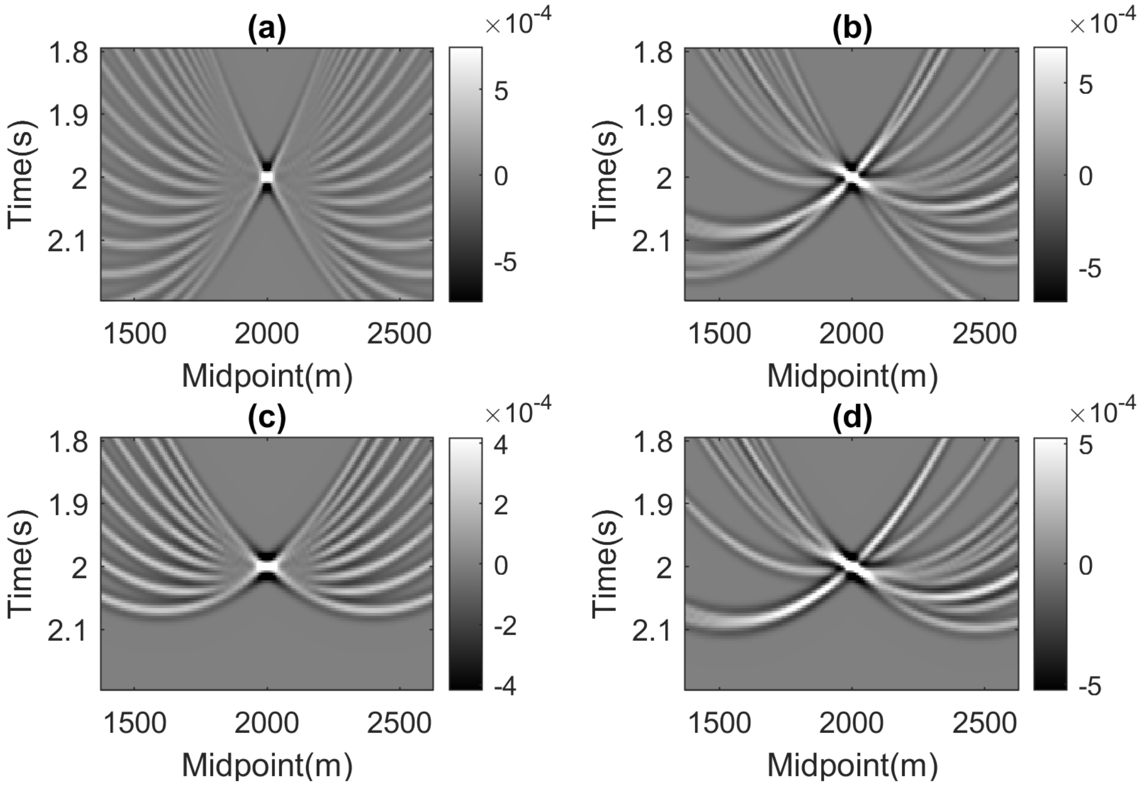

Figure 3.14: *Holistic migration with regular undersampling (a and c) and random undersampling (b and d). All examples use the same data subset as presented in Figure 3.13. However, the aperture is limited to* $\pm1000m$ *in the top row and further limited to* $\pm500m$ *in the bottom row.*

As previously mentioned, the most common filtering employed in an integral type of seismic imaging is to introduce a dip-limited aperture. However, in order to retain the character of the image obtained from conventional imaging (cf. Figure 3.13b), additional processing is required. This PhD study proposes a novel approach based on median filtering of the migration operator panels. Consider now a migration operator panel that coincides with a diffraction point (location indicated by the rightmost white line in Figure 3.13d). In such a case, the diffraction point is in focus and is defined by a large Fresnel aperture that constructively interferes when horizontally summing the operator panel (Figure 3.15a). Figure 3.15c shows a migration operator panel which does not coincide with the diffraction point (leftmost white line in Figure 3.13d). Stacking of this panel should ideally interfere destructively. This is indeed the fundamental concept of Kirchhoff migration: constructive interference of events in focus, and destructive interference of events out of focus. However, due to the severe downsampling associated with holistic migration, unfocused events will not be properly extinguished. However, the introduction of a simple median filtering of the migration operator panels effectively reduces the impact of destructive interference. Figures 3.15b and d show the corresponding migration operator panels after such median filtering, and reveals that the median filter has removed the operator noise. The final imaged trace is subsequently formed by stacking this operator panel.

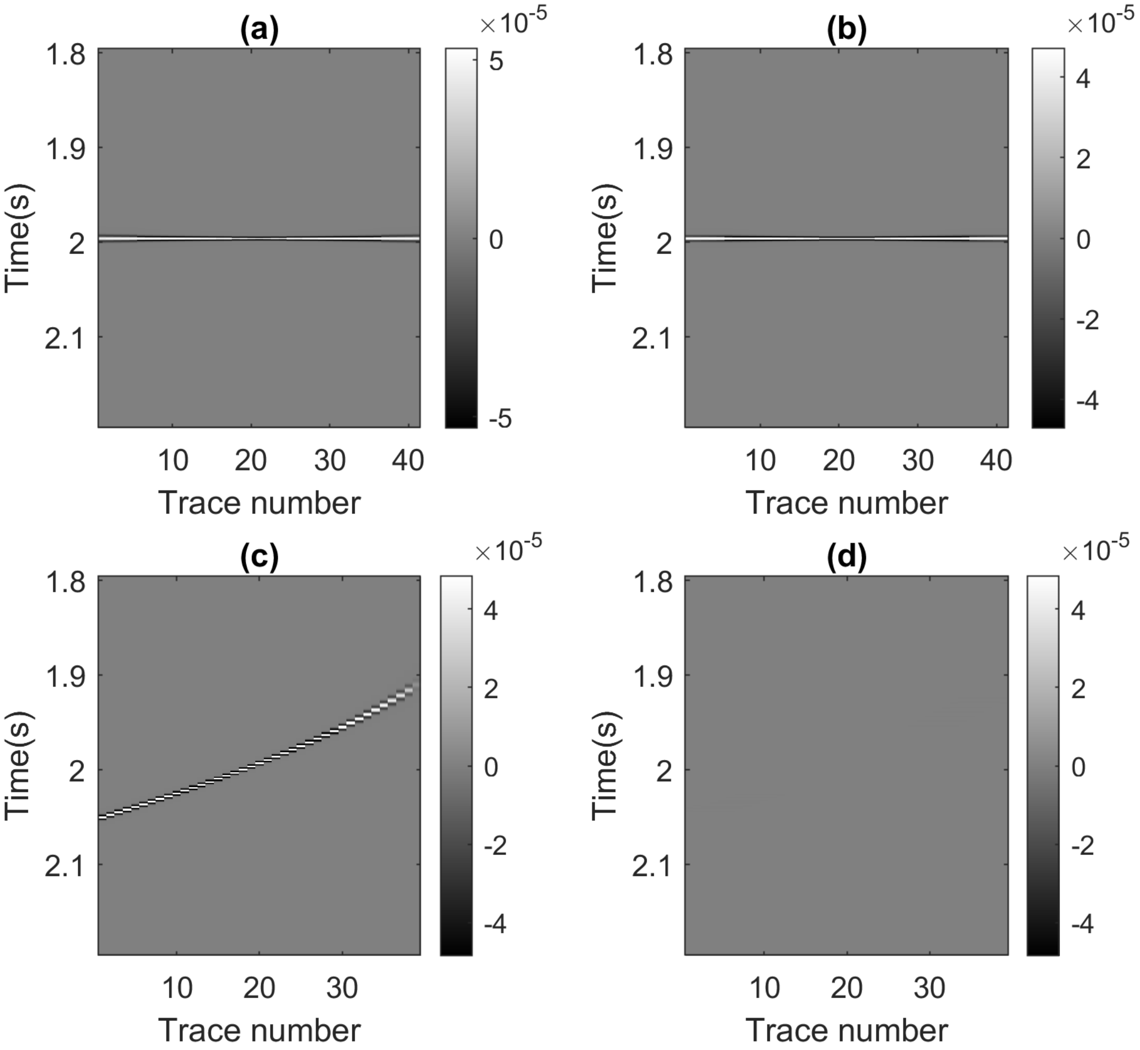

Figure 3.15: *Migration operator panels coincident (a and b) and offset by* ≈ 500 *meters (c and d) from the diffraction. The operator panels on the left and right hand side are depicted respectively before and after median filtering (filter length of 11 samples). The location of the gathers are shown in Figure 3.13d.*

Consider now the introduction of median filtering of the operator panels for the data examples shown in Figures 3.13 and 3.14. The resulting images are displayed in Figure 3.16, where we have also introduced median filtering in the case of conventional migration to make the comparisons most fair. It is evident that median filtering removed most of the noise in all cases. However, the best overall result was obtained by adopting regular undersampling and using the full available aperture. Figures 3.16d through g show that limiting the aperture (or, more accurately, removing the flanks of the diffraction) results in lower resolution. The filtering introduced for each of the cases is determined by the user, and can be labor-intensive to find. Thus, in order to more easily determine the optimal processing parameters, a graphical user interface was developed as a part of this study.

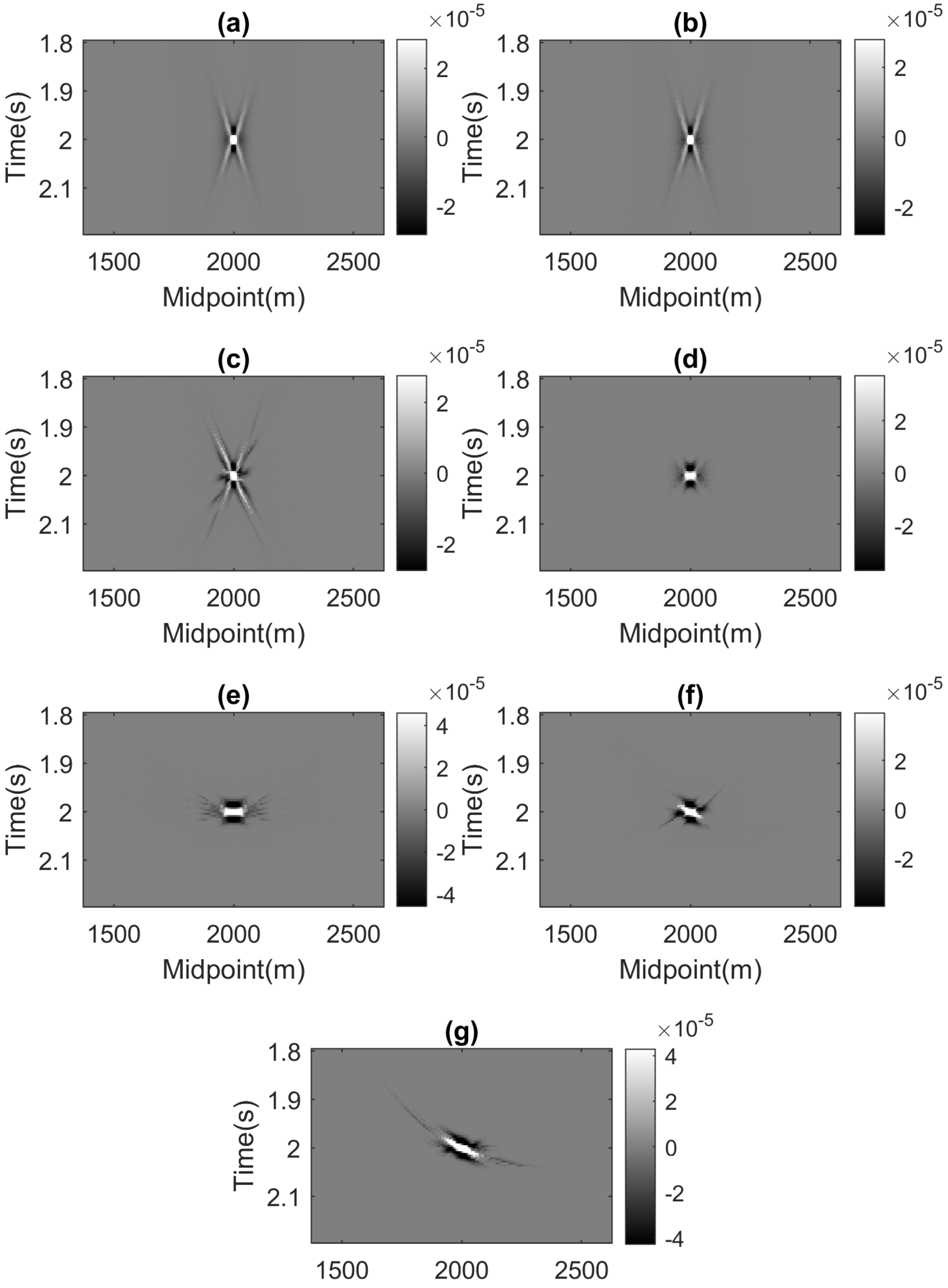

Figure 3.16: *Holistic migration with median filtering of the migration operators. The figures are organized as follows: (a) Conventional migration, (b) holistic migration with regular undersampling, (c) holistic migration with random undersampling, (d) holistic migration with regular undersampling but limited aperture (±1000m), (e) holistic migration with regular undersampling but limited aperture (±500m), (f) holistic migration with random undersampling but limited aperture (±1000m), and (g) holistic migration with random undersampling but limited aperture (±500m).*

3.4 User interface

In order to more easily tune the processing parameters for holistic migration, a simple user interface (UI) was developed. This UI takes the migration operator panels (cf. Figures 3.11, 3.12 and 3.15) and allows the user to apply some simple processing of the panels before final summation. Figure 3.17 displays a snapshot of the UI, which can be divided in two main sections: data display and user-determined input parameters. The data display (marked with A through E in Figure 3.17) includes the raw migration operator panel (A) along with the filtered panel (B) and the corresponding image trace output from this filtered panel (C). Moreover, it also includes a filtered section (D) and the raw summation (stack) (E). The input parameter section allows the user to choose which panel to display (F), filter length (G) and type of filtering (H), which updates interactively the operator panel and image trace displays. However, to decrease the computational burden, the user interface only updates the complete filtered section after a button click (I). Moreover, it is also possible to limit the data to a target area, thus further decreasing the computational burden.

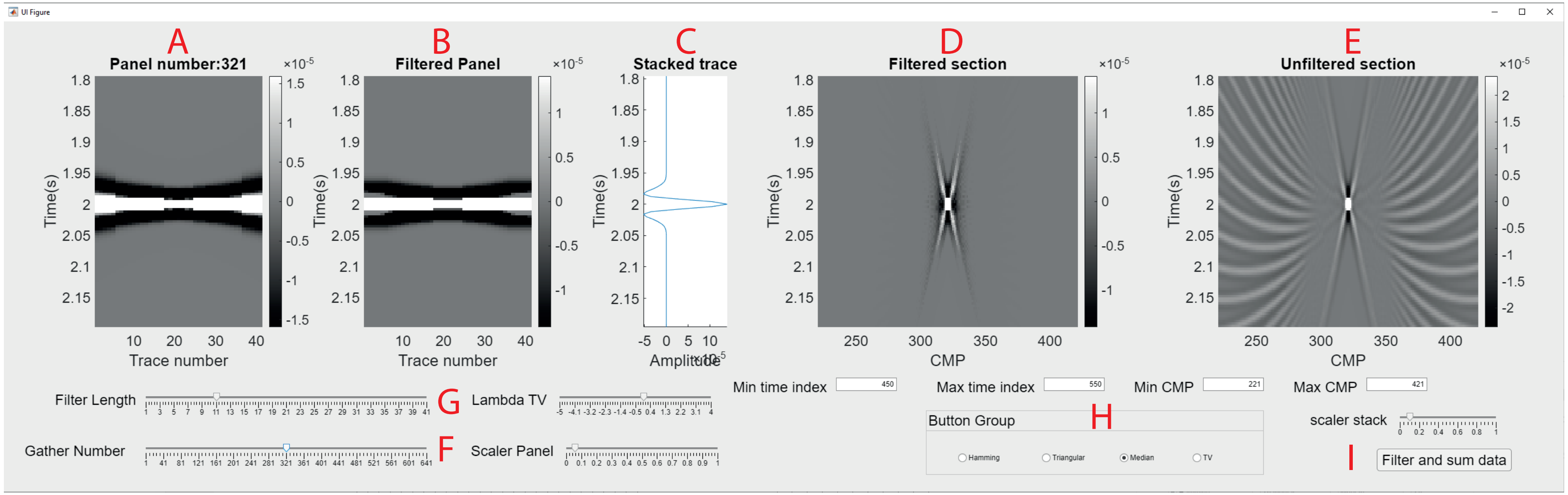

Min time index 450

Max time index 550

Min CMP 221

Max CMP 421

Figure 3.17: *User interface for filtering holistic migration.*

3.5 A note on holistic migration and reflections

As mentioned, diffractions represent the limit of resolution in seismic imaging (cf. Section 2.1). Moreover, diffractions are generally non-directional and global (i.e., scattered waves reach the entire measurement surface). Conversely, reflections are directional and localized. The size of the area that contributes to an event in the imaged section is denoted as the Fresnel aperture (Tabti et al., 2004). Thus, diffractions are defined by a large Fresnel aperture while reflections have a small Fresnel aperture. This implies the importance of employing a large aperture when imaging diffractions, and a smaller aperture when imaging reflections. However, limiting the aperture might lead to an unsatisfactory image section in the case of dipping reflectors, which can be found on larger offsets in the migration operator panels.

The size of the Fresnel aperture of reflected events have implications when imaging using holistic migration. These effect are most easily explained using a data example, for which this study employs the Sigsbee2a model, made public by the Subsalt Multiples Attenuation and Reduction Technology Joint Venture (SMAART JV) between 2001 and 2002. Figure 3.18a shows a conventional migration where reflections have been retained in the dataset, while Figure 3.18b shows the same section formed by using holistic migration (regular subsampling by a factor of eight). By directly comparing the two images, it is evident that much of the character is retained in the holistic migration. However, the signal is once again masked by coherent noise.

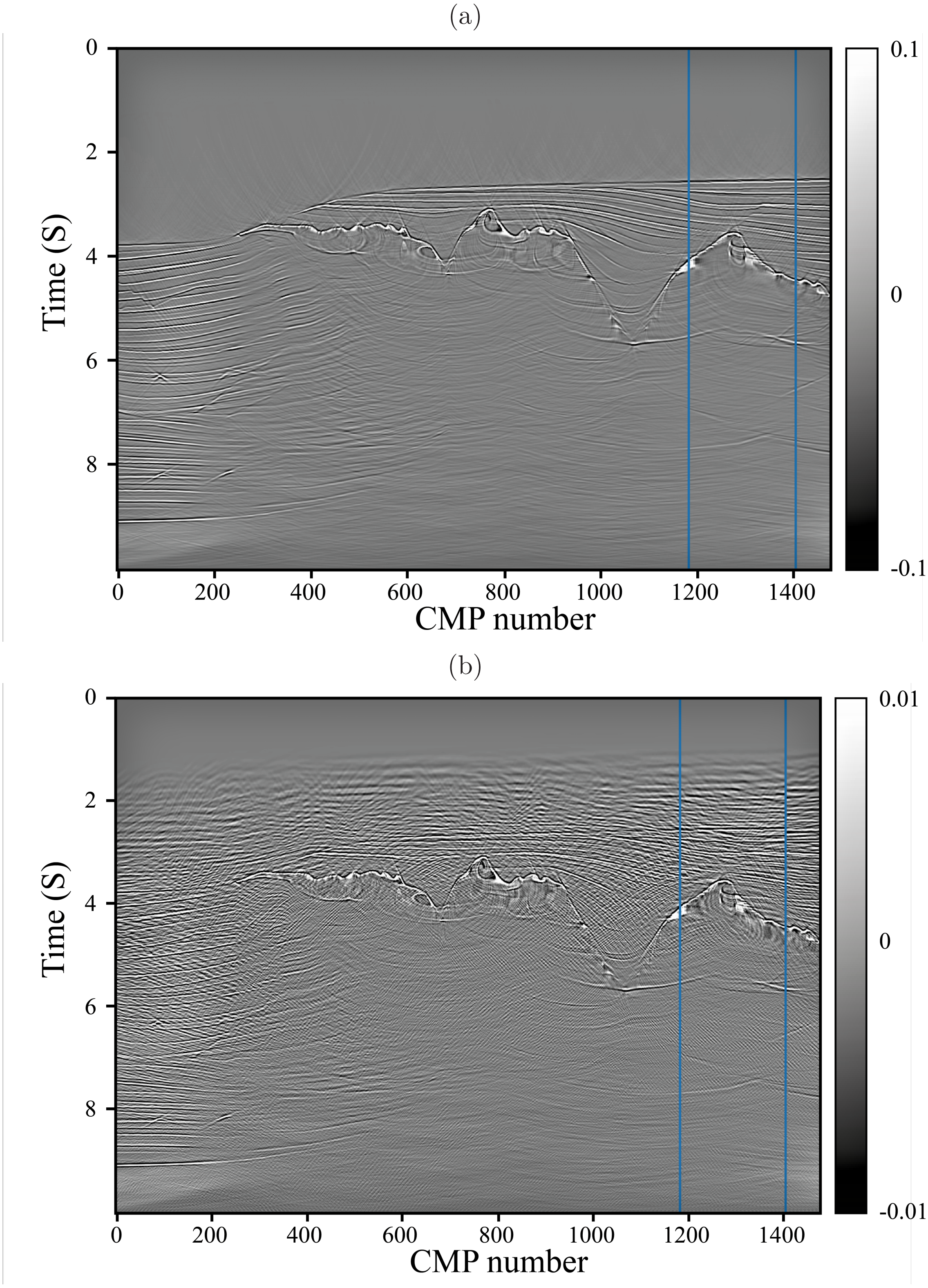

Figure 3.18: *Conventional migration (a) and holistic migration (b) of seismic reflection data. The input data was regularly subsampled by a factor of eight for the holistic migration.*

Initial trials revealed that median filtering of the migration operator panels gave an unsatisfactory image. An alternative approach based on machine learning was therefore tested, where a simple convolutional neural network was trained to remove the coherent noise. The training data is easily obtainable by first forming a conventional migration (Figure 3.18a), which serves as the target, while the subsampled migration operator panels constitute the input data for the network. Figure 3.19 shows a simplified schematic of the network used in this study. The main idea is to partially sum the data (average pooling) over the trace direction as part of the neural network. Ideally, the network should then filter out unwanted coherent noise while preserving the desired signal.

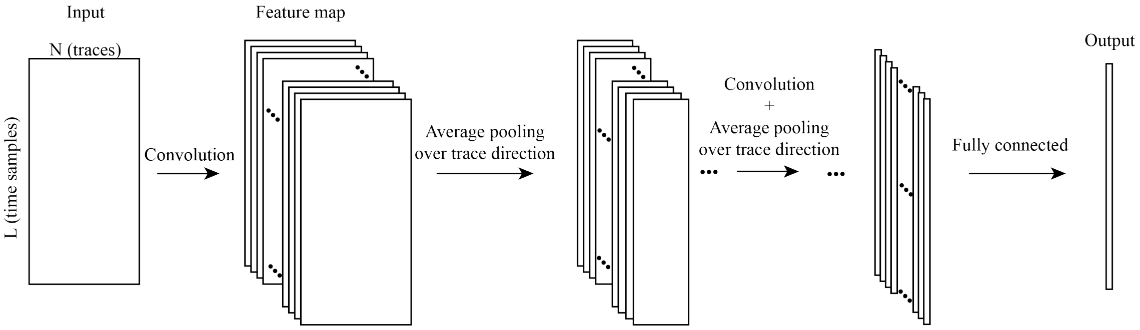

Figure 3.19: *Simplified schematic of the convolutional neural network used in this study.*

The full dataset was divided into training, validation, and test data. The training data constitute the bulk of the data (80%), and is limited by the leftmost blue vertical line. The validation set (15%) is restricted to data that fall between the two blue lines, while the test set (5%) comprise the rest of the dataset. The training set is used to adjust the weights of the neural network during the training stage. As the network tunes the weights towards this dataset, it is therefore necessary to validate that the network is generalizable. During the training stage, the network predictions are therefore continually measured against the validation set. The test set is kept separated during the entire training stage, and is used as a final assessment of whether the network has been able to learn a general function for noise removal. By directly comparing the network prediction with the conventional migration (cf. Figures 3.18a and 3.20a), it is evident that the network is able to remove the undesirable coherent noise for all three subsets of the data. This observation is also reflected in the difference plot between the target data and network prediction (cf. Figure 3.20b).

The results presented in this investigation should be considered as an introductory study only. The Sigsbee2a model contains many strong diffractions, which is ideal for holistic migration. Moreover, the reflected events in the dataset are generally quite flat and have a strong amplitude. It is therefore probable that this machine learning approach will struggle in the presence of high-dipping and weak reflection events. Furthermore, this study treats holistic migration of reflections as a simple denoising problem. However, this approach does not directly confront the problem of missing data. As mentioned, the Fresnel aperture associated with reflected events is much smaller than for diffractions. If the data is too severely undersampled, it is possible that some reflection events will be entirely missing from the migration operator panels. In such a case, the proposed method will not be sufficient for retaining the character of the conventional migration.

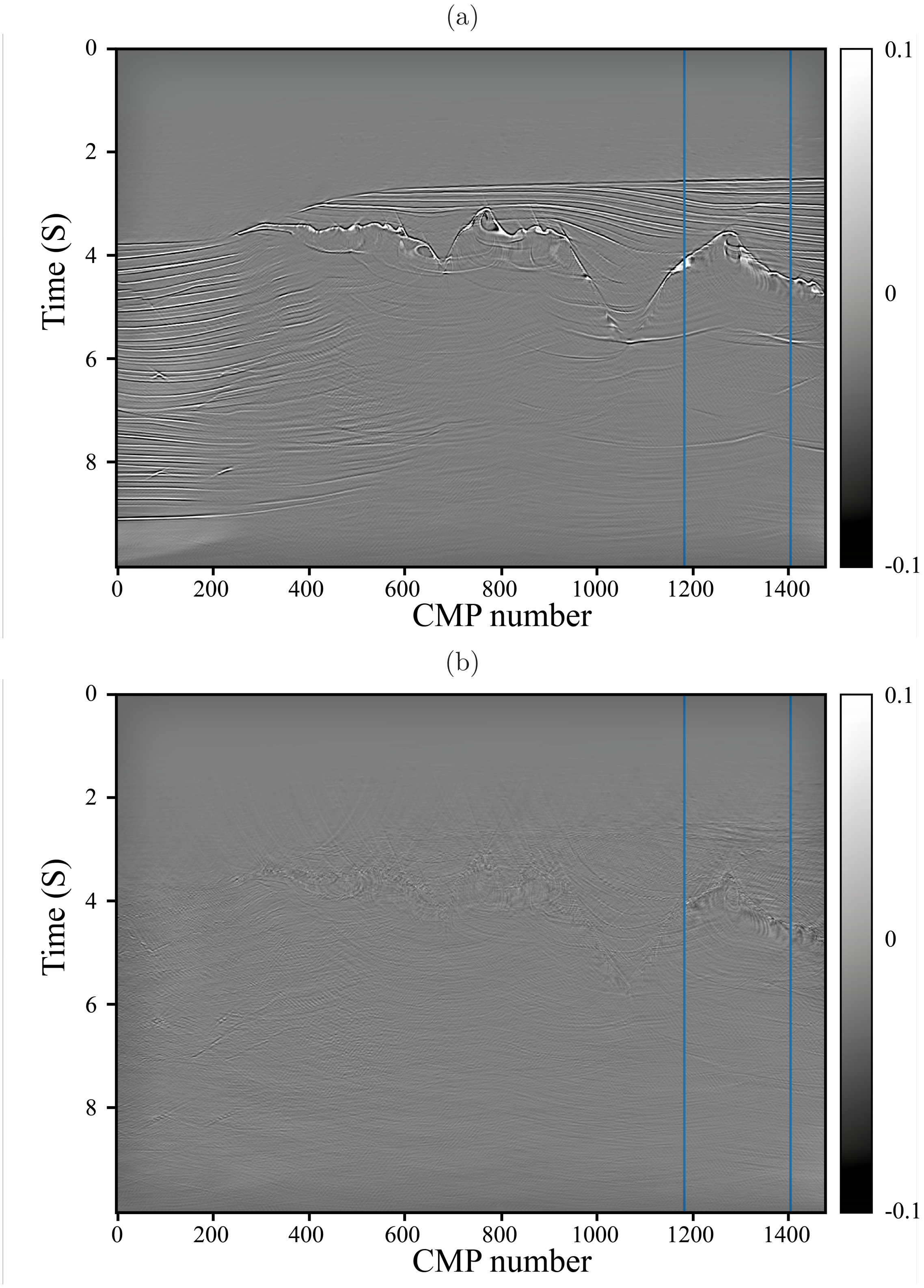

Figure 3.20: *Network prediction (a) and difference plot (target-prediction) (b) of seismic reflection data.*

Chapter 4

Controlled Source Electromagnetics (CSEM)

Around 1950, several independent researchers discussed the idea of determining the electrical resistivity of deep layers in the Earth based on the natural electric field strength measured at the surface (Rikitake, 1948; Tikhonov, 1950). This concept was further refined in a publication by Cagniard (1953), and is currently denoted as magnetotelluric (MT) sounding. It should be noted that all these contributions were carried out independently, and the publishing of Cagniard's seminal paper was delayed by several years due to confidentiality regarding commercial patents related to the MT method.

It would, however, take nearly 20 years before it was proposed to replace the natural source used in MT with a marine active source setup, leading to the concept of CSEM (Bannister, 1968). In his paper, Bannister advocated for the use of a Horizontal Electric Dipole (HED) source due to the increased noise associated with magnetic measurements. This idea was further advanced by Coggon & Morrison (1970), who proposed a high-frequency active source setup to determine the resistivity of the upper layers of the seabed (up to a few tens of meters). In the period to follow, much of the development of active-source EM sounding was led by Charles Cox and colleagues at the Scripps Institution of Oceanography. Young & Cox (1981) described an active source electromagnetic sounding system quite similar to the technology we see today. Moreover, the receiver technology developed at Scripps has continued to be employed for decades. Another important research group was built around professor Martin Sinha at the Cambridge University. They pioneered the work on an improved active source capable of floating in the water column, as opposed to the Scripps source, which was dragged along the seabed (Sinha et al., 1990). This innovation was found to be desirable when working in areas with rough bathymetry, and has been adapted by most subsequent source systems in CSEM.

In CSEM, the transmitted waveform contains a signal of alternating polarity, either with continuous transmission (frequency-domain CSEM) or silent periods without transmission (time-domain CSEM). Both approaches have their own strengths and weaknesses. In case of shallow water, the air-wave mode starts to dominate and its removal is more straightforward when employing time-domain CSEM. However, in case of deep water, frequency-domain CSEM may be the preferred choice. In this thesis work, frequency-domain CSEM is considered. Data was made available due to a collaboration between Electromagnetic Geoservices (EMGS) and the University of Oslo (UiO).

Before the turn of the millennium, there was only moderate interest in CSEM from the petroleum industry. Exxon filed a patent describing a CSEM acquisition system (Srnka, 1986), but significant interest would not come from the industry before the early 2000s (Constable & Srnka, 2007). An internal group at Statoil (now Equinor) had started working on CSEM in the late 1990s, which resulted in a field demonstration outside Angola (Eidesmo et al., 2002; Ellingsrud et al., 2002). At about the same time, Exxon carried out their own field tests (Constable & Srnka, 2007). The promising results of these field tests revitalized interest in CSEM, and several EM companies sprung out of already existing research groups. In Norway, Statoil formed EMGS, the Cambridge team formed Offshore Hydrocarbon Mapping (OHM), and Scripps collaborated with AOA geophysics to establish AGO, which was later acquired by Schlumberger (Cooper & MacGregor, 2020). Another university spinoff (from the University of Edinburgh) was Multi-Transient Electromagnetic (MTEM) Limited, founded in 2004 (Wright et al., 2005). The company was later bought by PGS in 2007.

In this period, CSEM was at the forefront of every oil companies' mind. However, the enthusiasm for this technology has faded since the mid 2000s. Cooper & MacGregor (2020) points at three main reasons for this decline. First, the method was oversold, and did not deliver on its sky-high expectations. Secondly, the leading companies engaged in a patent war, which ultimately hurt both the service companies and customers. The final (and most important) reason was a reluctance to properly integrate CSEM with seismic data. Despite the more recent setback of the CSEM technology, there are clear signs that a more qualified use is developing. A major strength of the method is its reliability when it comes to false negatives (Berre et al., 2020). Thus, properly integrating CSEM data in the decision chain increases the robustness of a proposed drilling campaign. In the years to come, use of the CSEM technique to monitor a CO_2 injection site will most likely also advance (Girard et al., 2011). This is reflected by the setup of the new service company Allton (formerly Petromarker).

In parallel with the development of CSEM from an equipment point of view, major advances were also achieved regarding interpretation and processing of the acquired data. Initially, this analysis was carried out in the data domain by the use of normalized Magnitude Versus Offset (MVO) plots (Ellingsrud et al., 2002; Røsten et al., 2003). However, as computing power developed, a complete inversion in the model domain replaced the simple data domain approach. These days, the inversion techniques can handle complex and anisotropic earth models in 3D (Brown et al., 2012; Wang et al., 2018; Jakobsen & Tveit, 2018)

Although data processing and interpretation in the inverted model domain is far superior to the data domain approach, it does come with a new set of challenges. Modern implementations of CSEM, magnetotellurics (MT), seismic tomography, and computerized tomography (CT) are all based on advanced inversion techniques. Ideally, every inversion result should be accompanied by a proper description of the uncertainty and resolution. Menke (2012) describes how to quantify the resolution of an inversion through the use of two resolution matrices: the *data resolution matrix* and the *model resolution matrix*. The data resolution matrix describes how well the data prediction matches the observed data, while the model resolution matrix describes how well each model parameter in a discrete model is resolved. In this work, we will assess both of these resolution matrices and investigate their applicability within CSEM inversion. However, we will first briefly discuss the basic theory behind CSEM inversion, including the forward modelling engine.

4.1 Practical aspects of forward modelling and inversion

In this section, we will discuss the most important practical aspects of forward modelling and inversion of CSEM data, with special emphasis on how these are implemented in the open-source package MARE2DEM employed in this study (Key, 2016). The basic forward modelling problem was introduced in Section 2.2, but did not include a discussion of how the equation system is solved in practice. The coupled set of equations (cf. Equations 2.25 and 2.26) can be solved by either finite-difference or finite-element techniques. When such discrete solvers are employed, the modelling mesh will be of vital importance for the accuracy of the forward modelling. By introducing a fine grid, the forward modelling will likely be very accurate, but we pay for this accuracy by making the problem computationally demanding. MARE2DEM employs an adaptively refining finite-element forward modelling scheme. Figure 4.1 shows a flow diagram describing the process of forward modelling with adaptively refined elements. As mentioned earlier, the finite-element system is solved independently for each wavenumber k_x. However, it is necessary to solve the system for many different wavenumbers and employ an inverse Fourier transform to obtain the solution for each datapoint. A stable result is achieved by making use of logarithmically spaced k_x values (Key, 2016).

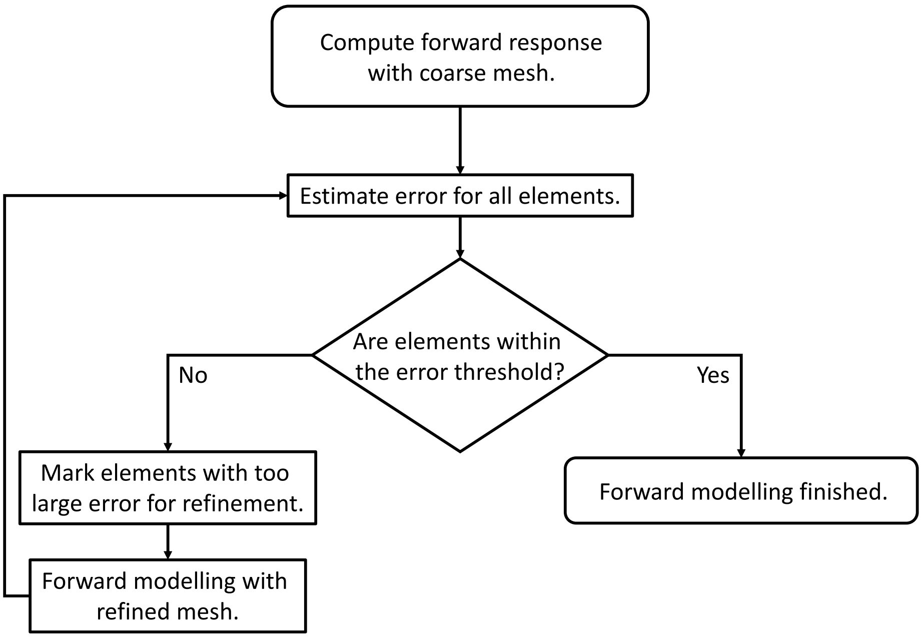

Figure 4.1: *Forward modelling with adaptively refined elements*

When field data are acquired, the earth model extends infinitely, and the measurements approach noise only when the separation between the source and receivers increases (e.g., below the detection threshold of the acquisition equipment). However, when modelling the data, it is necessary to limit the size of a model in order to decrease the computational burden. This can effectively be implemented by employing Perfectly Matched Layers (PML). An ideal PML should absorb all the incoming energy and include as few grid cells as possible for computational efficiency. A powerful implementation involves a coordinate stretch in the PML. Thus, by stretching the coordinates, the PML can be artificially extended while still only including a few grid cells (Li et al., 2018). When implemented correctly, a PML will not reflect any of the incoming energy, and therefore simulate the natural decay of the field strength without any boundary effects. MARE2DEM does not have these absorbing boundary conditions implemented, therefore it is important to employ a large model in order to avoid edge effects.

The starting point for the inversion scheme is a nonlinear problem formulation which is solved iteratively by minimizing a cost-function on the form (Key, 2016; Ren & Kalscheuer, 2020):

$$\phi[\mathbf{m},\alpha] = \left[(\mathbf{d} - F[\mathbf{m}])^{\dagger}\mathbf{W}_d^{\dagger}\mathbf{W}_d(\mathbf{d} - F[\mathbf{m}])\right] + \alpha\mathbf{m}^{\dagger}\mathbf{W}_m^{\dagger}\mathbf{W}_m\mathbf{m} \tag{4.1}$$

where $\mathbf{d}$ of size $i = 1, 2, \ldots N$ is the measured complex field data (i.e., frequency domain), $F[\mathbf{m}]$ is the corresponding modelled response, $\mathbf{W}_d$ is a weighting matrix for the data misfit, α is a Lagrangian weight factor for the regularization term, and $\mathbf{W}_m$ is a regularization matrix. When dealing with complex fields, we need to adopt the Hermitian † (i.e., matrix transpose and complex conjugation) notation for the matrices involved. In MARE2DEM, $\mathbf{W}_d$ is a diagonal matrix composed of the inverse of the standard error δ for each sample and $\mathbf{W}_m$ is a weighting matrix that forces smoothness of the model. The latter is obtained by using a gradient roughness operator. In the case of anisotropic earth models, the roughness is implemented by partitioning the model vector into anisotropic subsets (Key, 2016). Note that in MARE2DEM, the model parameter $\mathbf{m}$ represents the logarithm of resistivity $log(\rho)$ (bounded to a user-defined interval).

In practice and due to the non-linearity of the inverse problem, the forward (modelling) operator F in Equation 4.1 is quasi-linearized by the use of a Taylor series expansion, which can be formally written as:

$$\mathbf{F}[\mathbf{m}_{k+1}] \approx \mathbf{F}[\mathbf{m}_k] + \mathbf{J}(\mathbf{m}_{k+1} - \mathbf{m}_k), \tag{4.2}$$

where J is the model Jacobian matrix with entries $\partial F_i(\mathbf{m_k})/\partial m_j$. This leads to an iterative formulation where the $(k+1)th$ update is given as:

$$\begin{aligned}\phi_{lin}[\mathbf{m}_{k+1}, \alpha] = & \left[(\mathbf{d} - F[\mathbf{m}_k] - \mathbf{J}(\mathbf{m}_{k+1} - \mathbf{m}_k))^\dagger \mathbf{W}_d^\dagger \mathbf{W}_d (\mathbf{d} - F[\mathbf{m}_k] - \mathbf{J}(\mathbf{m}_{k+1} - \mathbf{m}_k))\right] \\ & + \alpha \mathbf{m}_{k+1}^\dagger \mathbf{W}_m^\dagger \mathbf{W}_m \mathbf{m}_{k+1}\end{aligned} \tag{4.3}$$

Finally, after differentiating the cost function (Equation 4.3) with respect to the current model and setting $\partial\phi_{lin}[\mathbf{m}_{k+1}, \alpha]/\partial\mathbf{m}_{k+1} = 0$, a least-squares solution is obtained after rearrangement:

$$\mathbf{m}_{k+1} = \mathbf{J}_w^{-g} \mathbf{W}_d \mathbf{d}_k, \tag{4.4}$$

with $\mathbf{d}_k = [\mathbf{d} - F[\mathbf{m}_k] + \mathbf{J}\mathbf{m}_k]$ being the modified data vector and $\mathbf{J}_w^{-g}$ being the generalized inverse matrix defined as $[\mathbf{J}^\dagger \mathbf{W}_d^\dagger \mathbf{W}_d \mathbf{J} + \alpha \mathbf{W}_m^\dagger \mathbf{W}_m]^{-1} \mathbf{J}^\dagger \mathbf{W}_d^\dagger$. MARE2DEM is based on the Occam approach (Constable et al., 1987) which is a variant of Gauss-Newton minimization. Occam inversion aims to find the smoothest possible model within a given error limit. As seen in Equation 4.4, the model update includes the Lagrangian multiplier α (through $\mathbf{J}_w^{-g}$) to balance data misfit and model roughness. In a conventional inversion, α is a constant user-defined input parameter. MARE2DEM employs a variation of Occam inversion denoted as "fast Occam". Each Occam iteration includes a grid search for the Lagrangian multiplier by calculating the model update and forward response for a range of α values. Thereafter, the model with lowest error (and its corresponding α value) will be used as a starting point for the next iteration. The "fast Occam" approach differs from conventional Occam inversion by terminating the current iteration if a large decrease in misfit is detected (15%) (Key, 2016).

4.2 Resolution matrices

The model resolution matrix describes how well each model parameter is resolved, and was briefly introduced in Section 2.2 with main emphasis on the PSF. Figure 4.2 shows the model resolution matrix calculated for a synthetic model case, with columns representing PSFs and rows representing smoothing kernels. In an ideal case with no regularization ($\alpha = 0$), Equation 2.33 will tend towards the identity matrix ($\mathbf{R_M} = \mathbf{I}$ for a perfectly resolved model). Conversely, it is clear that the model resolution matrix has non-zero values on off-diagonal indexes. Figure 4.2 displays the model resolution matrix for a 2D case with lexicographic ordering of the model space (1D vector). By proper index mapping, the corresponding 2D PSFs and smoothing kernels can be recovered. This allows us to quantify the resolving power of input dataset. For this purpose, we have developed the metric *ratio of resolution*. It is constructed by dividing the diagonal element of $\mathbf{R_M}$ with the sum of all elements falling inside a user-defined ellipsoid. Let V_i denote the ellipsoid centered around model parameter i. The ratio of resolution for model parameter i is then defined as:

$$ratio_{res,i} = \frac{R_{M,ii}}{\sum_{j=1}^{M} |R_{M,ij}| \in V_i}. \tag{4.5}$$

The size of V_i is found by trial and error. This study used an ellipsoid defined by a 150-meter vertical minor axis and a 1000-meter lateral major axis. The model resolution matrix can be constructed irrespective of the data input. Thus, it is possible to combine different subsets of data and quantify their resolving power by evaluating either the associated PSFs or the ratio of resolution.

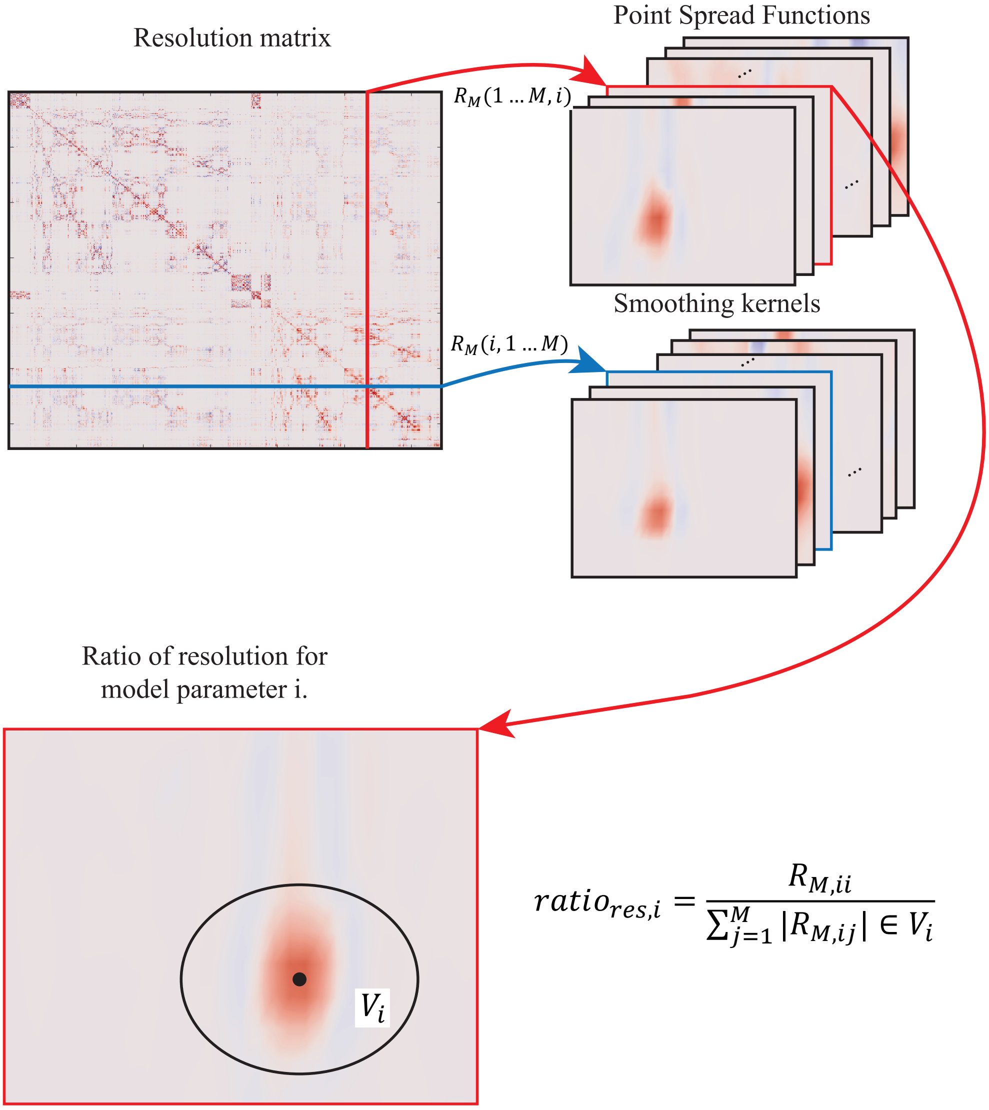

Figure 4.2: *The full model resolution matrix is of size $M \times M$, where M is the length of the model vector. The columns in the resolution matrix define the PSFs, while the rows represent the smoothing kernels. The resolution matrix is difficult to evaluate in its original form. However, by reorganizing the rows or columns via index mapping, it is possible to construct meaningful information in the form of 2D smoothing kernels or PSFs. To summarize the quality of the set of PSFs chosen, we propose the metric ratio of resolution. In the case of model parameter i, it is calculated by dividing the corresponding diagonal element of* $\mathbf{R_M}$ *($R_{M,ii}$) with the sum of the absolute value of all elements that fall inside a user-defined ellipsoid* V_i.

It is possible to construct the ratio of resolution for all combinations of input data. However, this study takes a different approach based on the data resolution matrix, which is constructed as follows. The predicted data for iteration $k + 1$ can be written as:

$$\mathbf{d}_{k+1} = \mathbf{F}[\mathbf{m}_{k+1}], \tag{4.6}$$

which can be combined with Equation 4.2 to give

$$\mathbf{d}_{k+1} \approx \mathbf{F}[\mathbf{m}_k] + \mathbf{J}(\mathbf{m}_{k+1} - \mathbf{m}_k). \tag{4.7}$$

A further combination of Equations 2.28 and 4.7 with the definition $\mathbf{d}_k = (\mathbf{d} - \mathbf{F}[\mathbf{m}_k] + \mathbf{J}\mathbf{m}_k)$ leads to:

$$\mathbf{d}_{k+1} \approx \mathbf{R_D}\mathbf{d} + (\mathbf{I} - \mathbf{R_D})(\mathbf{F}[\mathbf{m}_k] - \mathbf{J}\mathbf{m}_k), \tag{4.8}$$

where $\mathbf{R_D}$ is denoted as the data resolution matrix and given explicitly as:

$$\mathbf{R_D} = \Re\left[\mathbf{J}\left[\mathbf{J}^\dagger\mathbf{W}_d^\dagger\mathbf{W}_d\mathbf{J} + \alpha\mathbf{W}_m^\dagger\mathbf{W}_m\right]^{-1}\mathbf{J}^\dagger\mathbf{W}_d^\dagger\mathbf{W}_d\right]. \tag{4.9}$$

The diagonal of $\mathbf{R_D}$ is often called *data importances* (Maurer et al., 2000; Ren & Kalscheuer, 2020), and describes how important a data point is in its own prediction.

4.3 MARE2DEM user interfaces and extensions

In this section, the user interfaces (UI) of the MARE2DEM software will be briefly introduced, followed by a more in-depth description of a self-developed UI for sensitivity analysis and data reduction. The MARE2DEM package is an adaptive forward modelling and inversion code for CSEM and MT data. Table 4.1 lists a summary of the features included in the MARE2DEM package. The forward modelling and inversion code is programmed in Fortran and C, and can run on Unix operating systems. The code is fully paralellized, and can run on small laptops up to large clusters. The inversion code is seamlessly connected with several graphical user interfaces built in MATLAB. Perhaps the most important of these is the model builder (Mamba2D), in which the user can construct complex synthetic models and set up the inversion problem. The MATLAB code also includes UIs to display the resisitivity models (plotMARE2DEM) and data responses (plotMARE2DEM_CSEM and plotMARE2DEM_MT). Moreover, the package also provides the user with a simple sensitivity measure based on normalized sensitivity. This measure can be explicitly written as:

$$s_j = \frac{1}{A_j}\sum_i^n \left| W_{d,ii}\frac{\partial F_i(\mathbf{m_k})}{\partial m_j} \right|, \tag{4.10}$$

where $W_{d,ii}$ is the inverse of the standard error of data point i and A_j is the area of data element j. Put in a simple way, the normalized sensitivity is computed by summing the Jacobian matrix columnwise weighted by the data uncertainty.

Table 4.1: *Summary of features included in MARE2DEM.*

Forward modelling and inversion	**Model builder and data display**
Unix-based with MPI, Fortran and C compilers	MATLAB-based
Supports anisotropic models (VTI, HTI and triaxial)	Model builder (Mamba2D)
Supports a range of data inputs for both CSEM and MT data.	Displays synthetic and inverted resistivity models (plotMARE2DEM)
	Displays normalized sensitivity (plotMARE2DEM)
	Displays CSEM field data and inverted response
	Displays MT field data and inverted response

4.3.1 User interface

This study proposes a comprehensive workflow based on the resolution matrix and derived quantities to analyze the resolving power and robustness of electromagnetic data (marine CSEM). In order to efficiently employ these quantities, a UI has been developed which can be seen as an extension to the MARE2DEM software. Figure 4.3 shows a snapshot of this UI, which is fully compatible with MARE2DEM file formats, and requires a data file and the corresponding Jacobian calculations in order to function. Additionally, the user can optionally input a polygon file for plotting purposes (denoted by A in Figure 4.3). After the required files are loaded, the plot is automatically updated (C), and the user has the option of plotting both vertical and horizontal resistivity (B, top). Moreover, the user has full control over a range of plotting options (B, bottom).

The next step of the sensitivity analysis includes the calculation of resolution matrices. Initially, the user has full control over which data points are included in this calculation. For example, it is possible to remove selected receivers, transmitters, or frequencies from the calculation (D). After the optional initial subsampling, the resolution matrices are calculated (E). Subsequently, the user can plot either the full resolution matrices or their respective diagonal elements as separate plots. However, as previously mentioned, these quantities are difficult to analyze in their original forms. Thus, the UI provides several plotting options that aid the user in quantifying the resolving power of the selected dataset (F). For the model resolution matrix, this includes the *ratio of resolution* (cf. Figure 4.2 and Equation 4.5), radius of resolution (Friedel, 2003) and a distance plot. The last item is a simple measure of how far away the maximum value of a single PSF is from the origin.

The different data points in the data set are quantified through data importance plots. In this regard, the UI provides the user with two different options. In both cases, the data importance is plotted as a function of frequency and offset. However, the difference lies in the calculation of data importances. One implementation plots the data importances calculated from the full data resolution matrix, while the other calculates the data importance on a frequency-per-frequency and receiver-per-receiver basis (denoted as individual calculation). In this study, the individual calculation was used for data selection. After careful data analysis, the subsampling can be carried out employing all the above mentioned plots (G). The UI allows the user to subsample based on a percentile value of the full dataset, remove receivers entirely, impose offset limits, or remove certain frequencies. After the downsampling has been carried out, the UI will automatically calculate the model resolution matrix of the downsampled dataset, which is used to investigate the resolving power of this dataset.

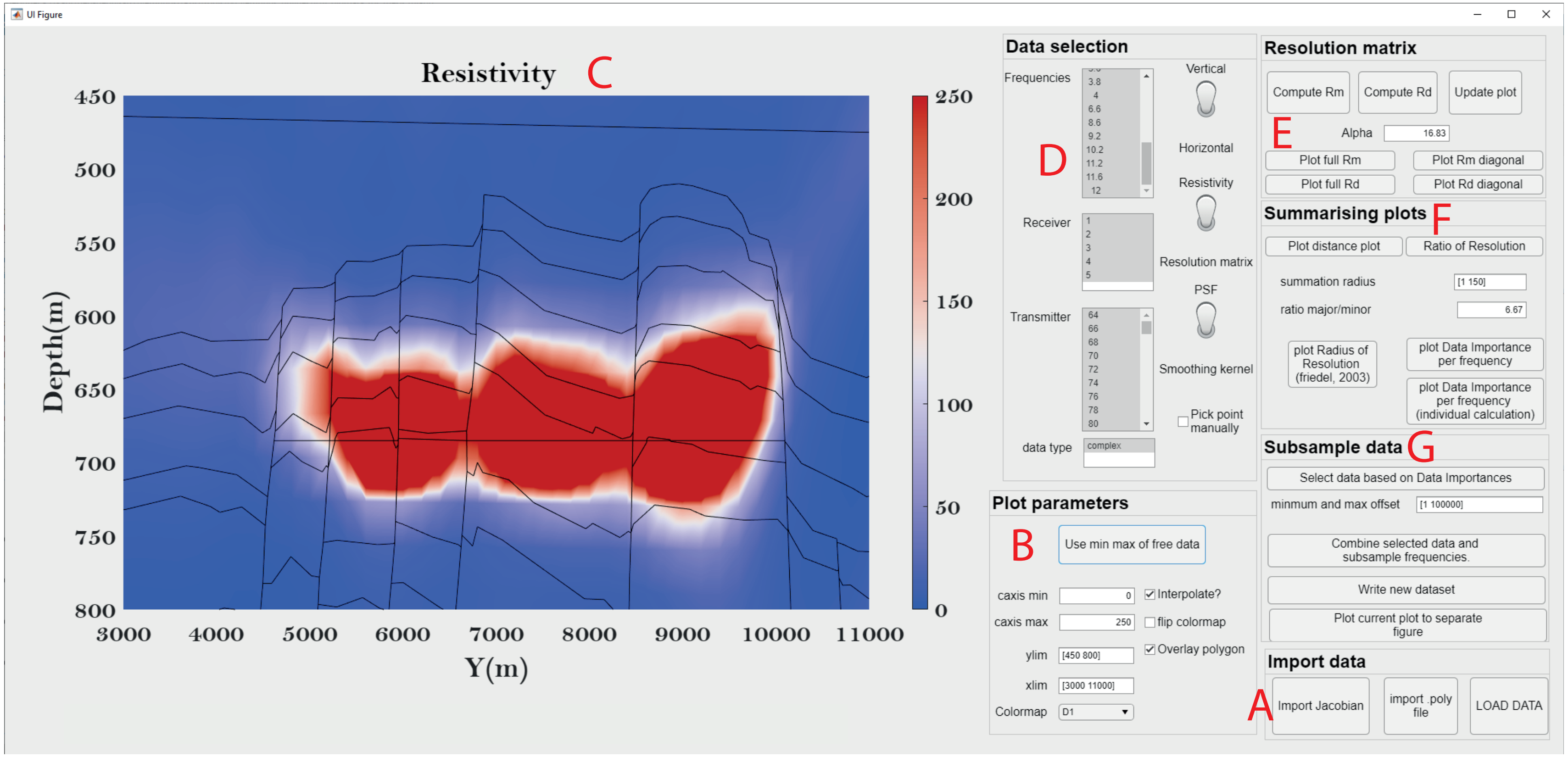

data type: complex

☐ Pick point manually

Alpha: 16.83

summation radius: [1 150]

ratio major/minor: 6.67

minmum and max offset: [1 100000]

caxis min: 0

caxis max: 250

☑ Interpolate?

☐ flip colormap

☑ Overlay polygon

ylim: [450 800]

xlim: [3000 11000]

Colormap: D1

Figure 4.3: *UI with resistivity*

The user can easily choose what parameters to display through the switches marked with A, B, and C in Figure 4.4. As already mentioned, the UI allows for plotting either vertical or horizontal resistivity (A). However, another important feature of the UI is the interactive access to PSFs and smoothing kernels (Figure 4.4). By flipping switch (B) from resistivity to resolution matrix, the UI automatically plots either PSFs or smoothing kernels (controlled through switch C). Moreover, the user can enable interactive access to PSFs (or smoothing kernels) by clicking a check box (D). After choosing a model parameter of interest, the UI allows for flexibility with regard to displaying the PSF or smoothing kernel from either the vertical or horizontal resolution matrix.

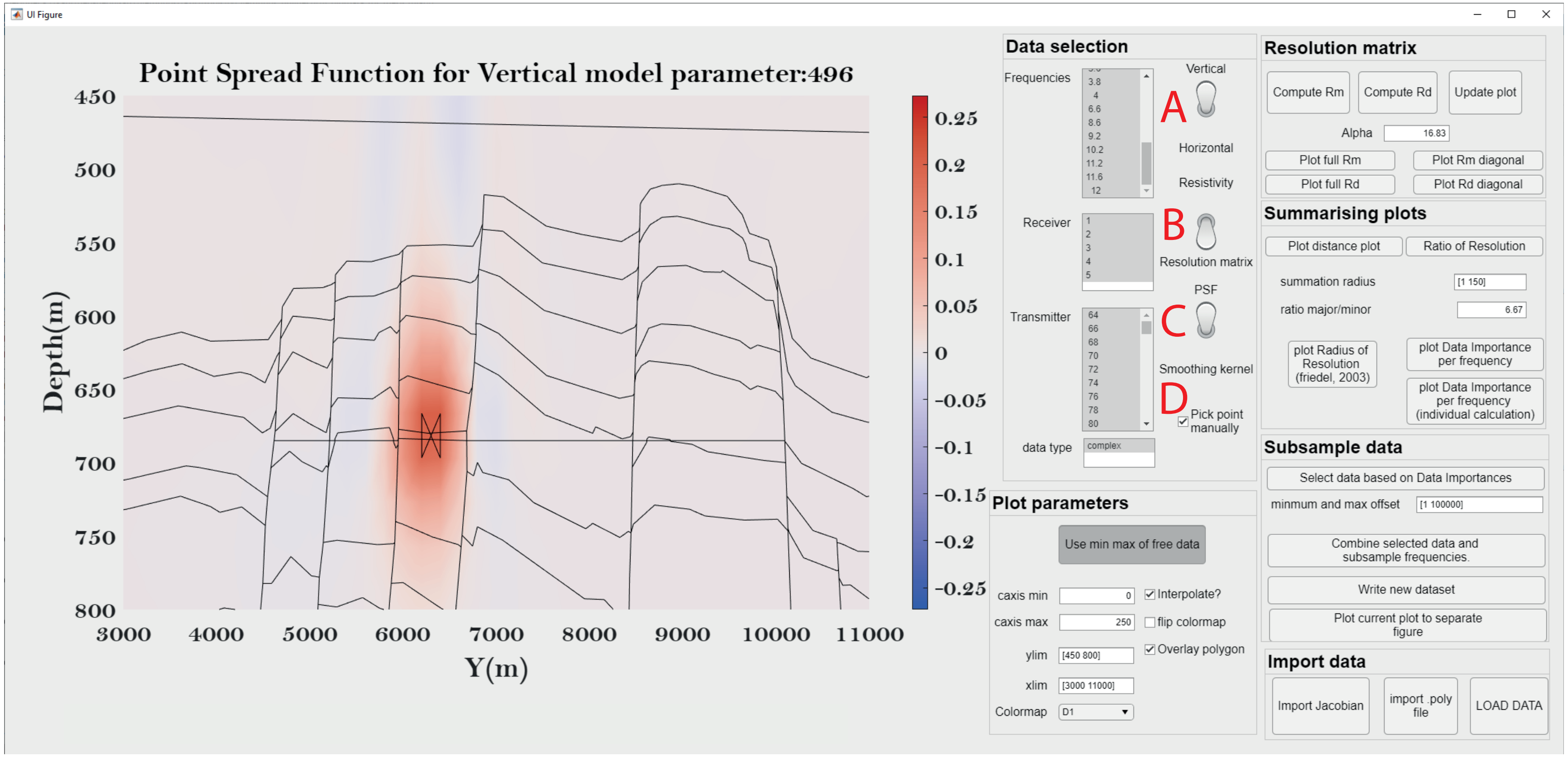

☑ Pick point manually

data type: complex

caxis min: 0

caxis max: 250

☑ Interpolate?

☐ flip colormap

☑ Overlay polygon

ylim: [450 800]

xlim: [3000 11000]

Colormap: D1

Alpha: 16.83

summation radius: [1 150]

ratio major/minor: 6.67

minmum and max offset: [1 100000]

Figure 4.4: *UI with PSF.*

4.4 PSF inversion

Due to the diffusive character of the EM field, only very low frequencies are used, leading to inversion results with rather low resolution. The blur associated with a CSEM inversion is however characterized by the PSFs. By analogy with work carried out earlier within seismic data imaging and inversion (Hu et al., 2001; Sjoeberg et al., 2003; Yu et al., 2006; Takahata et al., 2013; Yang et al., 2022) and astrophysics (Xu et al., 2020), we propose to employ the PSFs extracted from a regularized Gauss-Newton inversion of marine CSEM data to further deblur the inversion result in a post-processing step. Consider now a blur model on the form:

$$\mathbf{A}\mathbf{m} = \mathbf{b} + \mathbf{n}, \tag{4.11}$$

where we use the notation $\mathbf{A}$ to represent the resolution matrix corresponding to a lexicographic ordering of a 2D image (or model), and $\mathbf{n}$ represents additive noise. Equation 4.11 describes a general relationship between the the true model $\mathbf{m}$ and its blurred counterpart $\mathbf{b}$ (i.e., output from CSEM inversion). The blurring matrix $\mathbf{A}$ can take different forms depending on which boundary conditions are imposed and if we treat the problem as space-invariant (one PSF) or space-varying (multiple PSFs). In the following, we will describe how to construct $\mathbf{A}$ for these cases. However, as the space-invariant case represents the least complex of these, it serves as a good starting point for further discussion.

4.4.1 The blurring matrix

The construction of the blurring matrix is most easily explained by employing a simple 2D example. Consider a 3×3 blurred model as seen on the left hand side in Figure 4.5. The 2D matrix can be transformed into a 1D vector employing lexicographic ordering (right hand side of Figure 4.5). The matrix product $\mathbf{Am}$ represents a 2D convolution of a PSF and the true (deblurred) model.

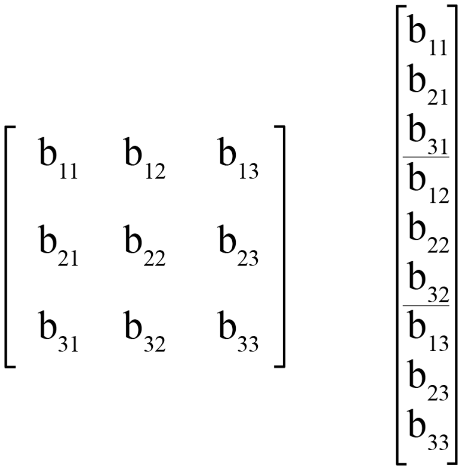

Figure 4.5: *Blurred model (left) and the corresponding model with lexicographic ordering (right).*

Figure 4.6 shows a schematic representation of this two-dimensional convolution operation. The elements in the blurred model are the sum of the elementwise product of the PSF and the true (deblurred) model. However, note how the PSF is rotated 180 degrees before multiplication due to the operation of convolution. For a central element (b_{22} in Figure 4.6), the blurred matrix element is obtained by direct multiplication and summation. However, it is necessary to impose boundary conditions when moving from the central element. In this study, we have employed zero boundary conditions, which can be seen in the calculation of the blurred matrix element b_{11}. Other popular boundary conditions include periodic and reflexive boundary conditions (Hansen et al., 2006).

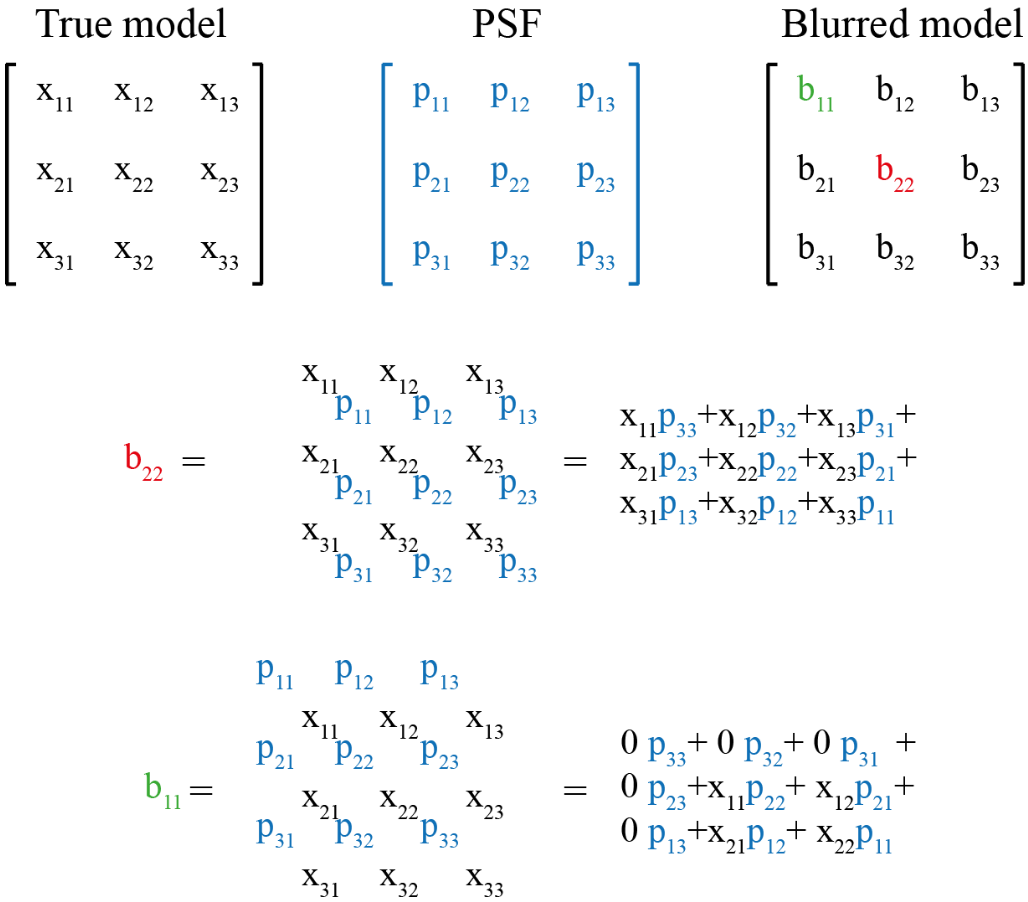

Figure 4.6: *Schematic representation of 2D convolution.*

Figure 4.6 shows how the two-dimensional convolution can be performed employing 2D matrices. However, employing lexicographic ordering entails performing the same operation using only matrix multiplications. For 2D problems with lexicographic ordering, **A** can take different forms depending on which boundary conditions are introduced. As mentioned, we have used zero boundary conditions in this study. Thus, **A** turns into a Block Toeplitz matrix with Toeplitz Blocks (BTTB), which is characterized by constant values along the diagonals (with the exception of some zero elements corresponding to the boundary condition) (Figure 4.7). Moreover, the matrix is built up by diagonally constant bands of Toeplitz blocks (Hansen et al., 2006). In practice, the BTTB matrix is most easily constructed by first forming the smaller Toeplitz blocks, followed by inserting these into the larger BTTB matrix. The reader is referred to paper III for a general description of the BTTB matrix structure.

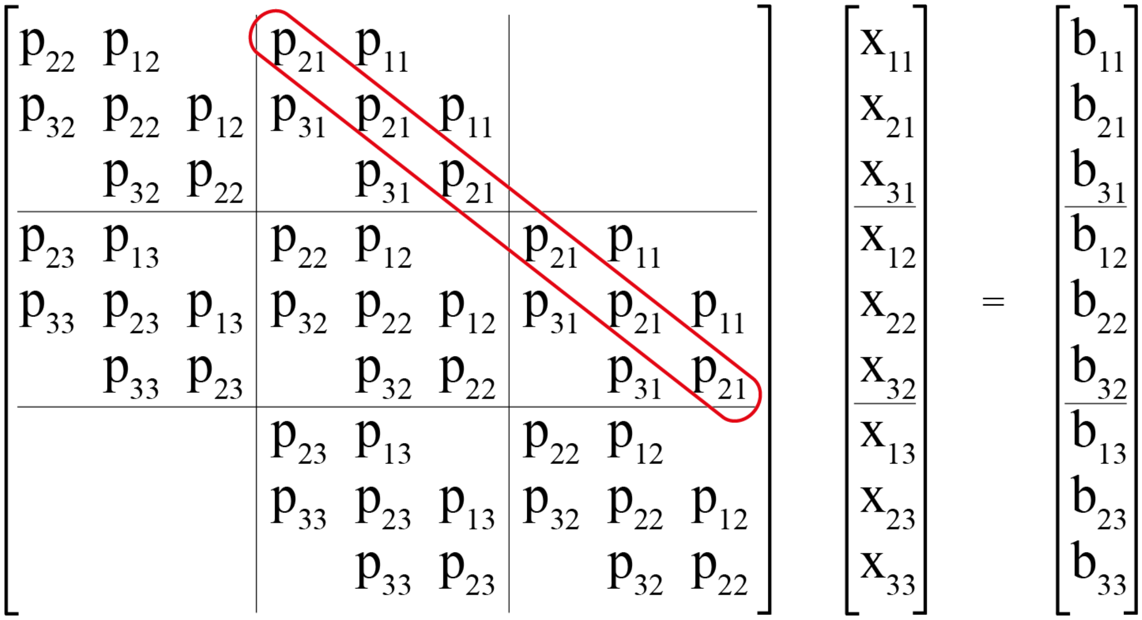

$$\left[\begin{array}{ccc|ccc|ccc}
p_{22} & p_{12} & & p_{21} & p_{11} & & & & \\
p_{32} & p_{22} & p_{12} & p_{31} & p_{21} & p_{11} & & & \\
 & p_{32} & p_{22} & & p_{31} & p_{21} & & & \\
\hline
p_{23} & p_{13} & & p_{22} & p_{12} & & p_{21} & p_{11} & \\
p_{33} & p_{23} & p_{13} & p_{32} & p_{22} & p_{12} & p_{31} & p_{21} & p_{11} \\
 & p_{33} & p_{23} & & p_{32} & p_{22} & & p_{31} & p_{21} \\
\hline
 & & & p_{23} & p_{13} & & p_{22} & p_{12} & \\
 & & & p_{33} & p_{23} & p_{13} & p_{32} & p_{22} & p_{12} \\
 & & & & p_{33} & p_{23} & & p_{32} & p_{22}
\end{array}\right]
\left[\begin{array}{c}
x_{11} \\ x_{21} \\ x_{31} \\ \hline x_{12} \\ x_{22} \\ x_{32} \\ \hline x_{13} \\ x_{23} \\ x_{33}
\end{array}\right]
=
\left[\begin{array}{c}
b_{11} \\ b_{21} \\ b_{31} \\ \hline b_{12} \\ b_{22} \\ b_{32} \\ \hline b_{13} \\ b_{23} \\ b_{33}
\end{array}\right]$$

Figure 4.7: *Schematic representation of the matrix system (cf. Equation 4.11) in the case of lexicographic ordering.*

4.4.2 Generalization to space-variant PSF (image segmentation)

We are now ready to discuss the more general case characterized by space-variant PSFs. A pragmatic approach would be to subdivide the model space into space-invariant regions and perform deblurring separately for each such region. This implies that each region is assigned a deblur matrix of the form given by Figure 4.7, but with its own representative PSF. The final image is then constructed by combining the space-invariant regions after deblurring (and possibly with some smoothing applied to avoid edge effects). A more attractive approach, however, is to construct a space-variant **A** matrix (Nagy & O'leary, 1997). Let Figure 4.8 (left part) represent an idealized case where the model space is subdivided in two regions, each of them characterized by distinct and different PSFs. In order to minimize edge effects, a transition zone has also been introduced, which defines a gradual transition between the two PSFs. Figure 4.8 (right part) shows the corresponding lexicographical ordering of the model parameters including the transition zone (by analogy with Figure 4.5).

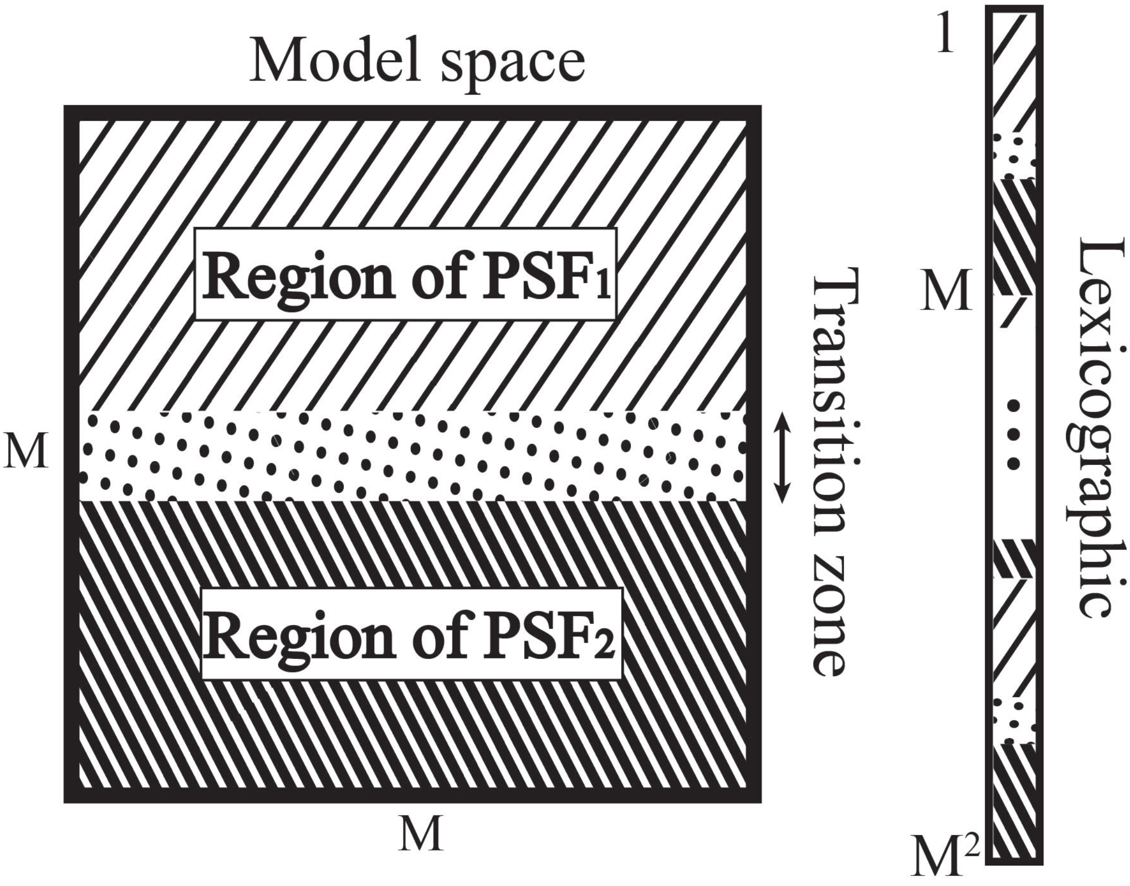

Figure 4.8: *Generalization to space-variant PSF.*

Before constructing the space-variant blur matrix $\mathbf{A}$, we need to define a corresponding space-invariant blur matrix for each subregion (same form as in Equation 9 in Paper III). In the idealized case shown in Figure 4.8, two blur matrices, $\mathbf{A_1}$ and $\mathbf{A_2}$ need therefore to be constructed. In this demonstration example, we have defined the two PSFs as simple 2D Gaussian functions with a different degree of blurring. More specifically, we chose the PSF of region 1 to introduce less blurring than the corresponding PSF of region 2. This implies that the blur matrix $\mathbf{A_1}$ has a more narrow band of values concentrated along its diagonal compared to the blur matrix $\mathbf{A_2}$ (cf. upper row in Figure 4.9).

The next step is to calculate a weighting matrix for each of the two regions in Figure 4.8 (respectively $\mathbf{D_1}$ and $\mathbf{D_2}$). In order to avoid edge effects, we want the PSF to vary smoothly between different subregions. This is obtained by applying a linear tapering between neighboring subregions. In such a transition zone, the effective PSF is constructed as the linear combination between the two neighbouring PSFs. The two weighting matrices for the idealized case in Figure 4.8 are shown in the middle row in Figure 4.9. A zoomed version of a section of the weighting matrix $\mathbf{D_2}$ is also included to better visualize the smooth transition between the two subregions (i.e., no sharp edges). The final blur matrix $\mathbf{A}$ can now be constructed as the sum of the Hadamard product of the two space-invariant matrices and the associated weighting matrices:

$$\mathbf{A} = \mathbf{A_1} \odot \mathbf{D_1} + \mathbf{A_2} \odot \mathbf{D_2}, \tag{4.12}$$

where the effective blur matrix **A** is shown in the bottom row in Figure 4.9. A zoomed version of a section of this matrix is also shown to better illustrate the effect of the smooth transition zone introduced between the two subregions in Figure 4.8.

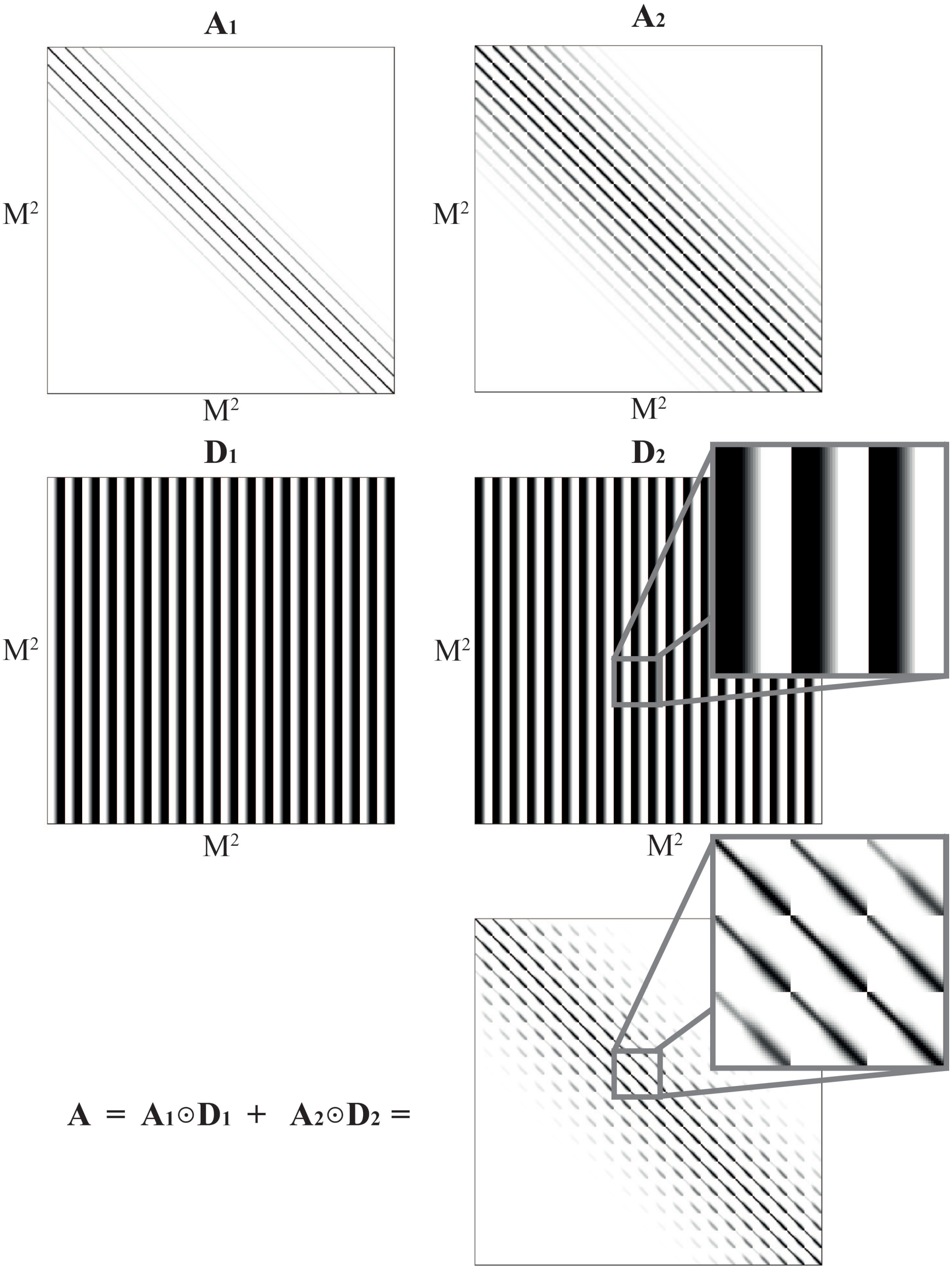

Figure 4.9: *Generalization to space-variant PSF.*

4.4.3 Deblurring algorithm (NN-FCGLS)

We are now ready to discuss how to deblur the output from the CSEM inversion. This step represents a new inversion problem to be solved, namely the one with a forward model as given by Equation 4.11. Several solution alternatives exist; in this study, we use the nonnegative flexible conjugate gradient least-squares (NN-FCGLS) algorithm (Gazzola & Wiaux, 2017) which is implemented as an inner-outer scheme. The model update in the inner iteration can be written in the form

$$\mathbf{m}_{k+1} = \mathbf{m}_k \alpha_k + \mathbf{p}_k, \tag{4.13}$$

where α_k is a *bounded* step size and $\mathbf{p}_k$ is a direction vector. In order to fulfill the condition of nonnegativity in the solution space, the main idea is to reduce the step size α_k so that $\mathbf{m}_{k+1} \geq 0$ if $\mathbf{m}_k > 0$. In NN-FCGLS, this is accomplished by the use of a bounded step size calculated from using the scheme:

$$\bar{\alpha_k} = \begin{cases} \alpha_k & \text{if } \mathbf{p}_k \geq 0 \\ min\left\{\alpha_k, min - (\mathbf{m_k})_j/(\mathbf{p}_k)_j\right\}, \quad j \in K & \text{if } \mathbf{p}_k < 0 \end{cases} \tag{4.14}$$

where K is a set of indices j such that $(\mathbf{p}_k)_j < 0$ and the direction $\mathbf{p}_k$ is obtained by a linear combination of at most κ_k previously computed $\mathbf{p}_j$ with j varying in $\{max\{0, k - \kappa_k\}, ..., k-1\}$. If a maximum number of iterations k_{max} is assigned for the inner cycle, the choice $\kappa_k = k_{max}$ corresponds to a full recursion, while a lower κ_k corresponds to a truncated recursion and with $\kappa_k = 1$, only the last computed vector $\mathbf{p}_{k+1}$ is used. The outer cycle relies on suitable restarts in order to avoid stagnation. For further details about the algorithm, the reader is referred to (Gazzola & Wiaux, 2017). In our study, we employed a code taken from the MATLAB library IR-tools (Gazzola et al., 2019).

Since the NN-FCGLS method enforces a nonnegativity constraint at each iteration, we believe that this algorithm will produce a more accurate approximate solution in our case where the output from the CSEM inversion is truly nonnegative (i.e., $log(\rho)$) where the resistivity ρ is bounded by $\rho \geq 1\Omega$-m). The proposed approach of deblurring is based on PSFs extracted from the resolution matrix associated with a linearized approximation of the original non-linear problem. Thus, this procedure does not represent an exact solution to the blur problem and in general results obtained should always be treated with caution.

4.4.4 User Interface

As the inversion can be sensitive to input parameters (e.g., choice of PSFs and size of transition zones), it was crucial to develop an interactive UI to assist in the selection of optimized parameters. Figures 4.10 and 4.11 display the UI (left and right parts respectively), which has features that can be divided into several groups.

When using the UI, the first step involves loading the data. However, before loading the relevant files (e.g., PSFs and blurred model), it is necessary to determine if the dataset has to be interpolated down to a regular grid, or if it can be used in its original form (A, Figure 4.10). This step also includes the crucial process of tapering the PSFs. Note that in practical application, each PSF will be delimited to a smaller area with tapering and with a normalization that ensures that the sum of its values inside the tapered area *add to one*. Subsequent to determining the data load parameters, the PSFs and blurred model are loaded into memory. The UI also optionally allows the user to load a polygon file in MARE2DEM's internal format (B, Figure 4.10).

When the files are loaded, the user can start selecting an array of PSFs. This process is done interactively by clicking on the display shown in Figure 4.11 (D). In general, and from personal experience, PSFs located (well) outside the target area should not be employed. Relevant PSFs are those near and inside the target area or structure. These observations stress the important role our interactive UI plays in the quality control of the selected parameters. After selecting a satisfactory PSF, it can be added to a list of PSFs via a button click (C, Figure 4.11). After the PSF has been added to the list, it will automatically appear on the data display shown in Figure 4.10 as a green dot referring to its corresponding model parameter position. The UI is also implemented with the option of employing an ideal PSF. Such a PSF consists of a centered spike, and can be used in the perimeter of the inversion problem to ensure stability.

Finally, the user provides the boundaries between the selected PSFs, along with a boundary size over which the PSFs are interpolated. This set of parametric choices is then used to construct the space-variant **A**-matrix as described in Section 4.4.2 (E, Figure 4.11). The blur matrix **A** is stored in the memory of the UI, allowing the user to efficiently try out different sets of inversion parameters.

In this PhD study, three deblurring options were implemented: Blind deconvolution, Tikhonov regularized least squares inversion, and NN-FCGLS (F, Figure 4.11). However, NN-FCGLS was found to perform best after extensive testing. Moreover, Blind deconvolution was only used as a benchmark. After the user has selected inversion parameters, the inversion can be carried out with a button click (F, Figure 4.10). At each iteration, the inversion result is stored in memory (and on disk), and can be easily accessed through the slider shown in Figure 4.10 (G). If we need to access previous inversions, these can easily be loaded back into memory (B, Figure 4.10). The user is provided with the option of changing a range of plotting parameters on the fly (H, Figure 4.10), and the most important results can be saved to disk by way of a simple button click (I, Figure 4.11).

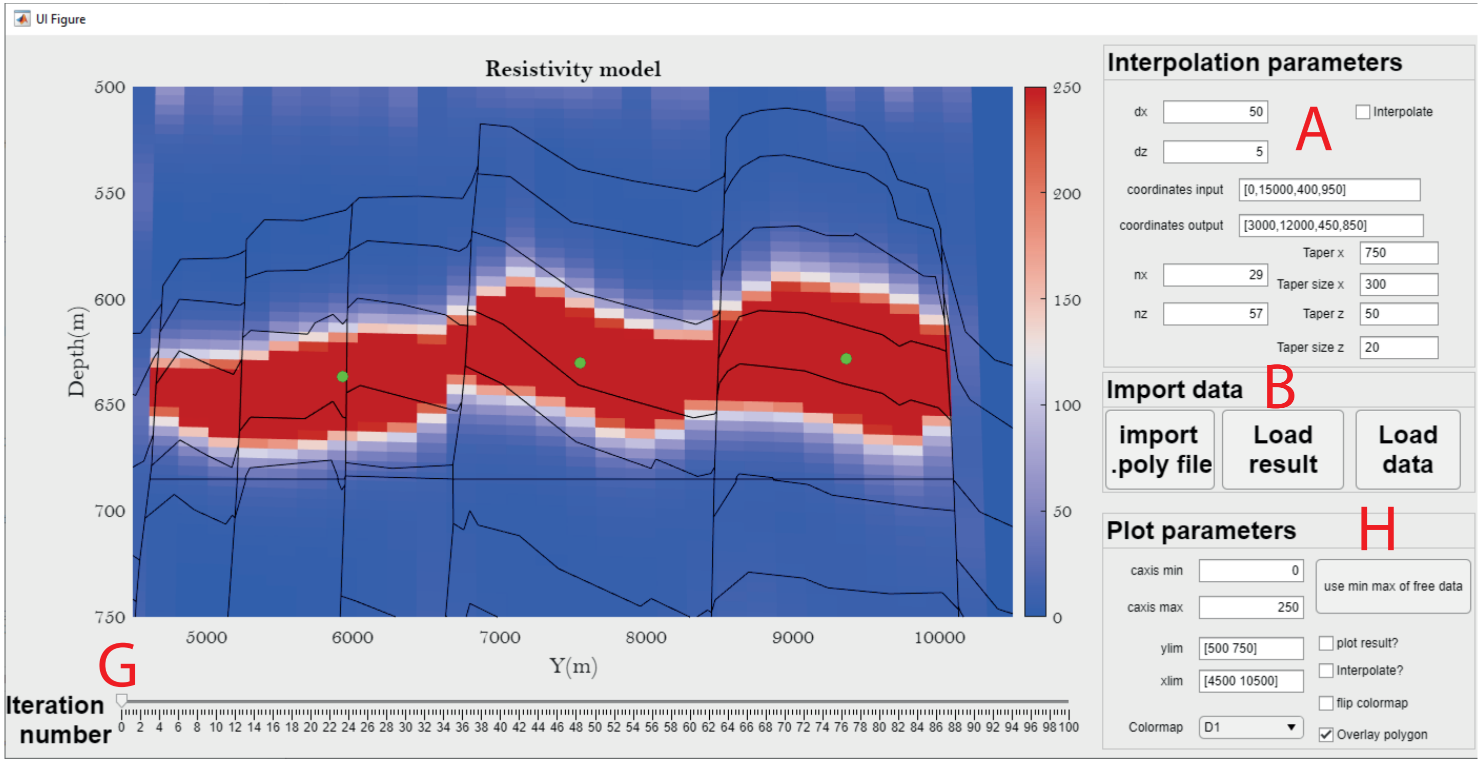

dx 50

dz 5

☐ Interpolate

coordinates input [0,15000,400,950]

coordinates output [3000,12000,450,850]

Taper x 750

nx 29

Taper size x 300

nz 57

Taper z 50

Taper size z 20

caxis min 0

caxis max 250

ylim [500 750]

xlim [4500 10500]

Colormap D1

☐ plot result?

☐ Interpolate?

☐ flip colormap

☑ Overlay polygon

Figure 4.10: *Left part of UI.*

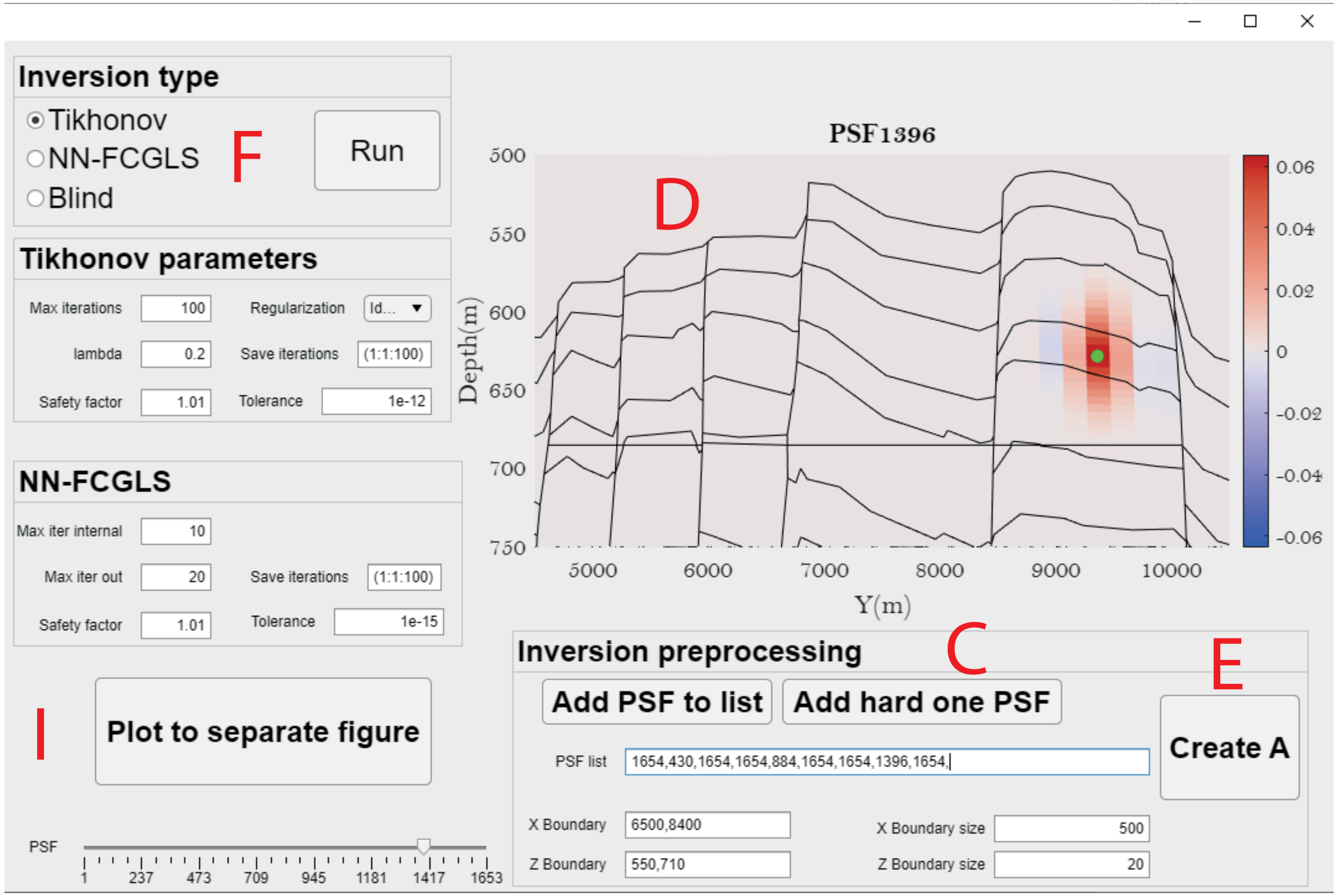

Inversion type

● Tikhonov
○ NN-FCGLS
○ Blind

Tikhonov parameters

Max iterations: 100
lambda: 0.2
Safety factor: 1.01
Regularization: Id...
Save iterations: (1:1:100)
Tolerance: 1e-12

NN-FCGLS

Max iter internal: 10
Max iter out: 20
Safety factor: 1.01
Save iterations: (1:1:100)
Tolerance: 1e-15

Inversion preprocessing

PSF list: 1654,430,1654,1654,884,1654,1654,1396,1654,
X Boundary: 6500,8400
Z Boundary: 550,710
X Boundary size: 500
Z Boundary size: 20

Figure 4.11: *Right part of UI.*

Chapter 5

Contributions of this thesis

5.1 Paper I:

Revisiting holistic migration

Vemund S. Thorkildsen, Leiv-J. Gelius and Enders A. Robinson.

The Leading Edge, Volume 40, issue 10 (2021): 768-777.

Motivation and objectives

Although more than 25 years have passed since the introduction of holistic migration in the seismic literature, earlier studies have not gained much interest. One of the reasons for this might be attributed to the lack of proper field data examples. Moreover, preceding studies recognized the difference in reflective and diffractive contributions to seismic imaging (Neidell, 1997; Robinson, 1998, 2018), but relied on the validity of Huygens' principle to recover a well-sampled image. Furthermore, the earlier studies did not properly consider the consequences of undersampling (i.e., noise) or which measures should be taken to remove such artifacts.

The above-mentioned publications challenge the common idea that the conventional Nyquist-Shannon sampling criterion determines image resolution. The idea of signal recovery beyond Nyquist has also been discussed by Wisecup (1998) and Stark (2013) among others. Thus, the main motivation behind Paper I is to address the challenges observed in the earlier works.

Key contributions and findings

Like Robinson (1998, 2018), we made the connection between optical and seismic holography (i.e., Kirchhoff migration). Analogous to the broken hologram (c.f., 3.1.3), it should be possible to significantly undersample the seismic input data, while still obtaining a high-resolution image. However, as optical holograms are diffraction-driven, we tailored our input seismic data by use of diffraction separation techniques. Following the earlier works, we proposed regular undersampling of the input data, resulting in coherent noise in the output image. It has been demonstrated, by use of both controlled and field data, that well-resolved images can be obtained from significantly undersampled input data. However, in the original works of Neidell and Robinson, the methodology was not fully developed and tested. We therefore introduced two important extensions to make holistic migration applicable to seismic field data. First, we proposed to use diffraction-enhanced data to comply with the basic assumption of diffraction-dominated input data. Second, we suggested a novel signal processing approach that efficiently removes the operator noise (crosstalk) caused by the regular data decimation. Moreover, the diffraction separation technique employed in this work is computationally demanding. Application of the concept of holistic migration can therefore decrease the computational time significantly. This can effectively be done by limiting the diffraction separation to every n-th trace and employing holistic migration to reconstruct a well-sampled image.

5.2 Paper II:

Electromagnetic resolution - A CSEM study based on the Wisting oil field

Vemund S. Thorkildsen and Leiv-J. Gelius.

Geophysical Journal International, Volume 233, Issue 3 (2023): 2124–2141.

Motivation and objectives

The marine Controlled Source Electromagnetic (CSEM) technique is used to map subsurface resistivity from surface measurements of magnetic and electric fields induced by a controlled source. Current studies process CSEM data by employing inversion techniques that can handle complex and anisotropic earth models in 3D (Brown et al., 2012; Wang et al., 2018; Jakobsen & Tveit, 2018). Ideally, every inversion result should be accompanied by a proper description of the uncertainty and resolution of the inverted model. Menke (2012) describes how to quantify the resolution of an inversion using two resolution matrices: the *data resolution matrix* and *the model resolution matrix*. Paper II assesses both resolution matrices to investigate their applicability within CSEM inversion. The literature includes several examples of the use of resolution matrices to analyze various inversion problems. However, within CSEM inversion, this is usually limited to simple applications of the model resolution matrix (Grayver et al., 2014; Mckay et al., 2015; Mattsson, 2015). This motivated us to publish a rigorous analysis of marine CSEM inversion with an emphasis on data redundancy and the full set of resolution matrices.

Key contributions and findings

In Paper II, we demonstrated that a typical CSEM survey is associated with significant data redundancy. A framework of analysis has been developed to efficiently employ the information carried by the resolution matrices and derived quantities. This workflow was implemented in a self-developed user interface, which interfaces seamlessly with the open-source MARE2DEM software. The columns in the model resolution matrix are known as point spread functions (PSF), and describe how a delta-like perturbation in the model will be blurred. However, as each model parameter is associated with its own PSF, we proposed a new metric, denoted as the *ratio of resolution*, to quantify the resolving power of the full dataset. Moreover, we proposed employing the diagonal of the data resolution matrix (*data importances*) to guide the subsampling. The feasibility of the proposed approach was demonstrated by employing both synthetic data computed from an interpreted model of the Wisting oil field in the Barents Sea and actual field data from the same oil field.

5.3 Paper III:

Resolution enhancement of 2D CSEM images by use of PSF inversion

Vemund S. Thorkildsen and Leiv-J. Gelius.

Submitted to *Frontiers in Earth Science.* Special issue: *Advances in Geophysical Inverse Problems.*

Motivation and objectives

Since EM wave propagation is associated with significant attenuation, only very low frequencies are used. Initially, CSEM data were processed directly in the data domain using normalized magnitude and phase-versus-offset plots (Ellingsrud et al., 2002; Røsten et al., 2003). During the last two decades, the processing of CSEM data has moved to the model domain through inversion. However, improvements in computing power and inversion techniques can not overcome the low-frequency content of CSEM data. This implies that the actual inversion result represents a blurred version of the true Earth model. In general, the blurring of an imaging system is quantified via the point spread function. Several publications in seismic data imaging and inversion (Hu et al., 2001; Sjoeberg et al., 2003; Yu et al., 2006; Takahata et al., 2013; Yang et al., 2022) perform further deblurring of images by employing PSF inversion. These previous publications motivated us to employ similar techniques in case of marine CSEM data.

Key contributions and findings

As mentioned, the process of PSF inversion has been successfully employed to improve the resolution of geophysical images. Paper III represents the first published attempt to deblur CSEM images by PSF inversion. This was carried out by extracting PSFs from a regularized Gauss-Newton inversion, while the actual deblurring was done by using the nonnegative flexible conjugate gradient least-squares (NN-FCGLS) algorithm. In addition, we employed a blind deconvolution based on maximum likelihood estimation (MLE) with unknown PSFs to attain completeness of the study. The potential of the proposed approach has been demonstrated using both complex synthetic data and field data acquired at the Wisting oil field in the Barents Sea. In both cases, the resolution of the final inversion result was improved and showed greater agreement with the known target area. Moreover, it was found that the results obtained from space-varying deconvolution outperformed both invariant and blind deconvolution.

Chapter 6

Discussion and outlook

In this thesis work, we have investigated several methods capable of increasing (or retaining) resolution in geophysical imaging and inversion. Paper I and II both investigate how to retain resolution with significantly undersampled input data for seismic and CSEM data respectively. Furthermore, Paper III investigates how to improve the resolution of CSEM inversions by use of PSF inversion.

In Paper I, we challenged the conventional understanding of the Nyquist-Shannon sampling criterion. As mentioned, several examples of undersampling seismic data can be found in the literature. However, all of these publications (including Paper I) only consider undersampling in one dimension (i.e., either space or time/depth). Thus, none of these publications properly consider undersampling of the full data volume, and it is likely that such undersampling will be accompanied with additional challenges. However, such a study is of value. We specialize to the case of diffraction separated data, as undersampling such data can be seen as analogous to the broken hologram (cf. Section 3.1.3). Moreover, we followed previous publications and adopted regular spatial undersampling. However, in the main body of this thesis, we explored different undersampling strategies, including regular and random undersampling with varying apertures. Introducing random undersampling in holistic migration results in a distinctly different noise pattern than for the regular undersampling case. The noise is then less coherent, which might result in less noise when contributions from several diffractions are superimposed. However, the results presented in this thesis also emphasize the importance of utilizing the full available aperture. Thus, by adopting regular undersampling, we ensure that all parts of the (randomly placed) diffraction points are covered equally.

As mentioned earlier, the pioneering papers of Neidell (1997); Robinson (1998, 2018) recognized the different characteristics of reflections and diffractions. Yet, these studies proposed to employ reflection data as input to holistic migration, and did not properly address the operator noise that is introduced. As reflections have a much smaller Fresnel aperture than diffractions, median filtering of the migration operators will remove the reflected events, leading to a poor migration result. Section 3.5 of this thesis presents a new approach to holistic migration for reflection data based on machine learning. In essence, this proposed approach wraps the summation of the migration operator into a neural network, which is trained (supervised training) to remove unwanted artifacts. Although the proposed method shows promising results for this dataset, it must be recognized that the Sigsbee2a dataset represents an idealized case, with strong diffractions and (generally) flat reflectors with strong amplitudes. However, this contribution can be seen as an introductory study of holistic migration for reflection data, where the noise concern is specifically addressed. Note that without a doubt, limits exist on how far we can undersample reflection data (or diffraction data for that matter) while still retaining resolution. For example, if the data is undersampled so severely that the contribution from a reflection is completely removed from the input data (due to a smaller Fresnel aperture), there is no algorithm that can recover such an event. A possible method to further improve the proposed machine learning approach might be to include several neighbouring migration operator panels.

As mentioned in Section 2.2, due to the complex imaging condition caused by the guided modes in electromagnetic data, the use of migration is not very practical. Thus, the proposed regular undersampling advocated for in case of seismic data in Paper I will not yield a good inversion result. The electromagnetic inversion problem is notoriously underdetermined; Paper II therefore proposes a more targeted undersampling strategy based on well-known inversion theory. The proposed approach has demonstrated that the resolution matrices carry essential information in the case of CSEM inversion. Such information can be used to subsample data without losing essential resolving power.
However, some challenges are also observed regarding the proposed method. In a nodal marine CSEM acquisition, it is common to acquire a full survey with regular spatial sampling of the receivers. In a 3D layout, this can include up to 200 receivers, and it is highly unlikely that all receivers contribute equally to the inversion. It should therefore be possible to remove the least influential receivers without losing essential resolving power. The results presented in synthetic data case 2 of Paper II support this claim. However, it should be noted that such an undersampling should only be done if a satisfactory inversion result has been achieved. By moving away from regular spatial sampling, it might still be possible to preserve a high resolution. Shantsev et al. (2020) describe how the acquisition of a monitor survey with known changes in receiver positions does not necessarily compromise the result, as long as the comparison is made in the model domain. Thus, it may be possible to replace the conventional regularly sampled survey with its sparsely optimized counterpart.

However, inferring the resolving power of a receiver location a priori is associated with some challenges. This issue might be resolved if a high-quality resistivity model is available. For a synthetic data case, where the Earth model is well known, receiver sensitivity studies can be performed in advance. However, in case of field data, the resistivity model is, almost by definition, unknown. In a production setting, which can typically last over 40 years, geologists build a deep understanding of a range of lithological properties. Building on this legacy information, it is thus likely possible to construct a representative resistivity model. An interesting idea for furthering this approach might be to investigate to which extent a synthetic model can be used to infer the resolving power of different receiver positions. In essence, such a study can be made by constructing a synthetic baseline model, which will represent the 'true' model of the study. This is followed by quantifying the resolving power for a range of receiver positions. Then, a second model with known changes in the resistivity distribution is constructed. Note that both models should be constructed in close collaboration with geologists. The resolving power of the corresponding receiver locations can then be quantified and compared to the true model.

Another challenge regarding improvements to survey design in a production setting relates to corresponding changes in the reservoir. During production, resistivity is expected to decrease. This phenomenon might again introduce changes in the sensitivity of the different receiver locations. Shantsev et al. (2020) address this concern and demonstrate that time-lapse effects due to production are preserved in the inverted domain even in cases with major differences in survey layout between base and monitor data. Nonetheless, a detailed study of such effects with emphasis on the resolution matrices would be of value.

As mentioned earlier, because EM wave propagation is associated with significant attenuation, only very low frequencies are used, resulting in a blurred inversion model. Thus, in Paper III, we propose to further deblur the inversion by making use of the PSFs originally computed as part of Paper II. The proposed deblurring approach is based on PSFs extracted from the resolution matrix associated with a linearized approximation of the original nonlinear problem. Thus, this procedure does not represent an exact solution to the blurring problem, and the results obtained should always be treated with caution. However, given the obvious computational advantage of deblurring over full inversion (minutes versus days with our resources), the approach has some merit. Moreover, it was found that the results obtained from space-varying deconvolution outperformed both invariant and blind deconvolution. Future work should address the optimal choice of PSFs and the particular choice of deblurring algorithm. Furthermore, there will always be challenges associated with iterative inversion algorithms, and further work should address concerns such as when to terminate the iterations or if the problem can be regularized in a different way. However, the main motivation of Paper III was to demonstrate the deblurring of CSEM data for the first time.

Bibliography

Asgedom, E. G., Gelius, L.-J., Faccipieri, J., & Tygel, M. (2012). 2-D pre-and post-stack diffraction separation and imaging. In *SEG Technical Program Expanded Abstracts 2012* (pp. 1–5). Society of Exploration Geophysicists. DOI: https://doi.org/10.1190/segam2012-0655.1.

Bannister, P. R. (1968). Determination of the electrical conductivity of the sea bed in shallow waters. *Geophysics*, 33(6), 995–1003.

Berkovitch, A., Belfer, I., Hassin, Y., & Landa, E. (2009). Diffraction imaging by multifocusing. *Geophysics*, 74(6), WCA75–WCA81. DOI: https://doi.org/10.1190/1.3198210.

Berre, L., Morten, J. P., Baillie, G., & Nerland, E. (2020). Experience on controlled-source electromagnetic performance for exploration in Norway. *Interpretation*, 8(4), SQ25–SQ37.

Bojarski, N. N. (1983). Generalized reaction principles and reciprocity theorems for the wave equations, and the relationship between the time-advanced and time-retarded fields. *The Journal of the Acoustical Society of America*, 74(1), 281–285.

Born, M. & Wolf, E. (1999). Principles of Optics, 7th (expanded) edition. *United Kingdom: Press Syndicate of the University of Cambridge*, 461, 93.

Brown, V., Hoversten, M., Key, K., & Chen, J. (2012). Resolution of reservoir scale electrical anisotropy from marine CSEM data. *Geophysics*, 77(2), E147–E158.

Byrne, C. (2015). A Brief History of Electromagnetism. *Lowell: University of Massachusetts*.

Cagniard, L. (1953). Basic theory of the magneto-telluric method of geophysical prospecting. *Geophysics*, 18(3), 605–635.

Claerbout, J. F. (1971). Toward a unified theory of reflector mapping. *Geophysics*, 36(3), 467–481.

Coggon, J. & Morrison, H. (1970). Electromagnetic investigation of the sea floor. *Geophysics*, 35(3), 476–489.

Constable, S., Parker, R. L., & Constable, C. G. (1987). Occam's inversion: A practical algorithm for generating smooth models from electromagnetic sounding data. *Geophysics*, 52(3), 289–300.

Constable, S. & Srnka, L. J. (2007). An introduction to marine controlled-source electromagnetic methods for hydrocarbon exploration. *Geophysics*, 72(2), WA3–WA12.

Cooper, R. & MacGregor, L. (2020). CSEM: Back from the Brink. *GEO ExPro Magazine*, 17(5), 38–40.

Dafni, R. & Symes, W. W. (2017). Diffraction imaging by prestack reverse-time migration in the dip-angle domain. *Geophysical Prospecting*, 65(S1), 295–316.

Dell, S. & Gajewski, D. (2011). Common-reflection-surface-based workflow for diffraction imaging. *Geophysics*, 76(5), S187–S195.

Eidesmo, T., Ellingsrud, S., MacGregor, L., Constable, S., Sinha, M., Johansen, S., Kong, F., & Westerdahl, H. (2002). Sea bed logging (SBL), a new method for remote and direct identification of hydrocarbon filled layers in deepwater areas. *First break*, 20(3).

Ellingsrud, S., Eidesmo, T., Johansen, S., Sinha, M., MacGregor, L., & Constable, S. (2002). Remote sensing of hydrocarbon layers by seabed logging (SBL): Results from a cruise offshore Angola. *The Leading Edge*, 21(10), 972–982.

Esmersoy, C. & Oristaglio, M. (1988). Reverse-time wave-field extrapolation, imaging, and inversion. *Geophysics*, 53(7), 920–931.

Faccipieri, J. H., Coimbra, T. A., Gelius, L.-J., & Tygel, M. (2016). Stacking apertures and estimation strategies for reflection and diffraction enhancement. *Geophysics*, 81(4), V271–V282. DOI: https://doi.org/10.1190/geo2015-0525.1.

Fomel, S. (2002). Applications of plane-wave destruction filters. *Geophysics*, 67(6), 1946–1960. DOI: https://doi.org/10.1190/1.1527095.

Friedel, S. (2003). Resolution, stability and efficiency of resistivity tomography estimated from a generalized inverse approach. *Geophysical Journal International*, 153(2), 305–316.

Gabor, D. (1948). A new microscopic principle. *Nature*, 161, 777–778. DOI:https://doi.org/10.1038/161777a0.

Gazzola, S., Hansen, P. C., & Nagy, J. G. (2019). IR Tools: a MATLAB package of iterative regularization methods and large-scale test problems. *Numerical Algorithms*, 81(3), 773–811.

Gazzola, S. & Wiaux, Y. (2017). Fast nonnegative least squares through flexible Krylov subspaces. *SIAM Journal on Scientific Computing*, 39(2), A655–A679.

Gelius, L.-J. & Asgedom, E. (2011). Diffraction-limited imaging and beyond–the concept of super resolution. *Geophysical Prospecting*, 59(3), 400–421.

Gilbert, W. (1893). *On the Loadstone and Magnetic Bodies, and on the Great Magnet the Earth: A New Physiology, Demonstrated with Many Arguments and Experiments*. Wiley.

Girard, J.-F., Coppo, N., Rohmer, J., Bourgeois, B., Naudet, V., & Schmidt-Hattenberger, C. (2011). Time-lapse CSEM monitoring of the Ketzin (Germany) CO2 injection using 2× MAM configuration. *Energy Procedia*, 4, 3322–3329.

Gray, S. (2011). Seismic migration. In H. Gupta (Ed.), *Encyclopedia of solid earth geophysics* (pp. 1236–1244). Springer Science & Business Media.

Grayver, A. V., Streich, R., & Ritter, O. (2014). 3D inversion and resolution analysis of land-based CSEM data from the Ketzin CO 2 storage formation. *Geophysics*, 79(2), E101–E114.

Hagedoorn, J. G. (1954). A process of seismic reflection interpretation. *Geophysical prospecting*, 2(2), 85–127.

Hansen, P. C., Nagy, J. G., & O'leary, D. P. (2006). *Deblurring images: matrices, spectra, and filtering*. SIAM.

Hoeber, H., Pelissier, M., Moser, T. J., & Klem-Musatov, K. (2017). Seismic diffractions: How it all began. *First Break*, 35(2).

Hu, J., Schuster, G. T., & Valasek, P. A. (2001). Poststack migration deconvolution. *Geophysics*, 66(3), 939–952.

Jakobsen, M. & Tveit, S. (2018). Distorted Born iterative T-matrix method for inversion of CSEM data in anisotropic media. *Geophysical Journal International*, 214(3), 1524–1537.

Key, K. (2016). MARE2DEM: a 2-D inversion code for controlled-source electromagnetic and magnetotelluric data. *Geophysical Journal International*, 207(1), 571–588.

Klokov, A. & Fomel, S. (2012). Separation and imaging of seismic diffractions using migrated dip-angle gathers. *Geophysics*, 77(6), S131–S143.

Langenberg, K. J. (1987). Applied inverse problems for acoustic, electromagnetic and elastic waves. *Basic methods of tomography and inverse problems*.

Leith, E. N. & Upatnieks, J. (1965). Photography by laser. *Scientific American*, 212(6), 24–35.

Levin, F. K. (1971). Apparent velocity from dipping interface reflections. *Geophysics*, 36(3), 510–516. DOI: https://doi.org/10.1190/1.1440188.

Li, G., Li, Y., Han, B., & Liu, Z. (2018). Application of the perfectly matched layer in 3-D marine controlled-source electromagnetic modelling. *Geophysical Journal International*, 212(1), 333–344.

Mattsson, J. (2015). Resolution and Precision of Resistivity Models from inversion of Towed Streamer EM data. In *2015 SEG Annual Meeting*: OnePetro.

Maurer, H., Boerner, D. E., & Curtis, A. (2000). Design strategies for electromagnetic geophysical surveys. *Inverse Problems*, 16(5), 1097.

Mckay, A., Mattson, J., & Du, Z. (2015). Towed Streamer EM–reliable recovery of sub-surface resistivity. *First Break*, 33(4).

Menke, W. (2012). *Geophysical data analysis: discrete inverse theory: MATLAB edition*, volume 45. Academic press.

Mitolo, M. & Araneo, R. (2019). A Brief History of Electromagnetism [History]. *IEEE Industry Applications Magazine*, 25(2), 7–11.

Mittet, R., Maaø, F., Aakervik, O. M., & Ellingsrud, S. (2005). A two-step approach to depth migration of low frequency electromagnetic data. In *SEG Technical Program Expanded Abstracts 2005* (pp. 522–525). Society of Exploration Geophysicists.

Moser, T. & Howard, C. (2008). Diffraction imaging in depth. *Geophysical Prospecting*, 56(5), 627–641.

Nagy, J. G. & O'leary, D. P. (1997). Fast iterative image restoration with a spatially varying PSF. In *Advanced Signal Processing: Algorithms, Architectures, and Implementations VII*, volume 3162 (pp. 388–399).: SPIE.

Neidell, N. S. (1997). Perceptions in seismic imaging Part 2: Reflective and diffractive contributions to seismic imaging. *The Leading Edge*, 16(8), 1121–1123.

Neidell, N. S. & Taner, M. T. (1971). Semblance and other coherency measures for multichannel data. *Geophysics*, 36(3), 482–497. DOI: https://doi.org/10.1190/1.1440186.

Pajak, J. (2005). Signal processing in the "Zhang Heng Seismograph" for remote sensing of impending earthquakes. In *1st International Conference on Sensing Technology November* (pp. 21–23).

Porter, R. P. (1970). Diffraction-limited, scalar image formation with holograms of arbitrary shape. *JOSA*, 60(8), 1051–1059.

Ren, Z. & Kalscheuer, T. (2020). Uncertainty and resolution analysis of 2D and 3D inversion models computed from geophysical electromagnetic data. *Surveys in Geophysics*, 41(1), 47–112.

Rikitake, T. (1948). Notes on electromagnetic induction within the Earth. *Bull. Earthq. Res. Inst*, 24(1), 4.

Robinson, E. A. (1998). Further to Norman Neidell's series.... Holistic migration. *The Leading Edge*, 17(3), 313–320. DOI: https://doi.org/10.1190/1.1437960.

Robinson, E. A. (2018). Extended resolution: Neidell is right. *The Leading Edge*, 37(1), 33–36.

Røsten, T., Johnstad, S., Ellingsrud, S., Amundsen, H., Johansen, S., & Brevik, I. (2003). A Sea Bed Loggin (SBL) Calibration Survey over the Ormen Lange Gas Field. In *65th EAGE Conference & Exhibition* (pp. cp–6).: European Association of Geoscientists & Engineers.

Schleicher, J., Tygel, M., & Hubral, P. (2007). *Seismic true-amplitude imaging.* Society of Exploration Geophysicists.

Schneider, W. A. (1978). Integral formulation for migration in two and three dimensions. *Geophysics*, 43(1), 49–76.

Schwarz, B. (2019). An introduction to seismic diffraction. In *Advances in Geophysics*, volume 60 (pp. 1–64). Elsevier.

Shantsev, D. V., Nerland, E. A., & Gelius, L.-J. (2020). Time-lapse CSEM: how important is survey repeatability? *Geophysical Journal International*, 223(3), 2133–2147.

Simpson, F. & Bahr, K. (2005). *Practical magnetotellurics.* Cambridge University Press.

Sinha, M. C., Patel, P., Unsworth, M., Owen, T., & MacCormack, M. (1990). An active source electromagnetic sounding system for marine use. *Marine Geophysical Researches*, 12(1-2), 59–68.

Sjoeberg, T. A., Gelius, L. J., & Lecomte, I. (2003). 2-D deconvolution of seismic image blur. In *2003 SEG Annual Meeting*: OnePetro.

Srnka, L. J. (1986). Method and apparatus for offshore electromagnetic sounding utilizing wavelength effects to determine optimum source and detector positions. US Patent 4,617,518.

Stark, T. J. (2013). Signal recovery beyond conventional Nyquist: The sample rates used for seismic acquisition do not need to limit the maximum recoverable frequencies. *The Leading Edge*, 32(11), 1334–1339.

Tabti, H., Gelius, L.-J., & Hellmann, T. (2004). Fresnel aperture prestack depth migration. *First Break*, 22(3).

Takahata, A., Gelius, L., Lopes, R., Tygel, M., & Lecomte, I. (2013). 2D spiking deconvolution approach to resolution enhancement of prestack depth migrated seismic images. In *75th EAGE Conference & Exhibition incorporating SPE EUROPEC 2013* (pp. cp–348).: European Association of Geoscientists & Engineers.

Thorkildsen, V. S. (2019). Separation of diffractions by diffraction-stacking and Plane-Wave Destruction filtering. Master's thesis, University of Oslo, http://urn.nb.no/URN:NBN:no-73150.

Thorkildsen, V. S. & Gelius, L.-J. (2023). Electromagnetic sensitivity - A CSEM study based on the Wisting oil field. *Geophysical Journal International*, (pp. to appear).

Thorkildsen, V. S., Gelius, L.-J., & Robinson, E. A. (2021). Revisiting holistic migration. *The Leading Edge*, 40(10), 768–777.

Tikhonov, A. (1950). On determining electrical characteristics of the deep layers of the Earth's crust. In *Doklady*, volume 73 (pp. 295–297).: Citeseer.

Vinje, V., Lie, J., Danielsen, V., Dhelie, P., Siliqi, R., Nilsen, C., Hicks, E., Walters, C., & Camerer, A. (2017). Shooting over the Streamer Spread-A Novel Approach in Seismic Marine Acquisition and Imaging. In *79th EAGE Conference and Exhibition 2017*.

Wang, F., Morten, J. P., & Spitzer, K. (2018). Anisotropic three-dimensional inversion of CSEM data using finite-element techniques on unstructured grids. *Geophysical Journal International*, 213(2), 1056–1072.

Wiggins, J. (1984). Kirchhoff integral extrapolation and migration of nonplanar data. *Geophysics*, 49(8), 1239–1248.

Wisecup, R. D. (1998). Unambiguous signal recovery above the Nyquist using random-sample-interval imaging. *Geophysics*, 63(2), 763–771.

Wright, D. A., Ziolkowski, A. M., & Hobbs, B. A. (2005). Detection of subsurface resistivity contrasts with application to location of fluids. US Patent 6,914,433.

Xu, L., Sun, W.-Q., Yan, Y.-H., & Zhang, W.-Q. (2020). Solar image deconvolution by generative adversarial network. *Research in Astronomy and Astrophysics*, 20(11), 170.

Yang, J., Huang, J., Zhu, H., McMechan, G., & Li, Z. (2022). An efficient and stable high-resolution seismic imaging method: Point-spread function deconvolution. *Journal of Geophysical Research: Solid Earth*, 127(7), e2021JB023281.

Yilmaz, Ö. (2001). *Seismic data analysis: Processing, inversion, and interpretation of seismic data*. Society of exploration geophysicists.

Young, P. D. & Cox, C. S. (1981). Electromagnetic active source sounding near the East Pacific Rise. *Geophysical Research Letters*, 8(10), 1043–1046.

Yu, J., Hu, J., Schuster, G. T., & Estill, R. (2006). Prestack migration deconvolution. *Geophysics*, 71(2), S53–S62.

Papers

Paper I

Revisiting holistic migration

Vemund Stenbekk Thorkildsen, Leiv-J Gelius, Enders A. Robinson

Published in *The Leading Edge*, October 2021, volume 40, issue 10, pp. 768–777. DOI: https://doi.org/10.1190/tle40100768.1.

Paper II

Electromagnetic resolution - A CSEM study based on the Wisting oil field

Vemund Stenbekk Thorkildsen, Leiv-J Gelius

Published in *Geophysical Journal International*, June 2023, volume 233, issue 3, pp. 2124–2141. DOI: https://doi.org/10.1093/gji/ggad046.

Geophysical Journal International

Geophys. J. Int. (2023) **00,** 1–20 https://doi.org/10.1093/gji/ggad046
Advance Access publication 2023 February 01
Marine geosciences and applied geophysics

Electromagnetic resolution—a CSEM study based on the Wisting oil field

Vemund Stenbekk Thorkildsen[†] and Leiv-J Gelius

Department of Geosciences, University of Oslo, Sem Sælands vei 1, 0371 Oslo, Norway. E-mail: vemund.s.thorkildsen@gmail.com

Accepted 2023 January 31. Received 2023 January 31; in original form 2022 April 5

SUMMARY

We consider marine controlled source electromagnetic (CSEM) data and demonstrate that a typical CSEM survey is associated with significant data redundancy. Thus, it should be possible to obtain a high-quality inversion result by using only a subset of the original data. Moreover, in survey design, effort should be made to optimize the placement of the receivers. This study therefore investigates the challenges of data decimation and survey design in the case of repeated surveys by use of the *data resolution matrix* and *model resolution matrix*. A framework of analysis has been developed to efficiently use these quantities. The feasibility of the proposed approach is demonstrated using both synthetic data computed from an interpreted model of the Wisting oil field in the Barents Sea, as well as actual field data from the same oil field.

Key words: Arctic region; Controlled source electromagnetics (CSEM); Marine electromagnetics; Inverse theory.

1 INTRODUCTION

The marine controlled source electromagnetic (CSEM) technique is used to map subsurface resistivity from surface measurements of magnetic and electric fields induced by a controlled source. For an exhaustive review of the development of marine CSEM, the reader is referred to (Constable 2010) and (Zhdanov 2010). Current studies process CSEM data by using inversion techniques that can handle complex and anisotropic earth models in 3-D (Brown *et al.* 2012; Jakobsen & Tveit 2018; Wang *et al.* 2018). Ideally, every inversion result should be accompanied by a proper description of the uncertainty and resolution of the inverted model. Menke (2012) describes how to quantify the resolution of an inversion using two resolution matrices: the *data resolution matrix* and the *model resolution matrix*. The data resolution matrix describes how well the data prediction matches the observed data, while the model resolution matrix describes how well each parameter in a discrete model is resolved. This study assesses both resolution matrices to investigate their applicability within CSEM inversion.

The literature includes several examples of the use of resolution matrices to analyse various inversion problems. For example, Friedel (2003) introduced a low-contrast inversion algorithm for electrical resistivity tomography data, which also provided an estimate of uncertainty, data resolution, and model resolution. Kalscheuer *et al.* (2010) used similar techniques to evaluate the resolution and variance properties for single and joint inversions of magnetotelluric (MT) and direct current data. Other studies discuss simple applications of the model resolution matrix within CSEM inversion (Grayver *et al.* 2014; Mattsson 2015; McKay *et al.* 2015). However a rigorous analysis of marine CSEM inversion with an emphasis on data redundancy and the resolution matrices has not yet been published.

CSEM acquisition systems can largely be divided into towed streamer and nodal acquisition approaches. In the early 2010s, Petroleum Geo-Services (PGS) developed a towed streamer acquisition system, which was later abandoned (Engelmark *et al.* 2014). Another example of towed streamer CSEM is the Scripps Institution of Oceanography's Vulcan acquisition system, which is often combined with seabed nodes (Constable *et al.* 2016). However, a significant amount of data is still acquired using seabed nodes. Because deploying the nodal receivers comprises a significant portion of the costs associated with acquiring CSEM data, it is of interest to try to minimize the number of receivers used (especially in 3-D). This is especially important in the case of repeated surveys, which can be essential in a production setting or in a CO_2 storage project. In this study, we will investigate the feasibility of using resolution matrices for survey design purposes.

Romdhane & Eliasson (2018) quantified the importance of different datapoints by evaluating the approximate Hessian as part of the CSEM inversion. This information can then be used for survey design. By omitting the least important data (quantified by the Hessian), it is possible to remove a larger part of the data set while still obtaining a good inversion result. The approximate Hessian method allows for efficient subsampling of the data set, and thus decreasing

---

[†] Department of Geosciences, P.O Box 1047 Blindern, NO-0316 Oslo, Norway.

the computational demand. However, because the approximate Hessian is constructed from the Jacobian matrix, which only contains first-order derivatives with respect to model parameters, the important effects of regularization of the inverse problem are not properly considered (Menke 2012; Ren & Kalscheuer 2020). We therefore present an alternative approach representing a more systematic emphasis on survey design based on the full set of resolution matrices and derived quantities.

As a starting point, this study uses the open-source inversion package MARE2DEM (Modelling with Adaptively Refining Elements 2D for Electromagnetics). This package integrates a model builder (Mamba2D), forward modelling, inversion and data display capabilities for CSEM and other electromagnetic (EM) inversion problems (Key 2016). However, MARE2DEM provides the user with a very simple measure of sensitivity based only on the Jacobian matrix. To remedy this, we have developed an extensive toolbox for post-processing of the CSEM inversion result, which includes resolution matrices and derived quantities. We demonstrate how access to such measures provides additional useful insight into the quality of the inversion results. Thus, both resolution and robustness are addressed in the context of CSEM inversion using a synthetic earth model.

Many of the synthetic models used for CSEM studies are either 1-D (Key 2009; Roux & García 2014) or very simple (Weitemeyer *et al.* 2010). Several high-quality synthetic seismic models (e.g. Marmousi, Sigsbee2a) are publicly available, allowing for the testing of algorithms on known, but complex models. This is in stark contrast to CSEM, where such models are very difficult to find. Two notable exceptions are the SEG Advanced Modelling (SEAM) initiative (Stefani *et al.* 2010), which provides modelled CSEM data that can be licensed for a fee, and the Marlim R3D model (Carvalho & Menezes 2017; Correa & Menezes 2019), which is publicly available but limited to low frequencies with focus on deep target exploration. Moreover, no field data from the same area is publicly available as part of MarlimR3D. This motivated us to create a high-quality synthetic model based on the Wisting oil field, an offshore oil field in the Barents Sea where CSEM is proven to add significant value.

This paper is organized as follows. First, the Wisting field is introduced, along with a general description of the local geology. The next section presents CSEM field data acquired across Wisting. This is followed by a description of the model-building workflow. Next, the theoretical framework of forward modelling, inversion and construction of the resolution matrices is discussed. Taking this proposed analysis framework, we demonstrate its practical use on both synthetic and field data. Finally, a discussion and conclusion section ends the paper with an eye toward future applications of the model for more efficient CSEM data collection.

2 THE WISTING OIL FIELD

To study the sensitivity of EM methods for exploration purposes, it is essential to use high-quality synthetic models of the subsurface. As mentioned, such resistivity models are not easily available. Accordingly, such a model must be constructed from the ground up. In this study, we have chosen to build a synthetic model based on the Wisting oil field. The proposed model-building workflow is described in the subsequent section. However, it is first necessary to provide a general introduction to the Wisting oil field.

The Wisting oil field is located in the Hoop Fault Complex (*cf.* Fig. 1a), a northern region of the southwestern Barents Sea. With an estimated 500 million barrels of oil equivalents, the field is a prime candidate for further development. However, in addition to the remote location of the oil field, several geological issues pose challenges for development. Senger *et al.* (2021) describe four major tectonic phases that have shaped the southwestern Barents Sea. The first phase was governed by the Palaeozoic Caledonian orogeny, followed by erosion of the Caledonian mountain chain. The second phase was defined by a Carboniferous to Permian extension, while the third phase was dominated by a sag basin formation. Erosion of the Uraldine mountain chain and the Northern Fennoscandian shield, along with continued subsidence, created a prograding shelf delta. This tectonic phase saw the deposition of thick sandstone-dominated formations, like the Middle Jurassic Stø formation, which serves as the main oil-bearing reservoir in the Wisting field. The fourth tectonic phase was dominated by uplift and erosion and can be seen as the most important process for the preservation of the current oil accumulations. The crest of the oil-bearing structure currently lies approximately 200 m below the seafloor after being uplifted roughly 1350 m from the late Cretaceous to early Palaeogene (Senger *et al.* 2021). Such a deep burial depth led to mechanical and chemical compaction, resulting in reduced porosity and permeability in the oil-bearing formations. Moreover, Fig. 1(b) highlights the faulted nature of the oil reservoir, caused by the major uplift. The average seafloor depth is about 400 m.

The oil-bearing section of the reservoir consists of three main formations. The aforementioned Stø formation is the primary hydrocarbon bearing unit, while the Nordmela and Fruholmen formations comprise the remaining parts of the reservoir (Granli *et al.* 2017). The main geological formations are outlined in the zoomed subsection of Fig. 1(b).

2.1 Electric properties of the Wisting field

The Wisting field is of particular interest due to its high resistivity values (Fig. 2), with the Stø formation regularly exceeding the maximum limit of the resistivity logger (100 000 Ωm) locally in the borehole. Such local extremities might be explained by an oil-wet reservoir, causing exceptional resistance to electric flow. However, it is believed that there are inaccuracies in the well log when encountering such high resistivity values. Supporting this claim, forward models with the original resistivity values lead to unrealistically high field strengths. As previously mentioned, the top reservoir lies only 200 m below the seabed, and the combination of shallow burial depth and high resistivity makes it an ideal candidate for constructing a high-quality resistivity model. To guide and calibrate the building of a synthetic model of the Wisting field, it is vitally important to access both resistivity logging data, high-quality CSEM, and seismic field data from the same area. The shallow burial depth means that a large frequency band (<12 Hz) is sensitive to the reservoir, which allows for easier tuning of the electric model by use of CSEM field data. Due to the low resolution of CSEM data compared to seismic data, it is crucial to use the latter to establish the reservoir geometry.

2.2 CSEM field data

In this study, we have access to CSEM field data from a 2-D line extracted from the BSMC08W 3-D survey, which was conducted in the summer of 2008 and belongs to the multiclient library of Electromagnetic Geoservices (EMGS). The corresponding selected

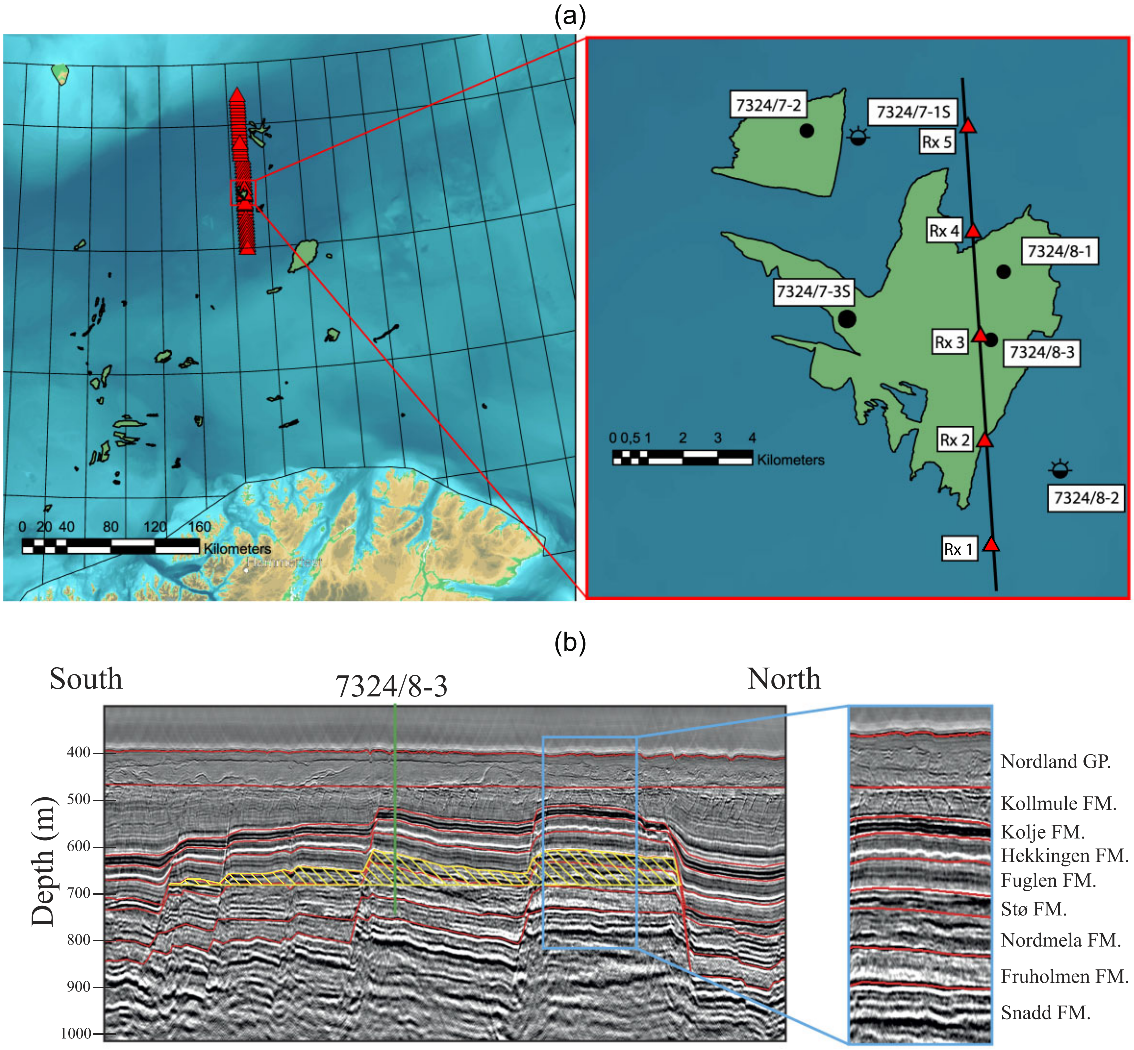

Figure 1. (a) Map of the southwestern Barents Sea along with a zoomed section of the Wisting oil field. The selected receivers of the extracted 2-D CSEM line are highlighted with red triangles, while the 2-D seismic depth line is shown in black. Nearby exploration wells are also highlighted. The data was acquired with a tow direction from south to north. Datapoints where the source is south of its corresponding receiver are therefore denoted in-tow, while the out-tow will have the source north of the corresponding receiver. (b) Seismic depth section showing the Wisting field along with the most important formations (annotated in the zoomed subsection). The approximate reservoir is highlighted in yellow.

receiver locations are highlighted in Fig. 1(a). Fig. 3 displays the source signature in the frequency domain, with the black bars representing the magnitude of the Fourier coefficients of the processed field data input to the inversion. The corresponding grey bars represent the theoretical discrete Fourier spectrum of the raw source signature. As expected, only minor differences exist. It is evident that most of the energy of this vintage data set is concentrated towards the lower frequencies ($<$4 Hz).

Processing of the raw data was carried out by EMGS, including the extraction of the 2-D CSEM line used in this study. Further processing was conducted by the authors to reduce the computational time of the inversion process. This included a resampling of the transmitter interval to 200 m. Fig. 4 shows the layout of the transmitter and receiver positions that were ultimately used. Note that, in case of receiver position 4, the transmitter interval is shifted 100 m.

Plots of the magnitude and phase of the inline horizontal electric field component at 2 Hz are shown in Fig. 5 (Receiver 2 in Fig. 1a). Fig. 5 also includes a normalized Magnitude Versus Offset (MVO) plot computed for the same receiver, which shows that the maximum field strength of the out-tow direction is about three times larger than the corresponding in-tow direction. This receiver gather only shows the response from the use of a single frequency. However, by using the full available band of frequencies (*cf.* Fig. 3) and multiple receiver locations, it should be possible to fine-tune an earth model with a representative resistivity distribution of the true subsurface.

However, to achieve a geologically constrained subsurface model of the electric properties, the use of additional seismic data is needed. This is discussed in greater detail in the next section, which describes the main steps of our suggested approach to build a synthetic model.

3 MODEL BUILDING

Building a high-quality resistivity model is not a trivial task. In order to construct a realistic resistivity model, depth-migrated seismic field data is used as a structural constraint and the structural model is populated with resistivity values from well log data. The

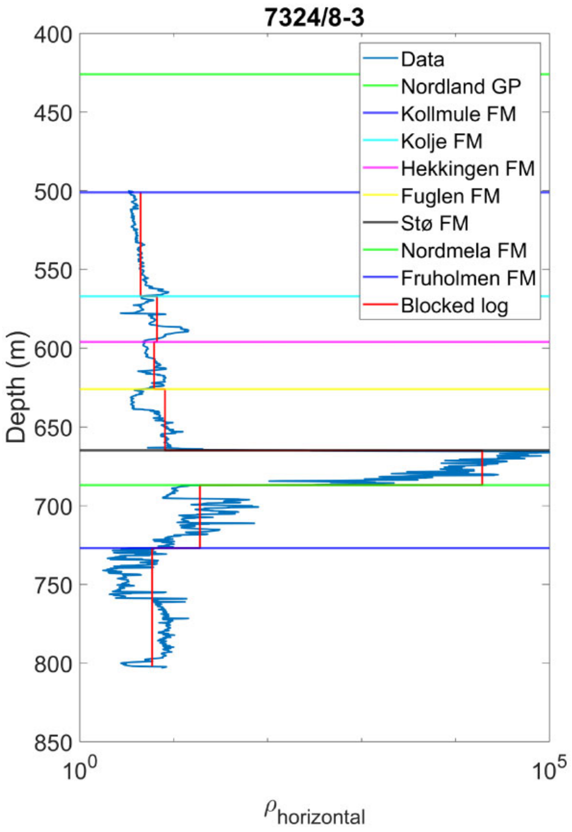

Figure 2. Deep resistivity log for well 7324/8-3 (see Fig. 1a) with labelled formation tops. Note also the discrete vertical red lines, which represent the upscaled (average) value in each formation and serve as a starting point for synthetic model building.

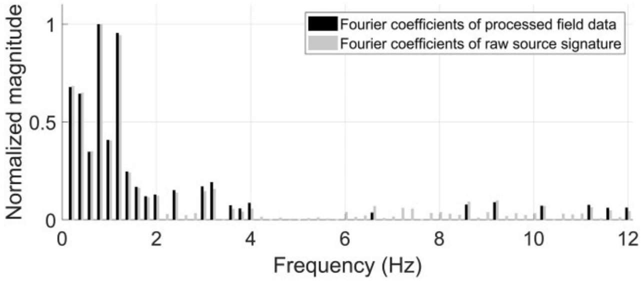

Figure 3. Source signature in the frequency domain. The black coefficients correspond to the processed data, while the grey bars show the raw source spectrum. Both sets of coefficients are normalized with the maximum amplitude of their respective data sets.

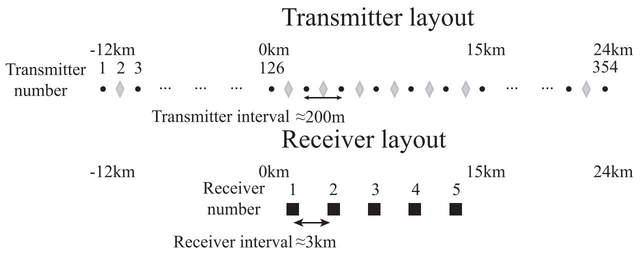

Figure 4. Survey layout after resampling to 200 m transmitter interval. The receiver interval is about 3 km, while the transmitter interval is around 200 m. Note that the transmitter positions of Receiver 4 (represented by grey diamonds in the transmitter layout) is shifted by 100 m compared to that of the other receivers.

freely available Marlim R3D uses a similar strategy for structural constraint, but takes a more sophisticated approach to populating the resistivity model (Carvalho & Menezes 2017). Building a 2-D resistivity model entails two primary problems: (i) extracting a 2-D line from a 3-D CSEM survey and (ii) identifying a 2-D seismic line in close proximity (Fig. 1a). The field data used in this paper represents the measured response of a 3-D structure. When interpreting the main (or target) horizons of the model, it is therefore essential to verify that only minor geological variations exist in the crossline direction of the selected 2-D line.

In addition, it must be recognized that the CSEM method is not sensitive to small-scale heterogeneities. Therefore, smaller faults should not invalidate the assumption of the 2-D experiment. Depth slices of a 3-D seismic data cube indicate that the selected data line used in this work should not be compromised by major structural faults (Granli *et al.* 2017), although some distortions may arise due to more rapid resistivity variations caused by changes in oil saturation. If such distortions are prominent, they would be expected to manifest in the southern part of the line (Fig. 1a). After selecting the most optimal combination of seismic and EM data, structural interpretation can be carried out. For this purpose, Petrel was used (Schlumberger 2018). After interpretation, the horizons are heavily downsampled before being imported to the model builder. For this purpose, we used the model builder Mamba2D, which is part of the MARE2DEM package. Mamba2D creates a mesh node at every point in the imported horizons. For computational efficiency, it is therefore ideal to begin with a sparse starting mesh that MARE2DEM can adaptively refine during the forward modelling process (Key 2016).

For this study, we have chosen to populate the model with resistivity values based on simple averaging of the deep resistivity logging measurements within blocks bounded by geologic formations (Fig. 2). This approach carries some limitations; well logs only provide a very local measure of the resistivity. Thus, the resistivity might vary greatly only a few metres away from the well path. In comparison, CSEM is a low-frequency technique and will only be sensitive to large volumes in our model. Moreover, vertical well logs only provide a measure of horizontal resistivity. By only using the horizontal resistivity, we are assuming the resistivity is isotropic. In the case of CSEM, this assumption can lead to poor inversion results. This can intuitively be understood by considering a layered earth. Assuming that the earth is isotropic leads to the conclusion that the electric current flows equally well in all directions. In other words, the current would be assumed to flow across lithological boundaries just as it flows along a uniform layer. Earlier studies have shown that a moderate ratio of vertical to horizontal resistivity of 2:3 may have a significant effect on the inversion result (Lu & Xia 2007; Newman *et al.* 2010; Brown *et al.* 2012).

Moreover, because CSEM data are generally more sensitive to vertical resistivity, using an isotropic inversion scheme to an anisotropic earth biases the inversion towards higher resistivity values (Hoversten *et al.* 2006). We did not have access to vertical resistivity measurements for this project. However, the operator of the Wisting oil field (Equinor) provided representative values of anisotropy. Fig. 6 shows the synthetic model colour-coded with the vertical component of the resistivity. The final vertical resistivity values in all formations are listed in Table 1, along with the ratio of vertical to horizontal resistivity ($\frac{\rho_z}{\rho_{xy}}$) and a brief lithology description. All anisotropy factors fall within the typical range found in the literature. To account for inaccuracies in the well logging tool when encountering such extreme resistivity values as seen in

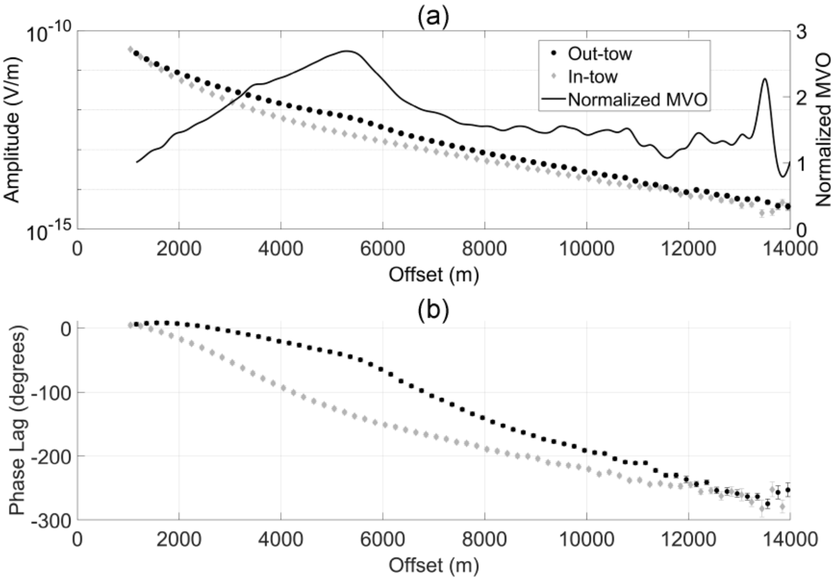

Figure 5. Field data example of the inline horizontal electric field component for Receiver 2. (a) MVO for the in-tow direction (represented by grey diamonds) and the out-tow direction (represented by black dots) along with normalized MVO, which is calculated as the ratio of the data of interest (i.e. out-tow) and an assumed background response (i.e. in-tow). (b) Phase lag for the same receiver.

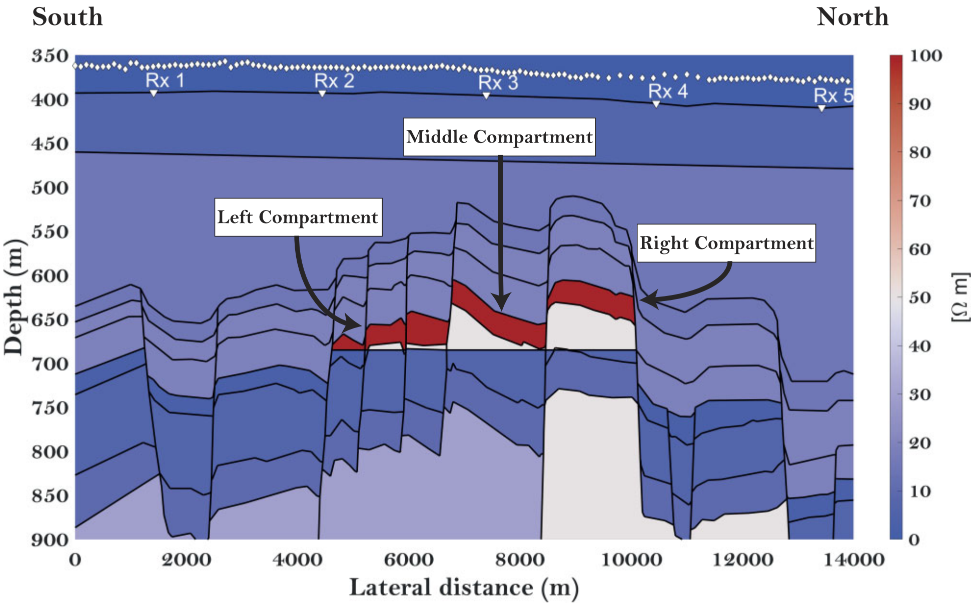

Figure 6. Synthetic model after tuning (colour coded with vertical resistivity). Note that the colour bar only shows values up to 100 Ωm to emphasize the resistivity variations in the different geological formations (see Table 1 for resistivity values). The reservoir can be divided into three compartments, defined by three main fault blocks. The left compartment is further subdivided into three fault blocks. However, when addressed in the text we refer to all three fault blocks.

the Stø formation, we had to tune the model in order to achieve a satisfactory data fit (Fig. 7). In general, the resistivity values in the inverted models from both the field data and synthetic data fit well. It should be noted that the tuning was done with the aim of creating a reasonable resistivity model for testing our method, and such tuning should not be done with interpretation in mind.

4 ELECTROMAGNETIC SENSITIVITY—INVERSION THEORY AND THE RESOLUTION MATRIX

In CSEM inversion, the largest computational bottleneck is the repeated forward modelling of the EM fields, due to the many source points and frequencies. However, methods to decrease the computational load do exist. Electromagnetic reciprocity can be exploited to decrease the computational burden in the case of nodal marine CSEM, where source points typically greatly outnumber receivers.

Table 1. Vertical and horizontal resistivity values chosen for the final model. Note that Stø and Nordmela are listed twice, as these two formations form the oil reservoir. The resistivity of the oil-filled Stø formation is also listed with a range, since an optimal data fit could only be achieved if different resistivity values were assigned for each compartment of the reservoir. The lithology description is taken from Senger *et al.* (2021).

Formation	ρ_z [Ohm-m]	$\frac{\rho_z}{\rho_{xy}}$	Lithology
Nordland Gp	7	2.3	Marine shale
Kollmule Fm	15	3.4	Marine shale
Kolje Fm	15	2.7	Marine shale
Hekkingen Fm	19.5	3.2	Marine/organic rich shale
Fuglen Fm	19.5	2.4	Marine shale
Stø Fm (oil-filled)	1500–2500	1	Sandstone
Stø Fm (brine-filled)	3	2	Sandstone
Nordmela Fm (oil-filled)	50	1	Marine shale/sandstone
Nordmela Fm (brine-filled)	7	2	Marine shale/sandstone
Fruholmen Fm	10	2	Alluvial shale/sandstone
Snadd Fm	30	2	Marine shale

Electromagnetic reciprocity states that, for a linear medium, the position and orientation of a receiver and transmitter can be swapped, and still measure the same response. The medium is defined as linear if the magnetic permeability μ, dielectric permittivity ϵ, and electric conductivity σ do not depend on the magnetic $\mathbf{H}$ or electric $\mathbf{E}$ field intensity. In practice, this means that we swap the position and orientation of the receivers and source points (Parasnis 1988). In the case of a towed streamer CSEM survey, reciprocity will not yield a significant decrease in computational time, as the number of source and receiver points are approximately equal.

However, even after exploiting electromagnetic reciprocity, the forward problem remains computationally demanding. This emphasizes the question of how much of the data we really need to use, and especially how many frequencies are needed. We propose the combined use of the model resolution matrix and data resolution matrix to quantify the importance of each data parameter. By examining the resolution matrices, we can remove datapoints which do not contribute significantly to our target area.

4.1 MARE2DEM

MARE2DEM is an open-source forward modelling and inversion software developed by the Scripps Seafloor Electromagnetic Consortium. The package is described in detail by Key (2016), so we will only give a brief introduction to the main concepts for completeness.

All electromagnetic induction methods aim to map the subsurface in terms of resistivity (or conductivity) by using either a natural or an artificial (i.e. active) source. Based on the measured electric field responses of the subsurface, a quantitative image of the earth model can be recovered by inversion. In CSEM inversion, we need to solve for the electric fields using Maxwell's equations on a discrete grid. This can effectively be done by using finite difference or finite element solvers. When such discrete solvers are used, the accuracy of the forward modelling critically depends on the modelling mesh. By introducing a fine grid, the forward modelling will likely be very accurate, but the cost of this accuracy is high computational demand. MARE2DEM uses an adaptively refining finite element forward modelling scheme. This means that if the base is a sparse model with few mesh nodes, the program will refine the different grid cells based on a stability criterion (Key 2016).

When field data are acquired, the earth model extends infinitely, and the measurements approach noise only when the separation between the source and receivers increases (e.g. below the detection threshold of the acquisition equipment). However, when modelling the data, it is necessary to limit the size of the model to decrease the computational burden. This can be implemented by using an absorbing boundary condition such as a perfectly matched layer (Li *et al.* 2018). However, because MARE2DEM does not have these absorbing boundary conditions implemented, it is necessary to use a large model to avoid edge effects.

4.2 Inversion

In an iterative inversion process, the forward modelling response is calculated in the current model, and a misfit or cost function representing the error between the calculated response and the actual response is constructed. By minimizing this misfit, the model is updated in an iterative manner. Following Ren & Kalscheuer (2020), this cost function can formally be written as:

$$U[\mathbf{m}, \alpha] = Q_d[\mathbf{m}] + \alpha Q_m[\mathbf{m}], \tag{1}$$

where $\mathbf{m}$ is the model vector, $Q_d[\mathbf{m}]$ is the model dependent data misfit and $Q_m[\mathbf{m}]$ is the regularization term that simplifies the solution space. The Lagrangian multiplier α acts as a weight factor between the data misfit term and the regularization term, thereby balancing resolution and stability. MARE2DEM uses a variation of Occam inversion denoted 'fast Occam' (Key 2016). This is an implementation of the Gauss–Newton optimization scheme, in which the model update is done by building the Jacobian matrix of sensitivities. Calculating the Jacobian matrix involves simulating the response of all the sources (forward fields) and receivers (adjoint fields). Thus, reciprocity would not yield any decrease in computation time. However, each Occam iteration includes a grid search for the Lagrangian multiplier by calculating the model update and forward response for a range of α-values. The forward modelling in this grid search does not involve calculating the Jacobian matrix, and will therefore be faster by using reciprocity in the case of marine nodal acquisition. For more details regarding Occam inversion and its specific implementation in MARE2DEM, the reader is referred to, respectively, Constable *et al.* (1987) and Key (2016). The MARE2DEM package optionally includes a reference model. However, because this is not included in our analysis, the inversion relies solely on a roughness penalty for regularization. Eq. (1) can be expanded as follows:

$$U[\mathbf{m}, \alpha] = \left[(\mathbf{d} - \mathbf{F}[\mathbf{m}])^{\dagger}\mathbf{W}_{\mathbf{d}}^{\dagger}\mathbf{W}_{\mathbf{d}}(\mathbf{d} - \mathbf{F}[\mathbf{m}])\right] + \alpha \mathbf{m}^{\dagger}\mathbf{W}_{\mathbf{m}}^{\dagger}\mathbf{W}_{\mathbf{m}}\mathbf{m}, \tag{2}$$

where $\mathbf{d}$ denotes the measured complex field data and $\mathbf{F}[\mathbf{m}]$ denotes the model response. Working with complex fields requires us to use the Hermitian † (i.e. matrix transpose + complex conjugation) for the matrices involved. The data misfit is also weighted by $\mathbf{W}_{\mathbf{d}}$, a diagonal matrix consisting of the inverse of the standard error for each sample. The regularization term includes the weighting matrix $\mathbf{W}_{\mathbf{m}}$ to enforce model smoothness. In MARE2DEM, this is obtained using a gradient roughness operator. For anisotropic models, the roughness is augmented by splitting the model vector into anisotropic subsets (Key 2016).

Since our problem is non-linear, the forward operator is linearized in the vicinity of the current model $\mathbf{m}_k$ by use of a Taylor series expansion:

$$\mathbf{F}[\mathbf{m}_{k+1}] \approx \mathbf{F}[\mathbf{m}_k] + \mathbf{J}(\mathbf{m}_{k+1} - \mathbf{m}_k). \tag{3}$$

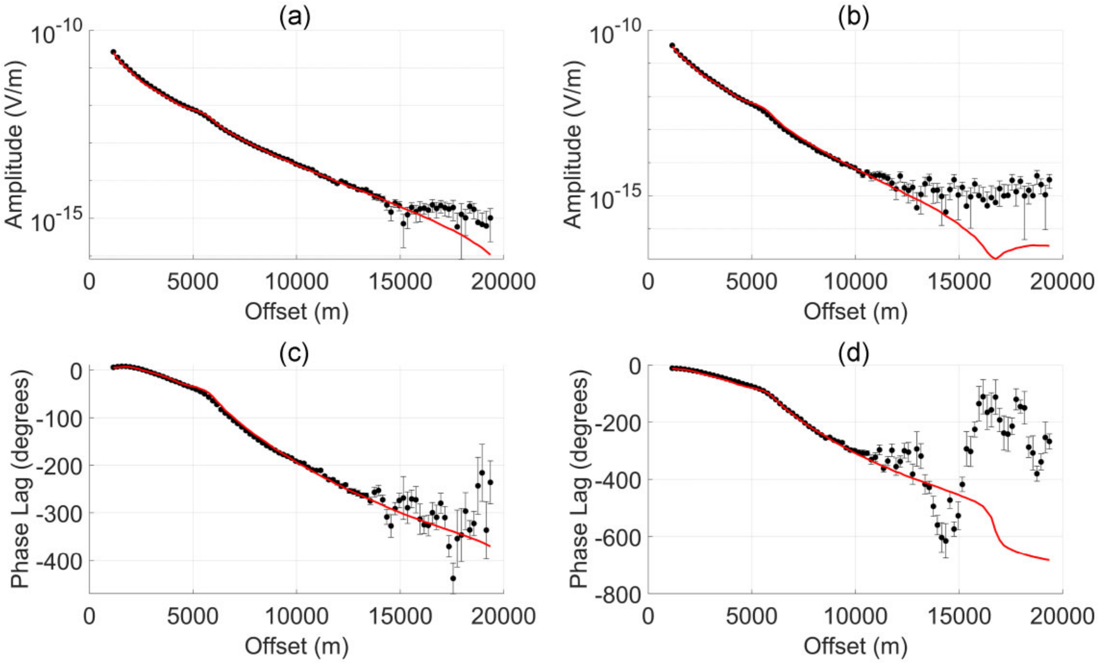

Figure 7. Field data (dots) and synthetic response (line) for Receiver 2. On the left-hand side, MVO (a) and PVO (c) are shown for a 2 Hz response, while on the right-hand side the MVO (b) and PVO (d) are shown for 4 Hz. For both frequencies, the synthetic data fit well with the field data (until the noise floor is reached at an amplitude of around 10^{-15} V m^{-1}). The vertical bars associated with the field data represent data uncertainty.

The Jacobian or sensitivity matrix **J** (with entries $\frac{\partial F_i(\mathbf{m}_k)}{\partial \log(\rho_j)}$, where ρ_j is the resistivity in cell j), includes the first-order partial derivatives with respect to model parameters (log resistivity). Note also that MARE2DEM outputs the data and Jacobian matrix in the same format as the input. Wheelock *et al.* (2015) found that, in electromagnetic inversion, the most computationally efficient and robust approach is to use phase lag and logarithmically scaled amplitude as input. Thus, we adapted the same input format in this study. However, because we are working with complex fields, it is necessary to transform the Jacobian matrix into its complex field equivalent. For more details regarding the calculation of the Jacobian and the transformation to its complex field equivalent, the reader is referred to Appendix A. Combining eqs (2) and (3) yields the following:

$$\begin{aligned} U^{lin}[\mathbf{m}_{k+1}, \alpha] \\ = \Big[\Big(\mathbf{d} - \mathbf{F}[\mathbf{m}_k] - \mathbf{J}(\mathbf{m}_{k+1} - \mathbf{m}_k) \Big)^{\dagger} \mathbf{W}_{\mathbf{d}}^{\dagger} \mathbf{W}_{\mathbf{d}} \Big(\mathbf{d} - \mathbf{F}[\mathbf{m}_k] - \mathbf{J}(\mathbf{m}_{k+1} - \mathbf{m}_k) \Big) \Big] \\ + \alpha \mathbf{m}_{k+1}^{\dagger} \mathbf{W}_{\mathbf{m}}^{\dagger} \mathbf{W}_{\mathbf{m}} \mathbf{m}_{k+1}. \end{aligned} \tag{4}$$

A least squares solution is obtained by setting $\frac{\partial U^{lin}[\mathbf{m}_{k+1},\alpha]}{\partial \mathbf{m}_{k+1}}$ to zero and solving for $\mathbf{m}_{k+1}$:

$$\mathbf{m}_{k+1} = \mathbf{J}_w^{-g} \mathbf{W}_{\mathbf{d}} \mathbf{d}_k, \tag{5}$$

where $\mathbf{d_k} = [\mathbf{d} - \mathbf{F}[\mathbf{m}_k] + \mathbf{J}\mathbf{m}_k]$ and $\mathbf{J}_w^{-g}$ is the generalized inverse $[\mathbf{J}^{\dagger}\mathbf{W}_{\mathbf{d}}^{\dagger}\mathbf{W}_{\mathbf{d}}\mathbf{J} + \alpha \mathbf{W}_{\mathbf{m}}^{\dagger}\mathbf{W}_{\mathbf{m}}]^{-1}\mathbf{J}^{\dagger}\mathbf{W}_d^{\dagger}$. It is possible to include a total of six different data components relating to the three different directions of the magnetic and electric field in the inversion. However, this study only makes use of the inline horizontal electric field (E_y).

4.3 Model resolution matrix

Here, let $\mathbf{m}_k$ denote the inversion obtained from the final (kth) iteration of an inversion cycle. By assuming that model $\mathbf{m}_k$ is linearly close to the true earth model $\mathbf{m}_{\mathrm{true}}$, we can write the following equation:

$$\mathbf{d} = \mathbf{F}[\mathbf{m}_{\mathrm{true}}] + \mathbf{n} \approx \mathbf{F}[\mathbf{m}_k] + \mathbf{J}(\mathbf{m}_{\mathrm{true}} - \mathbf{m}_k) + \mathbf{n}, \tag{6}$$

where **n** denotes noise. Consequently, the data prediction for iteration k can be approximated as follows:

$$\mathbf{d}_k = (\mathbf{d} - \mathbf{F}[\mathbf{m}_k] + \mathbf{J}\mathbf{m}_k) \approx \mathbf{J}\mathbf{m}_{\mathrm{true}} + \mathbf{n}. \tag{7}$$

Combining eqs (5) and (7) yields:

$$\mathbf{m}_{k+1} = \mathbf{R}_{\mathbf{M}} \mathbf{m}_{\mathrm{true}} + \mathbf{J}_w^{-g} \mathbf{W}_d \mathbf{n}. \tag{8}$$

In eq. (8), $\mathbf{R}_{\mathbf{M}}$ is the *model resolution matrix* (Menke 2012), and is explicitly given as:

$$\mathbf{R}_{\mathbf{M}} = \Re \left[\left[\mathbf{J}^{\dagger} \mathbf{W}_{\mathbf{d}}^{\dagger} \mathbf{W}_{\mathbf{d}} \mathbf{J} + \alpha \mathbf{W}_{\mathbf{m}}^{\dagger} \mathbf{W}_{\mathbf{m}} \right]^{-1} \mathbf{J}^{\dagger} \mathbf{W}_{\mathbf{d}}^{\dagger} \mathbf{W}_{\mathbf{d}} \mathbf{J} \right], \tag{9}$$

where $\Re$ implies taking the real part. If the inversion terminates at iteration k, $\mathbf{m}_{k+1}$ is considered the preferred inversion model. The model resolution matrix indicates how close the preferred inversion model is to the true model. Because the model resolution matrix depends on the Lagrangian multiplier α, letting $\alpha \to 0$ allows the model resolution matrix to approach the identity matrix. In such a case, $\mathbf{m}_{k+1}$ is said to be perfectly resolved, and the preferred inversion model only has contributions from $\mathbf{m}_{\mathrm{true}}$ and the noise term (Ren & Kalscheuer 2020). In a real-world case, $\mathbf{m}_{\mathrm{true}}$ is unobtainable, so it is substituted with $\mathbf{m}_k$.

The model resolution matrix can be seen as a blurring filter that describes how the unobtainable true model is reproduced by the inversion. Figs 8(a) and (b) depict a schematic representation of eq. (8) without the error term. Note that these figures show the relationship for a 1-D model. In case of a 2-D model, the model resolution matrix takes the form of a block Toeplitz matrix with Toeplitz blocks (BTTB) if the 2-D image is represented as a vector (lexicographic ordering) (Hansen *et al.* 2006). Parts (a) and (b) of

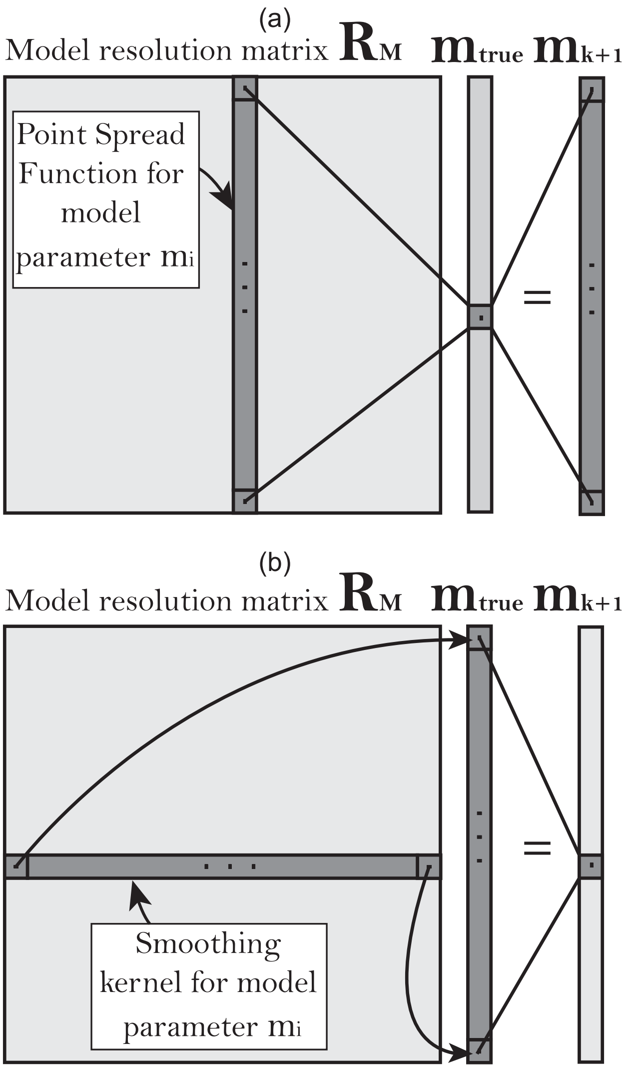

Figure 8. Computational relationship between the resolution matrix ($\mathbf{R_M}$), the unobtainable true model $\mathbf{m}_{\mathrm{true}}$ and the preferred inversion model $\mathbf{m}_{k+1}$. The relationship is shown with an emphasis on the PSF (a) and the Smoothing Kernel (b).

Fig. 8 illustrate, respectively, the column information with an emphasis on the point spread function (PSF) and the row information with an emphasis on the Smoothing Kernel. The PSF is well known from imaging theory (Rossmann 1969) and describes how an imaging system responds to an impulse. Assigning a delta function in $\mathbf{m}_{\mathrm{true}}$, the PSF describes how this delta function spreads across the inverted model $\mathbf{m}_{k+1}$ (Fig. 8a). The Smoothing Kernel describes the extent to which each parameter in the true model contributes to a single model parameter in the inverted model. Although it is well defined, the Smoothing Kernel is more challenging to interpret than the PSF. We have therefore only used the PSFs to quantify resolution power.

In an ideal case, where the model is perfectly resolved, the associated PSFs and Smoothing Kernels are delta functions ($\mathbf{R_M} = \mathbf{I}$). In most cases, such a model is impossible to obtain; the PSF will vary across the model space. However, in a general inversion, it is likely that some areas will be well resolved, and others more poorly resolved. The PSF in well-resolved areas will be characterized by a small spread centred on the associated model parameter. PSFs in poorly resolved areas can be characterized by a large spread, an off-centred maximum, or a combination of the two.

Fig. 9 shows the resolution matrix of an inversion of synthetic data calculated from the model in Fig. 6. The resolution matrix is difficult to evaluate in its full form. However, it can be reorganized to form 2-D slices representing either PSFs or Smoothing Kernels. Because we are free to choose which datapoints should contribute when constructing $\mathbf{R_M}$, it is therefore possible to select different subsets of input data and evaluate the corresponding changes in the PSFs. However, it is extremely labour-intensive to evaluate all the PSFs, so it is therefore advisable to construct a metric summarizing the quality of the selected data. Friedel (2003) tackles this challenge by introducing the *radius of resolution*:

$$r_{\mathrm{res},i} = \frac{r_0}{\sqrt{R_{M,ii}}}, \tag{10}$$

where r_0 represents an inscribed circle for a given model element i and $R_{M,\,ii}$ represents the corresponding value of the diagonal element of the resolution matrix for the same model parameter. This measure breaks down if the highest value is off-diagonal. In such cases, Friedel (2003) introduces a simple distortion flag to mark those cells where the highest value is not centred on the diagonal. As an alternative, we suggest a combined measure that takes into account both the width of the PSF and distortions when the PSF is off-diagonal. We denote this metric the *ratio of resolution*. It is constructed by dividing the diagonal element of $\mathbf{R_M}$ with the sum of all elements falling inside a user-defined ellipsoid. Let V_i denote the ellipsoid centred around model parameter i. The ratio of resolution for model parameter i is then defined as:

$$\mathrm{ratio}_{\mathrm{res},i} = \frac{R_{M,ii}}{\sum_{j=1}^{M} |R_{M,ij}| \in V_i}. \tag{11}$$

The size of V_i is found by trial and error. This study used an ellipsoid defined by a 150-m vertical minor axis and a 1000-m lateral major axis. The model resolution matrix can be constructed irrespective of the data input. Thus, it is possible to combine different subsets of data and quantify their resolving power by evaluating either the associated PSFs or the ratio of resolution.

4.4 Data resolution matrix

It is possible to construct the ratio of resolution for all combinations of input data. However, this study takes a different approach based on the data resolution matrix, which is constructed as follows. The predicted data for iteration $k + 1$ can be written as:

$$\mathbf{d}_{k+1} = \mathbf{F}[\mathbf{m}_{k+1}], \tag{12}$$

which can be combined with eq. (3) to give

$$\mathbf{d}_{k+1} \approx \mathbf{F}[\mathbf{m}_k] + \mathbf{J}(\mathbf{m}_{k+1} - \mathbf{m}_k). \tag{13}$$

A further combination of eqs (5) and (13) with the definition $\mathbf{d}_k = (\mathbf{d} - \mathbf{F}[\mathbf{m}_k] + \mathbf{J}\mathbf{m}_k)$ leads to:

$$\mathbf{d}_{k+1} \approx \mathbf{R_D}\mathbf{d} + (\mathbf{I} - \mathbf{R_D})(\mathbf{F}[\mathbf{m}_k] - \mathbf{J}\mathbf{m}_k), \tag{14}$$

where $\mathbf{R_D}$ is denoted the data resolution matrix and is given explicitly as:

$$\mathbf{R_D} = \Re\left[\mathbf{J}\left[\mathbf{J}^\dagger\mathbf{W}_d^\dagger\mathbf{W}_d\mathbf{J} + \alpha\mathbf{W}_m^\dagger\mathbf{W}_m\right]^{-1}\mathbf{J}^\dagger\mathbf{W}_d^\dagger\mathbf{W}_d\right]. \tag{15}$$

The diagonal of $\mathbf{R_D}$ is often called *Data Importances* (Maurer *et al.* 2000; Ren & Kalscheuer 2020), and describes how important a data point is in its own prediction.

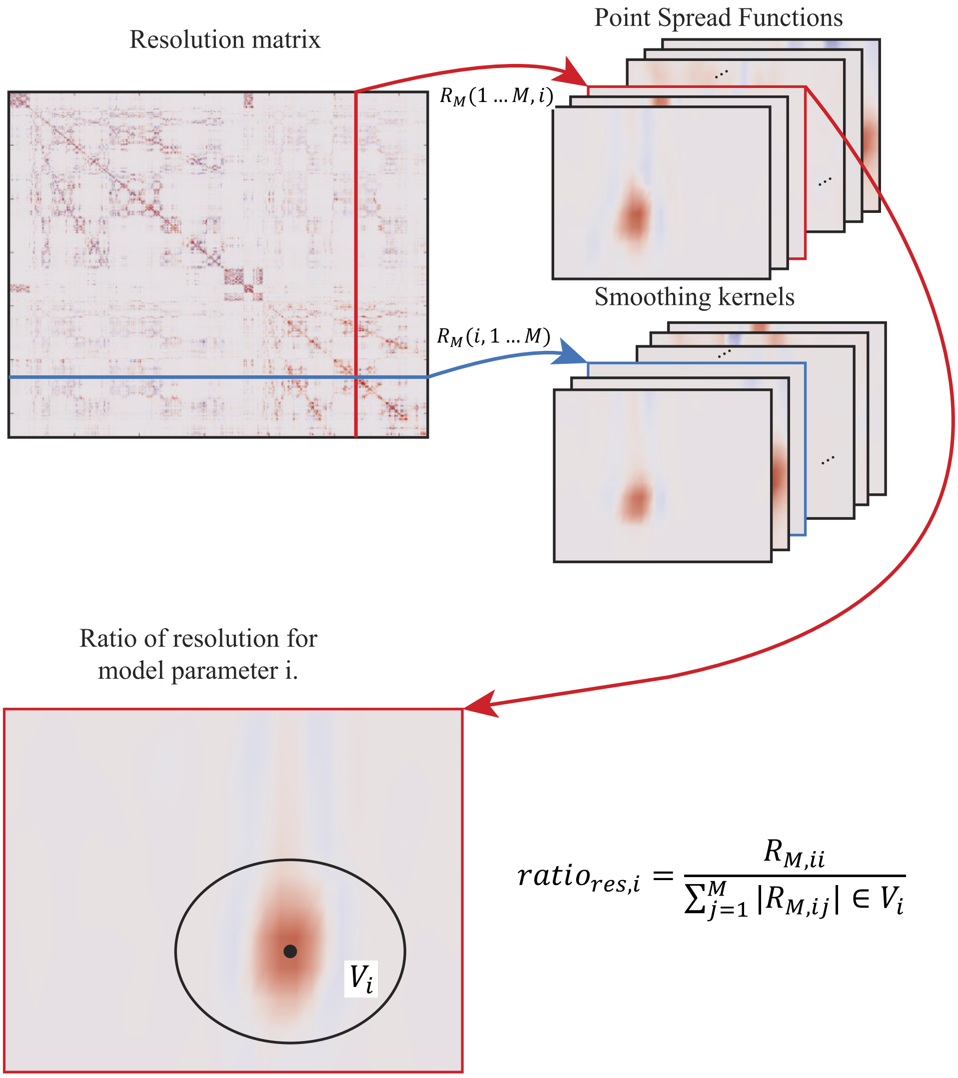

Figure 9. The full model resolution matrix is of size $M \times M$, where M is the length of the model vector. The columns in the resolution matrix define the PSFs, while the rows represent the Smoothing Kernels. The resolution matrix is difficult to evaluate in its original form. However, by reorganizing the rows or columns to fit the model space, it is possible to construct meaningful information in form of Smoothing Kernels or PSFs. To summarize the quality of the set of PSFs chosen, we propose the metric ratio of resolution. In case of model parameter i, it is calculated by dividing the corresponding diagonal element of $\mathbf{R_M}$ ($R_{M,ii}$) with the sum of the absolute value of all elements that fall inside a user-defined ellipsoid V_i.

4.5 Data reduction and planning of repeated surveys

As mentioned, this study proposes using a combination of the data resolution matrix and model resolution matrix to reduce the number of data points used in the inversion. To assess which data points to use, we propose a method in which the Data Importances guide the data selection. We then assess the resulting ratio of resolution to determine whether the target area has lost any important resolving power. The workflow of our proposed method is summarized in Fig. 10.

In the proposed method for data reduction, it is also helpful to evaluate whether Data Importances can truly be used like the name suggests. Therefore, the first step involves computing the data resolution matrix and extracting the Data Importances. This study proposes calculating this quantity on a frequency-per-frequency and receiver-per-receiver basis. The Data Importances are then subsampled by first selecting the percentile value of their full range and then discarding all the values falling below this threshold. The selected data can then be used to calculate the model resolution matrix for the subsampled data set, along with its associated ratio of resolution. A direct comparison between the ratio of resolution map of the complete and decimated data sets should then reveal whether any essential resolving power has been lost. For a given model parameter m_i, a loss in resolving power will manifest as a decrease in $ratio_{res,i}$, with the note that this is an a priori indicator of the resolving power of the subsampled data. This reduced data set can then be used as input for a new inversion.

Another method of using Data Importances relates to repeated surveys. By plotting the Data Importances for each receiver, it is possible to evaluate whether some are more important than others. If one or more receivers are characterized by a very low importance, it might be possible to remove such receivers in a repeated survey.

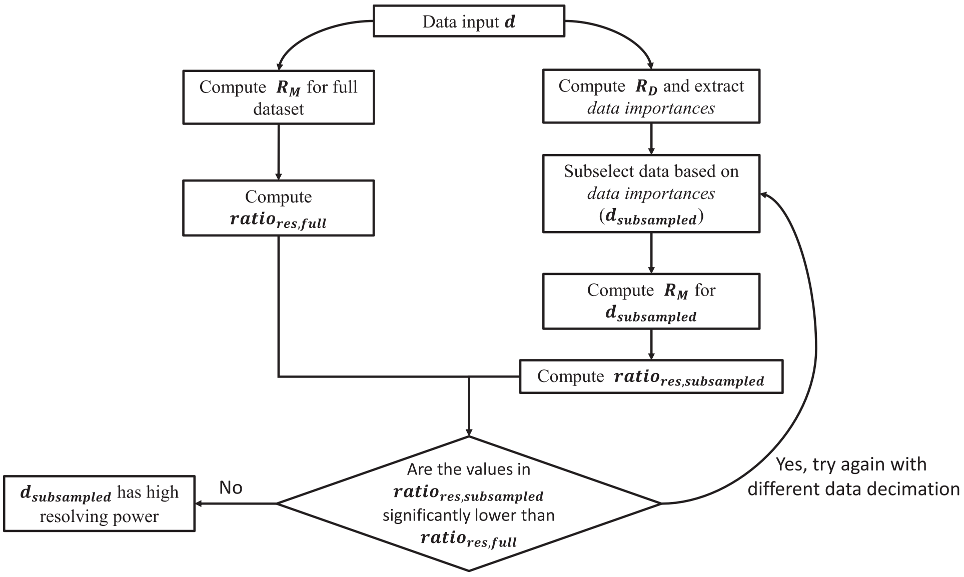

Figure 10. Workflow for data reduction.

5 SYNTHETIC DATA

This section presents the results obtained from testing the workflow in Fig. 10, using the synthetic Wisting data set with the acquisition layout described in Section 2.2. Trials with different initial models did not significantly alter the final inversion result. Thus, we use a simple gradient model in all the inversions presented here. However, for computational efficiency, the inversion is constrained to a region around the known target area. This region reaches down to ≈1600 m below seabed and from −5000 to 20 000 m inline distance (*cf.* Fig. 6). Outside this region, the model parameters are kept fixed and equal to those of the initial model. First, the results obtained from full inversion are presented in the form of PSFs and the calculated Data Importance. Next, the data are subsampled in three different ways and analysed using the proposed workflow. Finally, as a validation, a direct comparison is made between the different inversions.

5.1 Case 1—Full data set

The first experiment uses the full data set up to 12 Hz as data input. The plots shown in Fig. 11 can now be formed following the post-processing steps described in the previous section. Fig. 11(a) shows the PSF of a well-resolved model parameter and demonstrates that the PSF is well centred, exhibiting only one main lobe. Fig. 11(b) shows how the PSF for a poorly resolved model parameter contrasts with the well-resolved model parameter case. The PSF is now off-centre, smeared over a large area with several sidelobes. A direct analysis of the PSFs reveals useful information about resolving power. However, a more efficient computational approach is to use the previously introduced ratio of resolution. An example of this metric is shown in Fig. 12(a). In general, the highest values (associated with good resolution) are found inside the reservoir, while the zones above and below the reservoir are defined by lower values (with the exception of some boundary effects). The final inverted resistivity model is characterized by three main compartments, as shown in Fig. 12(b). Direct comparison with the true (i.e. synthetic) model shown in Fig. 6 demonstrates that the inversion has captured the main features, especially with regard to the lateral extension. However, the image is characteristically smeared over a larger vertical area due to the general lack of resolution of the CSEM method.

5.2 Case 2—Removing the least influential receiver

Figs 11(c) and (d) show the Data Importance for Receivers 2 and 4, respectively. These two receivers are laterally placed on opposing edges of the reservoir (*cf.* Figs 1a and 6). There are clear differences between the two plots, wherein Receiver 2 has higher Data Importance throughout. It should be noted that the Data Importance values of the remaining receivers exhibit the same character as Receiver 2, while Receiver 4 stands out with much lower values. As shown in Fig. 4, Receiver 4 is associated with a shifted line of transmitters compared to the other receivers. This may have played a role.

Based on the Data Importance panels, Receiver 4 carries less important information in the inversion. It should therefore be possible to remove this receiver without losing significant resolving power. A direct comparison of the ratio of resolution for Cases 1 and 2 (Figs 12a and b) reveals that removing Receiver 4 does not significantly change the resolving power. However, an exhaustive validation can only be found by comparing the actual inversion results. Figs 12(b) and (d) show the inverted (vertical resistivity) model for these two cases and confirms that our proposed approach to subselect the data is feasible. It should be noted that this observation is particularly valuable for design of repeated surveys, especially in a 3-D setting.

5.3 Case 3—30 per cent cut-off including lowest frequencies

The promising results of Case 2 imply that further data decimation is possible. However, because none of the remaining receivers are characterized by a low overall Data Importance, the data decimation should now be performed in a different way. As previously suggested, such a decimation can be achieved by calculating a user-provided percentile value of the full data set, then discarding values that fall below this threshold. However, this data decimation would remove all data samples of the lowest frequency (0.2 Hz) from the

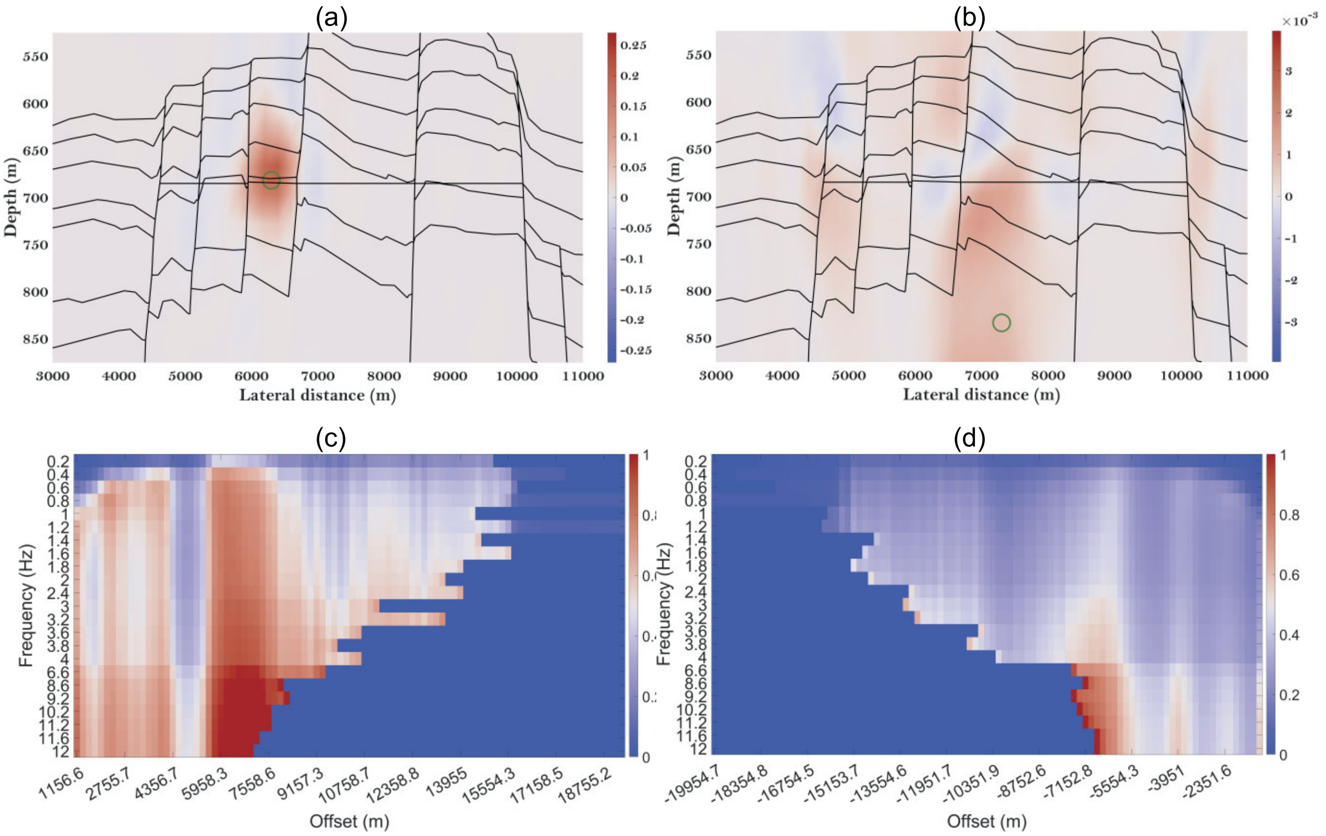

Figure 11. PSF for a well-resolved (a) and poorly resolved model parameter (b), with the circle indicating the position of the parameter. Note that there are two orders of magnitude between the maximum value of the two PSFs. Data Importance is shown as a function of frequency and offset for Receivers 2 (c) and 4 (d). Refer to Figs 1(a) and 6 for receiver locations.

data set. The absence of this low frequency information in initial trials led to a vertical displacement of the reservoir in the inverted model. In Case 3, we therefore propose to discard Receiver 4 and all data points with a Data Importance falling below the 70th percentile. However, all data points of the two lowest frequencies (0.2 and 0.4 Hz) are retained for the remaining receivers (1, 2, 3 and 5) to avoid the observed vertical displacement. The left-hand column in Fig. B1 shows the data subsampling introduced for each receiver (Appendix B). Fig. 12(e) shows the ratio of resolution for this subsampled data set. Based on the quality of this map, the resolving power of this new subsampled data set is expected to be fair. A direct comparison of the inverted models for both Cases 2 and 3 (Figs 12d and f, respectively) reveals that most of the character is retained.

5.4 Case 4—30 per cent cut-off and limited frequencies

Both Cases 2 and 3 only considered data decimation based on Data Importances. Thus, this approach did not place any additional emphasis on which frequencies to transfer to the decimated data set. However, there is good coverage over a large range of frequencies. Therefore, Case 4 subsamples the data set from Case 3 along the frequency dimension. This selection was completed based on several criteria. The source signature in the frequency domain was used as a guide (Fig. 3), along with the Data Importance panels. However, the most important criterion was to evaluate the resolving power of the subsampled data set in form of its ratio of resolution. This can be done by testing different frequency combinations and then evaluating the corresponding ratios of resolution. Directly comparing the ratio of resolution maps for Cases 3 and 4 shows that they are nearly identical (Figs 12e and g). Moreover, this similarity is also reflected in the inverted model domain (*cf.* Figs 12f and h). Refer to the right column of Fig. B1 (Appendix B) for the data subsampling introduced for each receiver.

5.5 Synthetic data—Summary

The four cases presented demonstrate that this study's proposed data decimation scheme is feasible. Table 2 gives the decimation of each case as a percentage of the full data set. It is important to note that all the inverted models exhibit the same character, especially with regard to the three compartments and the lateral extension. Case 2 shows that an entire receiver can be removed without significantly changing the inversion result. As demonstrated by Case 3, even a severe data decimation of ≈61 per cent is feasible without losing essential resolving power. Upon further inspection of the Data Importance panels (Figs 11c and d), it is clear that a large range of frequencies are covered even after Case 3's data decimation. In the final Case 4, we therefore limit the number of frequencies from the original 23 down to 11. Note that this case uses only ≈23 per cent of the original data, while still preserving the main features of the model.

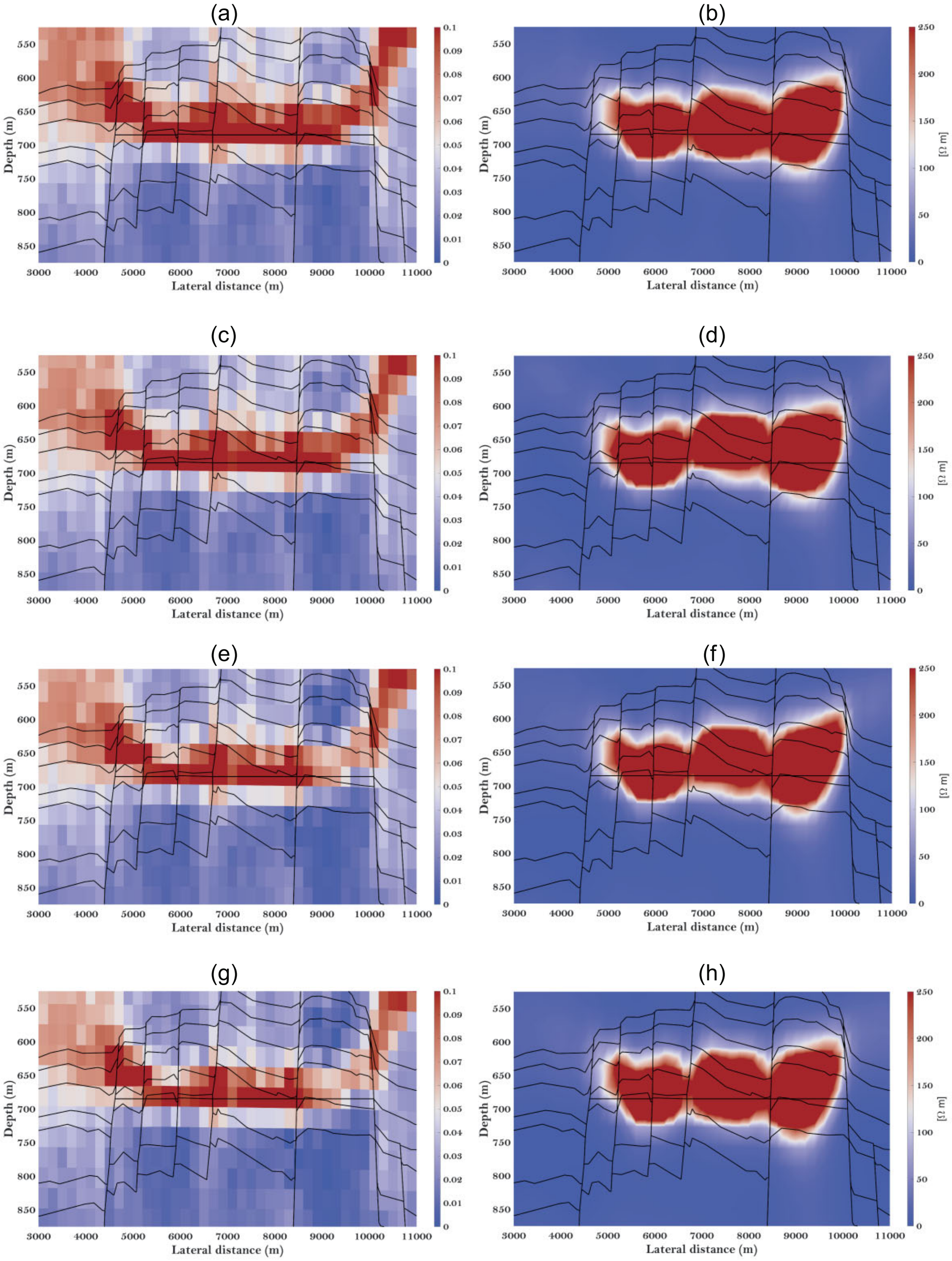

Figure 12. Ratio of resolution for Cases 1 through 4 (a, c, e, g) and corresponding inverted models (b, d, f, h).

6 FIELD DATA

The results presented in the synthetic data section demonstrate that it is possible to severely downsample the original data while still preserving the main features in the final inverted model. However, synthetic data are associated with an ideal model case. Field data, on the other hand, represent the response from a more complicated earth model, with further complications resulting from imperfections in survey and instrumentation. Nonetheless, our proposed approach is still useful in the case of real data. To support this claim, this section provides a simple example from the Wisting field data. In the field data inversion, we used the same starting model as described in Section 5. However, synthetic data allows for full control of the background model. Conversely, for the field data lacking this level of control, a poor inversion result was observed from using the

Table 2. Description of the four cases and the percentage of the full data set used in each inversion.

	Description	Per cent of full data set
Case 1	Full data set Frequencies [Hz]:0.2, 0.4, 0.8, 1, 1.2, 1.4, 1.6,1.8, 2, 2.4, 3, 3.2, 3.6, 3.8,4, 6.6, 8.6, 9.2, 10.2, 11.2, 11.6, 12	100 per cent
Case 2	Removed least influential receiver Frequencies [Hz]:0.2, 0.4, 0.8, 1, 1.2, 1.4, 1.6,1.8, 2, 2.4, 3, 3.2, 3.6, 3.8,4, 6.6, 8.6, 9.2, 10.2, 11.2, 11.6, 12	≈ 82.5 per cent
Case 3	Removed least influential receiver Cut-off at the 70th percentile No cut-off for the two lowest frequencies (0.2 and 0.4 Hz) Frequencies [Hz]:0.2, 0.4, 0.8, 1, 1.2, 1.4, 1.6,1.8, 2, 2.4, 3, 3.2, 3.6, 3.8,4, 6.6, 8.6, 9.2, 10.2, 11.2, 11.6, 12	≈ 39 per cent
Case 4	Removed least influential receiver Cut-off at the 70th percentile No cut-off for the two lowest frequencies (0.2 and 0.4 Hz) Frequencies [Hz]:0.2, 0.4, 0.8, 1.2, 2, 3, 4, 6.6, 9.2, 10.2, 12	≈ 23 per cent

full data set. Thus, the maximum offset was limited to about 10 km to remove such artefacts. The inversion was not constrained by the interpreted horizons, and no constraints were introduced on the maximum resistivity to be recovered.

6.1 Field Case 1—Full data set

A direct comparison between the inversion of the field data and synthetic data reveals that the reservoir has a shallower placement in the field data (Figs 12b and 14b). This effect might arise from attempting to solve a 3-D problem by using a 2.5-D inversion algorithm. When using this 2.5-D technique, we assume no variations in the electrical properties along the strike direction. Moreover, there is also an underlying assumption that the model extends to infinity along the same direction. Thus, the inversion tries to compensate for these inconsistencies by placing the reservoir at a shallower depth. In both the field and synthetic inversions, the reservoir shows three compartments. However, these three compartments are more distinctly separated in the synthetic inversion. Moreover, the lateral extension of the reservoir is virtually the same in both. No distinct differences in resistivity between the three compartments were observed.

Another distinct feature of the Field Case 1 inversion can be seen by examining the rightmost compartment. This compartment is placed deeper in the model, which might be explained by examining the ratio of resolution plot (Fig. 14a). This map reveals that the rightmost compartment is more poorly resolved than the remaining part of the reservoir. Fig. 13 shows the field data along with the modelled response from the inverted model. As briefly mentioned, the offset range in this field data example is limited in order to remove unwanted artefacts. The recovered model accurately describes the field data response for most offsets.

6.2 Field Case 2—Limited frequencies

Some similarities are evident from direct comparison between the Data Importance panels for the field data and synthetic data. The Data Importance of Receiver 4 is generally lower for both the synthetic and field inversions. However, none of the receivers stand out to the extent as seen in the synthetic data case. Thus, it seems that the best approach for field data is to retain all receiver positions. In Field Case 2, we therefore subsample the input data along the frequency direction. We use the same frequency range as in Case 4 for the synthetic data. The subsampled data set corresponds to ≈47 per cent of the full field data set (Table 3). Even with such a severe downsampling, the ratio of resolution and inverted models of Field Cases 1 and 2 are virtually the same (Fig. 14).

7 DISCUSSION

The results show that the resolution matrices carry essential information in the case of CSEM inversion. Such information can be used to subsample data without losing essential resolving power. However, some challenges are also observed regarding the proposed method.

This study introduces Vertical Transverse Isotropy in the inversion, which implies access to both vertical and horizontal resolution matrices. However, we have chosen to limit our reported study to vertical resolution matrices, since CSEM is generally known to be more sensitive to vertical resistivity. Another issue relates to the field components selected for the inversion. Here, the inline horizontal field component (E_y) has been chosen, since it is known to be the most important carrier of information. However, a superior constraint of horizontal resistivity might be achieved by introducing broadside data in the inversion (Masnaghetti & Ceci 2010). While the proposed method for subsampling should also be valid for broadside data, the data analysis would be more comprehensive, as the resolution matrices need to be investigated separately for the different data inputs.

In an exploration setting, it is common to acquire a full survey with regular spatial sampling. However, Case 2 of the synthetic data study illustrates how Data Importances can be used to design a repeated survey. For example, say that the objective is to monitor the Wisting field throughout its lifespan by use of CSEM. First, a baseline survey (with regular spatial sampling) would be acquired before production starts. Thereafter, this baseline survey could be used to calculate resolution matrices and derived quantities. This information can then be used as a guide before acquiring a repeated survey. In a 3-D layout including up to 200 receivers, it is highly unlikely that all receivers contribute equally to the inversion. It should therefore be possible to remove the least influential receivers without losing essential resolving power. Another important point relates to the actual placement of the receivers. By moving away from a regular spatial sampling, it might still be possible to preserve a high resolution. Shantsev *et al.* (2020) describe how the acquisition of a monitor survey with known changes in receiver positions does not necessarily compromise the result, as long as the comparison is made in the model domain. Thus, it may be possible to replace the conventional regularly sampled survey with its sparsely optimized counterpart.

Some challenges exist when seeking to improve survey design. The most fundamental issue is the impossible task of inferring the resolving power of a receiver location a priori. This implies that researchers need to acquire data at a proposed new location to know for certain if it constitutes an improvement. This issue might

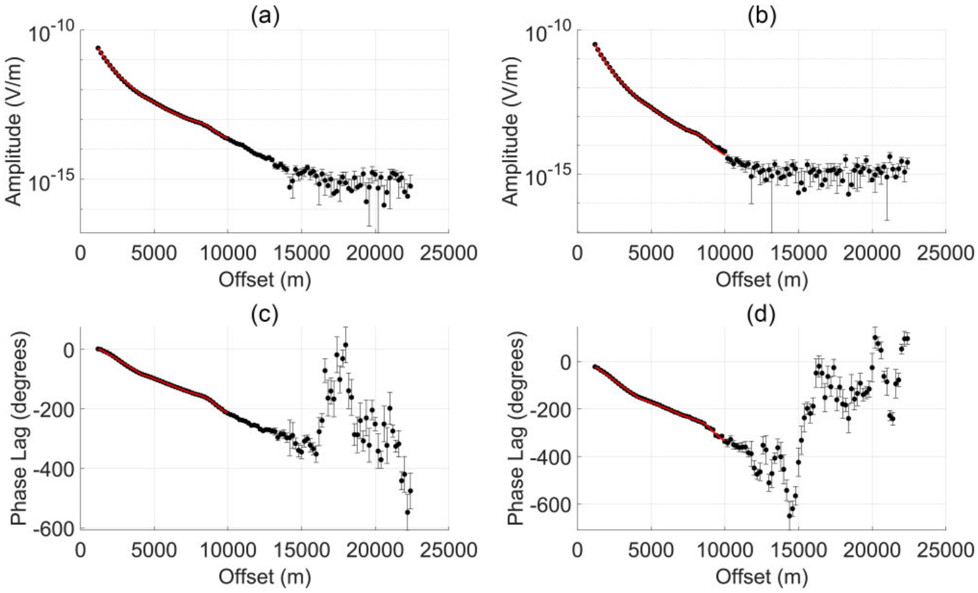

Figure 13. Field data (dots) and modelled response (line) obtained from the inverted model for Receiver 1 (*cf.* Fig. 6). On the left-hand side, MVO (a) and PVO (c) are shown for a 2 Hz response, while on the right-hand side the MVO (b) and PVO (d) are shown for 4 Hz. Note that the offset range has been limited due to the observations described above.

Table 3. Description of the two field cases and the percentage of the full data set used in each inversion.

	Description	Per cent of full data set
Field Case 1	Full data set Frequencies [Hz]:0.2, 0.4, 0.8, 1, 1.2, 1.4, 1.6,1.8, 2, 2.4, 3, 3.2, 3.6, 3.8,4, 6.6, 8.6, 9.2, 10.2, 11.2, 11.6, 12	100 per cent
Field Case 2	Frequencies: 0.2 0.4, 0.8, 1.2, 2, 3, 4, 6.6, 9.2, 10.2, 12	≈ 47 per cent

be resolved if a high-quality resistivity model is available. For a synthetic data case, where the earth model is well known, receiver sensitivity studies can be performed in advance. However, in case of field data, this cannot always be ensured. In this investigation, we have studied both field data and synthetic data associated with the Wisting oil field. Comparing the inversions of the synthetic and field data demonstrates clear similarities as well as discrepancies. For both data types, Receiver 4 stands out for its overall low Data Importance. However, it does not distinguish itself as clearly in the case of field data. Thus, the removal of this receiver might result in an unacceptable decrease in resolving power. The differences observed between the synthetic and field inversions might be due to the fact that the latter represents a 3-D earth response inverted using a 2.5-D inversion algorithm.

Another challenge regarding improvements to survey design in a production setting relates to corresponding changes in the reservoir. During production, resistivity is expected to decrease. This phenomenon might again introduce changes in the sensitivity of the different receiver locations. Shantsev *et al.* (2020) address this concern and demonstrate that time-lapse effects due to production are preserved in the inverted domain even in cases with major differences in survey layout between base and monitor data. Nonetheless, a detailed study of such effects with emphasis on the resolution matrices would be of value.

It is possible to significantly subsample the data along the frequency direction without losing essential resolving power. However, such selections should be guided by using ratio of resolution maps. Moreover, it seems that the best results are obtained by retaining the highest- and lowest-frequency components and then more sparsely filling in key frequencies between these two endpoints. Key (2009) made the same observation with regard to frequency sampling in 1-D CSEM inversion. However, while (Key 2009) emphasized that this observation might not hold in higher dimensions, our observations substantiate that this claim at least holds some merit in two dimensions.

8 CONCLUSION

The purpose of this work is to introduce and investigate the use of the resolution matrices in CSEM inversion and evaluate how such information can be used for data decimation and survey design in the case of a repeated survey. Proper testing of our proposed strategy required the construction of a high-quality resistivity model using well logs, seismic and CSEM data from the Wisting oil field in the southwestern Barents Sea. The MARE2DEM forward modelling and inversion package was used as a starting point for this study. We suggested a new metric, denoted ratio of resolution, to better evaluate the resolving power of a given data set. We also introduced a detailed framework to describe how resolution matrices can be used for both survey design and data decimation. Finally, we demonstrated the proposed approach on both synthetic and field data sets.

Our results show that the resolution matrices carry important information that can be used for more efficient data decimation and survey design. It is likely that significant data redundancy may exist in the acquisition of a full CSEM survey. Thus, utilizing the information carried by the resolution matrices allows the original data set to be downsampled without losing essential resolving power.

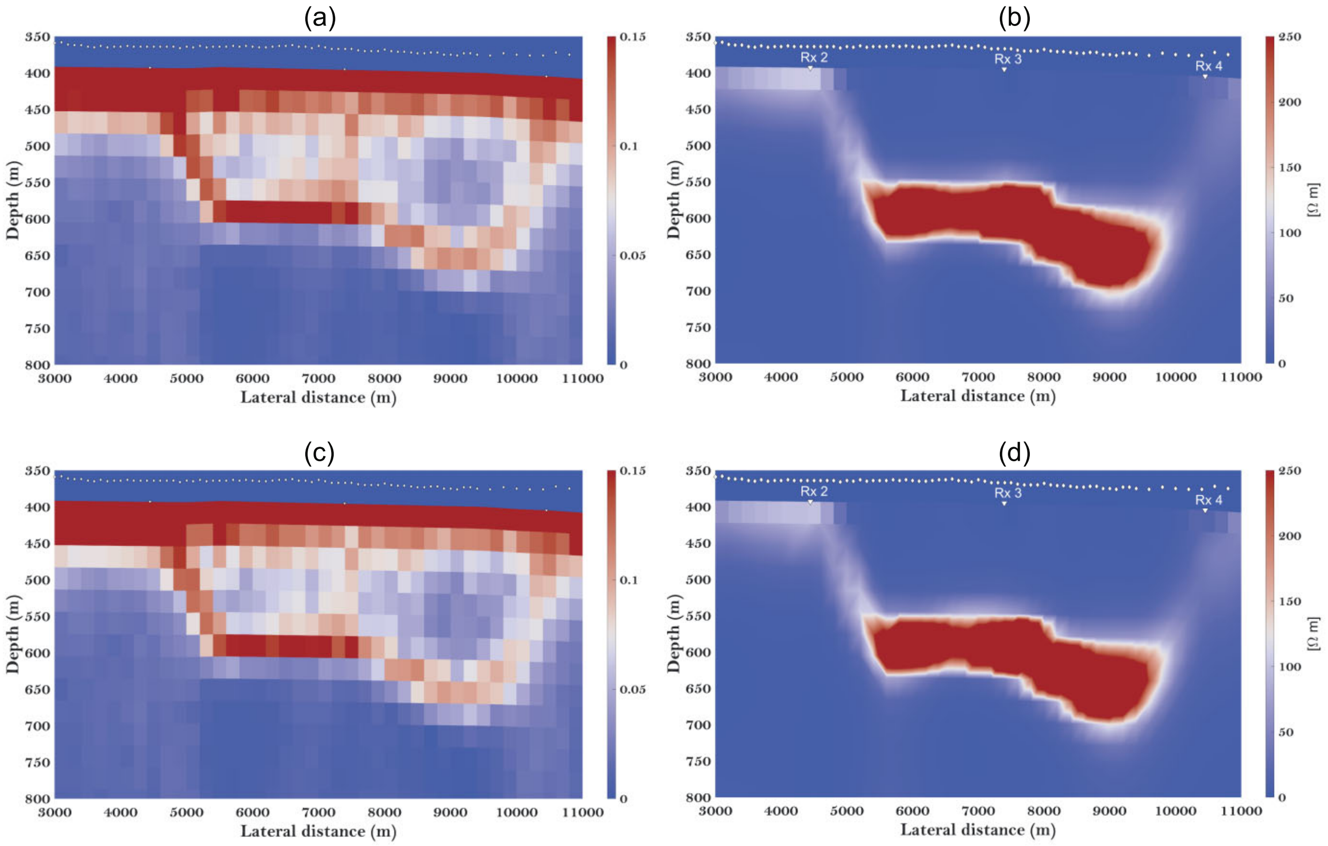

Figure 14. Ratio of resolution for Field Case 1 and 2 (a, c) and corresponding inverted models (b, d).

ACKNOWLEDGMENTS

This work has been funded by the Research Centre for Arctic Petroleum Exploration (ARCEx) and the Norwegian Research Council (project number 228107). The authors acknowledge EMGS ASA for providing the field data and Dr Kerry Key for making the MARE2DEM package publicly available. In addition, we would like to extend our gratitude to Dr Torgeir Wiik for fruitful discussions and help during this project.

DATA AVAILABILITY

The data underlying this paper were provided by EMGS ASA under license. The data will be shared on a reasonable request to the corresponding author subject to permission from EMGS ASA.

REFERENCES

Brown, V., Hoversten, M., Key, K. & Chen, J., 2012. Resolution of reservoir scale electrical anisotropy from marine CSEM data, *Geophysics,* **77**(2), E147–E158.

Carvalho, B.R. & Menezes, P. T.L., 2017. Marlim R3D: a realistic model for CSEM simulations-phase I: model building, *Braz. J. Geol.,* **47,** 633–644.

Constable, S., 2010. Ten years of marine CSEM for hydrocarbon exploration, *Geophysics,* **75**(5), 75A67–75A81.

Constable, S., Parker, R.L. & Constable, C.G., 1987. Occam's inversion: a practical algorithm for generating smooth models from electromagnetic sounding data, *Geophysics,* **52**(3), 289–300.

Constable, S., Kannberg, P.K. & Weitemeyer, K., 2016. Vulcan: a deep-towed CSEM receiver, *Geochem. Geophys. Geosyst.,* **17**(3), 1042–1064.

Correa, J.L. & Menezes, P.T., 2019. Marlim R3D: a realistic model for controlled-source electromagnetic simulations—Phase 2: the controlled-source electromagnetic data set, *Geophysics,* **84**(5), E293–E299.

Engelmark, F., Mattsson, J., McKay, A. & Du, Z., 2014. Towed streamer EM comes of age, *First Break,* **32**(4), doi:10.3997/1365-2397.32.4.74381.

Friedel, S., 2003. Resolution, stability and efficiency of resistivity tomography estimated from a generalized inverse approach, *Geophys. J. Int.,* **153**(2), 305–316.

Granli, J.R., Veire, H.H., Gabrielsen, P. & Morten, J.P., 2017. Maturing broadband 3D CSEM for improved reservoir property prediction in the Realgrunnen Group at Wisting, Barents Sea, in *Proceedings of the 2017 SEG International Exposition and Annual Meeting,* OnePetro.

Grayver, A.V., Streich, R. & Ritter, O., 2014. 3D inversion and resolution analysis of land-based CSEM data from the Ketzin CO_2 storage formation, *Geophysics,* **79**(2), E101–E114.

Hansen, P.C., Nagy, J.G. & O'Leary, D.P., 2006. *Deblurring Images: Matrices, Spectra, and Filtering,* SIAM.

Hoversten, G.M., Røsten, T., Hokstad, K., Alumbaugh, D., Horne, S. & Newman, G.A., 2006. Integration of multiple electromagnetic imaging and inversion techniques for prospect evaluation, in *Proceedings of the SEG Technical Program Expanded Abstracts 2006,* pp. 719–723, Society of Exploration Geophysicists.

Jakobsen, M. & Tveit, S., 2018. Distorted Born iterative T-matrix method for inversion of CSEM data in anisotropic media, *Geophys. J. Int.,* **214**(3), 1524–1537.

Kalscheuer, T., De los Ángeles García Juanatey, M., Meqbel, N. & Pedersen, L.B., 2010. Non-linear model error and resolution properties from two-dimensional single and joint inversions of direct current resistivity and radiomagnetotelluric data, *Geophys. J. Int.,* **182**(3), 1174–1188.

Key, K., 2009. 1D inversion of multicomponent, multifrequency marine CSEM data: methodology and synthetic studies for resolving thin resistive layers, *Geophysics,* **74**(2), F9–F20.

Key, K., 2016. MARE2DEM: a 2-D inversion code for controlled-source electromagnetic and magnetotelluric data, *Geophys. J. Int.,* **207**(1), 571–588.

Li, G., Li, Y., Han, B. & Liu, Z., 2018. Application of the perfectly matched layer in 3-D marine controlled-source electromagnetic modelling, *Geophys. J. Int.,* **212**(1), 333–344.

Lu, X. & Xia, C., 2007. Understanding anisotropy in marine CSEM data, in *Proceedings of the 2007 SEG Annual Meeting,* OnePetro.

Masnaghetti, L. & Ceci, F., 2010. Analysis of the sensitivity to anisotropy of CSEM data using 2.5 D modeling and inversion, in *Proceedings of the SEG Technical Program Expanded Abstracts 2010,* pp. 614–618, Society of Exploration Geophysicists.

Mattsson, J., 2015. Resolution and precision of resistivity models from inversion of towed streamer EM data, in *Proceedings of the 2015 SEG Annual Meeting,* OnePetro.

Maurer, H., Boerner, D.E. & Curtis, A., 2000. Design strategies for electromagnetic geophysical surveys, *Inverse Problems,* **16**(5), doi:10.1088/0266-5611/16/5/302.

McKay, A., Mattsson, J. & Du, Z., 2015. Towed streamer EM-reliable recovery of sub-surface resistivity, *First Break,* **33**(4), doi:10.3997/1365-2397.33.4.79748.

Menke, W., 2012. *GeophySical Data Analysis: Discrete Inverse Theory,* MATLAB edition, Vol. **45,** Academic Press.

Newman, G.A., Commer, M. & Carazzone, J.J., 2010. Imaging CSEM data in the presence of electrical anisotropy, *Geophysics,* **75**(2), F51–F61.

Parasnis, D., 1988. Reciprocity theorems in geoelectric and geoelectromagnetic work, *Geoexploration,* **25**(3), 177–198.

Ren, Z. & Kalscheuer, T., 2020. Uncertainty and resolution analysis of 2D and 3D inversion models computed from geophysical electromagnetic data, *Surv. Geophys.,* **41**(1), 47–112.

Romdhane, A. & Eliasson, P., 2018. Optimised geophysical survey design for CO$_2$ monitoring—a synthetic study, in *Proceedings of the 14th Greenhouse Gas Control Technologies Conference,* Melbourne, pp. 21–26.

Rossmann, K., 1969. Point spread-function, line spread-function, and modulation transfer function: tools for the study of imaging systems, *Radiology,* **93**(2), 257–272.

Roux, E. & García, X., 2014. Optimizing an experimental design for a CSEM experiment: methodology and synthetic tests, *Geophys. J. Int.,* **197**(1), 135–148.

Schlumberger, 2018. *Petrel 20 years book,* https://www.software.slb.com/-/media/software-media-items/software/documents/external/product-sheets/petrel-20-years-book.pdf, Accessed: 14-02-2022.

Senger, K., Birchall, T., Betlem, P., Ogata, K., Ohm, S., Olaussen, S. & Paulsen, R.S., 2021. Resistivity of reservoir sandstones and organic rich shales on the Barents Shelf: Implications for interpreting CSEM data, *Geosci. Front.,* **12**(6), doi:10.1016/j.gsf.2020.08.007.

Shantsev, D.V., Nerland, E.A. & Gelius, L.-J., 2020. Time-lapse CSEM: how important is survey repeatability?, *Geophys. J. Int.,* **223**(3), 2133–2147.

Stefani, J., Frenkel, M., Bundalo, N., Day, R. & Fehler, M., 2010. SEAM update: models for EM and gravity simulations, *Leading Edge,* **29**(2), 132–135.

Wang, F., Morten, J.P. & Spitzer, K., 2018. Anisotropic three-dimensional inversion of CSEM data using finite-element techniques on unstructured grids, *Geophys. J. Int.,* **213**(2), 1056–1072.

Weitemeyer, K., Gao, G., Constable, S. & Alumbaugh, D., 2010. The practical application of 2D inversion to marine controlled-source electromagnetic data, *Geophysics,* **75**(6), F199–F211.

Wheelock, B., Constable, S. & Key, K., 2015. The advantages of logarithmically scaled data for electromagnetic inversion, *Geophys. J. Int.,* **201**(3), 1765–1780.

Zhdanov, M.S., 2010. Electromagnetic geophysics: notes from the past and the road ahead, *Geophysics,* **75**(5), 75A49–75A66.

APPENDIX A: SENSITIVITY CALCULATIONS AND TRANSFORMATION TO COMPLEX FIELDS

In order to extract the resistivity model from observed data, iterative inversion schemes are used. In deterministic inversion, the partial derivatives with respect to model parameters form a crucial part of the inversion scheme. These partial derivatives are often denoted sensitivities and together makes up the Jacobian matrix. We start by defining sensitivity as introduced in Key (2016). Let σ_j represent an arbitrary conductivity parameter in our earth model. The sensitivity of one datapoint (i.e. one unique source, receiver and frequency combination) with respect to this model parameter can now be calculated as:

$$\frac{\partial F}{\partial \sigma_j}(x, y, z) = \frac{1}{2\pi}\int_{-\infty}^{\infty} \hat{s}_j(k_x, y, z)e^{ik_x(x_r - x_s)}\mathrm{d}k_x, \tag{A1}$$

where $\hat{s_j}(k_x, y, z)$ is given by

$$\hat{s}_j(k_x, y, z) = \int_{A_j} \hat{\mathbf{E}}^{\mathbf{a}}(-k_x, y, z)\left(\frac{\partial \bar{\bar{\sigma}}}{\partial \sigma_j}\hat{\mathbf{E}}(k_x, y, z)\right)\mathrm{d}A_j. \tag{A2}$$

$\mathbf{E}$ and $\mathbf{E}^{\mathbf{a}}$ denote, respectively, the electric field and adjoint electric field in the wavenumber domain. The adjoint field is created by turning the corresponding receiver into an adjoint source. In eqs (A1) and (A2), A_j denotes the area of the cell containing conductivity parameter σ_j, while x_r and x_s describe the along strike position of the receivers and sources. The entries of the Jacobian matrix related to this unique datapoint can now be written as

$$J_j = \frac{\partial F[\mathbf{m}]}{\partial m_j} = \frac{\ln(10)}{\rho_j}\frac{\partial F[\mathbf{m}]}{\partial \sigma_j} = \frac{\partial F[\mathbf{m}]}{\partial \log(\rho_j)} = \frac{\partial \mathbf{d}}{\partial \log(\rho_j)}. \tag{A3}$$

Eq. (A3) takes this special form since the inversion in MARE2DEM is parametrized with respect to log transformed resistivities. Moreover, the actual sensitivity output from MARE2DEM is given separately for log amplitude and phase (in degrees). However, in order to carry out the analysis proposed in this paper, it is crucial that the entries in the Jacobian matrix represent the complex field. For one unique datapoint in the data vector $\mathbf{d}$, the complex data sample d can be formally written as

$$d = ae^{i\phi_{\text{rad}}} = a(\cos(\phi_{\text{rad}}) + i\sin(\phi_{\text{rad}})), \tag{A4}$$

where a is the amplitude and ϕ_{rad} is the phase given in radians. By taking the derivative with respect to the base 10 logarithm of the model we get

$$\begin{aligned}\frac{\partial d}{\partial \log(\rho_j)} &= \frac{\partial a}{\partial \log(\rho_j)}e^{i\phi_{\text{rad}}} + ae^{i\phi_{\text{rad}}}i\frac{\phi_{\text{rad}}}{\partial \log(\rho_j)}\\ &= d\left(\frac{1}{a}\frac{\partial a}{\partial \log(\rho_j)} + i\frac{\partial \phi_{\text{rad}}}{\partial \log(\rho_j)}\right).\end{aligned} \tag{A5}$$

The quantities inside the brackets in eq. (A5) can be computed as:

$$\frac{1}{a}\frac{\partial a}{\partial \log(\rho_j)} \approx \ln(10)\frac{\partial \log(a)}{\partial \log(\rho_j)}, \tag{A6}$$

and

$$\frac{\partial \phi_{\text{rad}}}{\partial \log(\rho_j)} = \frac{\pi}{180}\frac{\partial \phi_{\text{degree}}}{\partial \log(\rho_j)}. \tag{A7}$$

Thus, by combining eqs (A4), (A5), (A6) and (A7) we can construct the Jacobian matrix for the complex field as follows:

$$\frac{\partial d}{\partial \log(\rho_j)} \approx d\left(\ln(10)\frac{\partial \log(a)}{\partial \log(\rho_j)} + i\,\frac{\pi}{180}\,\frac{\partial \phi_{\mathrm{degree}}}{\partial \log(\rho_j)} \right), \tag{A8}$$

where $\frac{\partial \log(a)}{\partial \log(\rho_j)}$ and $\frac{\partial \phi_{\mathrm{degree}}}{\partial \log(\rho_j)}$ represent sensitivity outputs from MARE2DEM. The Jacobian entries as calculated from eq. (A8) must also be accompanied with corresponding standard errors (δ) of the measurement data. These errors form the diagonal weighting matrix $\mathbf{W_d}$ used in the expressions for the resolution matrices. For one particular datapoint, δ is computed as

$$\delta = \frac{1}{\sqrt{2}a\sigma_l}, \tag{A9}$$

where σ_l denotes the user defined noise level (i.e. 1 per cent = 0.01)

APPENDIX B: SUBSAMPLED DATA SETS

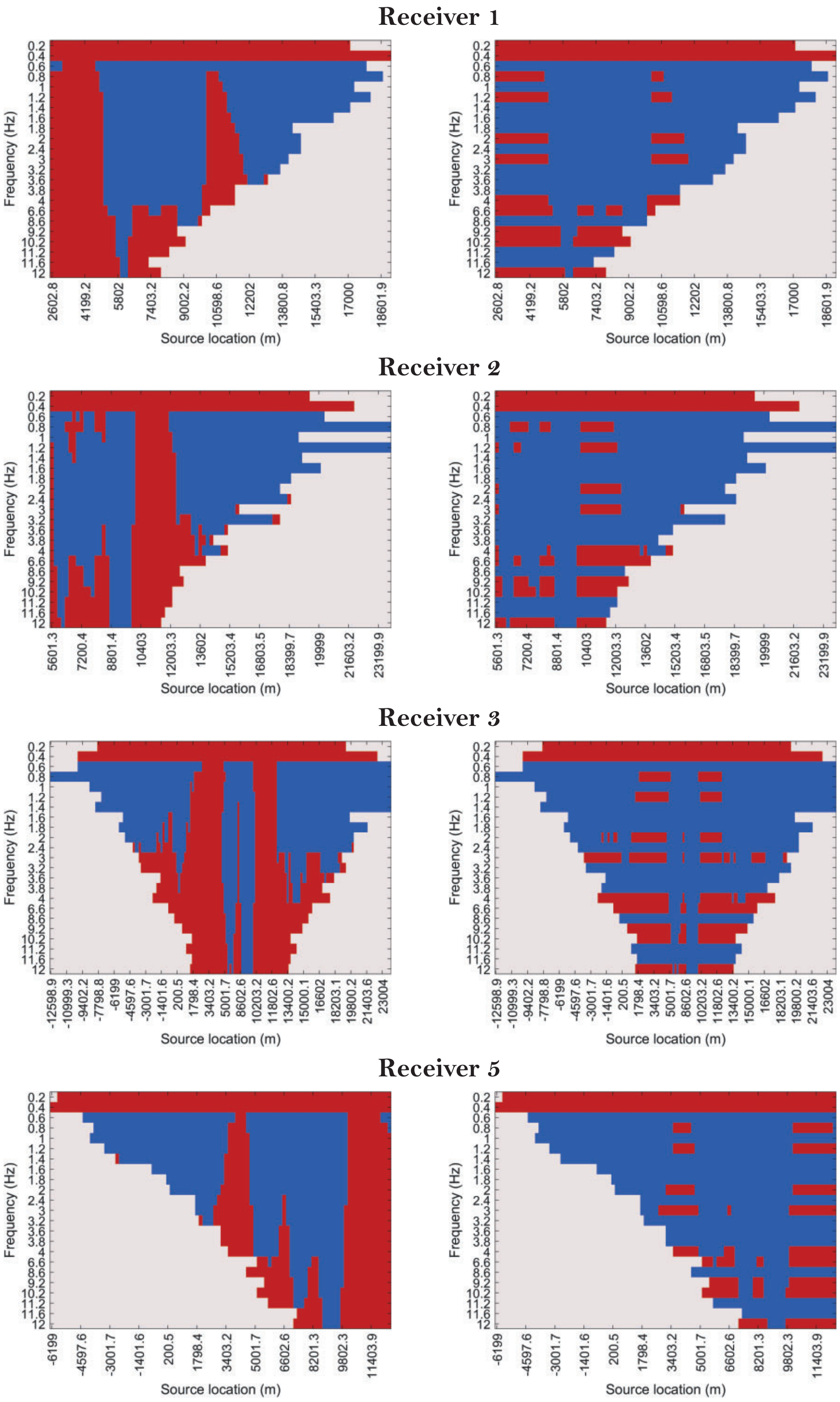

Figure B1. Data subsampling for Cases 3 (left-hand column) and 4 (right-hand column) in the main body of the text. Red indicates data input to the inversion, while blue signifies data which have been removed by the thresholding described in Section 4.5. Row 1, 2, 3 and 4 refers to receiver 1, 2, 3 and 5, respectively (Fig. 1a). Note that the data subsampling plot for Receiver 4 is omitted due to the findings in Case 2.

Paper III

Resolution enhancement of 2D CSEM images by use of PSF inversion

Vemund Stenbekk Thorkildsen, Leiv-J Gelius

Submitted for publication in *Frontiers in Earth Science*. Special issue: *Advances in Geophysical Inverse Problems.*

Resolution enhancement of 2D CSEM images by use of PSF inversion

Vemund S. Thorkildsen[1*] and **Leiv-J. Gelius**[1]

[1]Department of Geosciences, University of Oslo, Norway

*** Correspondence:**
Vemund S. Thorkildsen
vemund.s.thorkildsen@gmail.com

Keywords: controlled-source EM (CSEM), inversion, deblurring, point-spread function (PSF)

Abstract

The marine controlled-source electromagnetic (CSEM) technique is employed both in large-scale geophysical applications as well as within the exploration of hydrocarbons and gas hydrates. Because of the diffusive character of the EM field, only very low frequencies are used, leading to inversion results with low resolution. In this paper, we calculated the resolution matrix associated with the inversion and derived the corresponding point-spread functions (PSFs). The PSFs provided information about how much the actual inversion was blurred. Using a space-varying deconvolution can thus further improve the inversion result. The actual deblurring was carried out using the nonnegative flexible conjugate gradient least-squares (NN-FCGLS) algorithm, which is a fast iterative restoration technique. To attain completeness, we also introduced the results obtained using a blind deconvolution algorithm based on the maximum likelihood estimation (MLE) with unknown PSFs. The potential of the proposed approach has been demonstrated using both complex synthetic data and field data acquired at the Wisting oil field in the Barents Sea. In both cases, the resolution of the final inversion result was improved and showed greater agreement with the known target area.

1 Introduction

The marine controlled-source electromagnetic (CSEM) technique has the potential to resolve the fluid distribution in a reservoir. This method is particularly sensitive to high-resistivity fluids like hydrocarbons and has therefore proven successful within petroleum exploration (Um and Alumbaugh, 2007; Constable, 2010). Initially, CSEM data were processed directly in the data domain using normalized magnitude and phase-versus-offset plots (Ellingsrud et al., 2002; Røsten et al., 2003). During the last two decades, and in parallel with the improvement in computing power, the processing of CSEM data has moved to the model domain through inversion. Nowadays, such inversion can handle complex 2D and 3D Earth models including anisotropy (Brown et al., 2012; Wang et al., 2018; Jakobsen and Tveit, 2018). However, the CSEM technique has a low resolution because low frequencies (typically in the range of 0.25–10 Hz) are used to achieve the desired penetration depths because of the characteristics of the diffusive wave. Thus, the actual inversion represents a blurred version of the true target. In addition, data noise, bias, and inappropriate a priori geological information may lead to further uncertainties in the final inversion result.

The use of sophisticated inversion techniques like the Gauss-Newton method (Key, 2016; Nguyen et al., 2016; Bjørke et al., 2020) may (partly) correct for resolution losses by including the approximate Hessian matrix. In this study, we proposed the use of point-spread functions (PSFs) to quantify the remaining deblurring after a Gauss-Newton inversion. Such functions can be extracted from the model resolution matrix (Jackson, 1972; Menke, 2012). Several examples of the use of resolution matrices to analyze various inversion problems can be found in the literature (Alumbaugh and Newman, 2000; Friedel, 2003; Routh and Miller, 2006; Kalscheuer et al., 2010; Fichtner and Leeuwen, 2015; Chrapkiewicz et al., 2020; Ren and Kalscheuer, 2020). A few publications have also briefly discussed applications of the model resolution matrix within CSEM inversion but with limited demonstrations (Grayver et al., 2014; Mckay et al., 2015; Mattsson, 2015). In a recent publication, Thorkildsen and Gelius (2023) introduced for the first time the rigorous use of resolution matrices within CSEM and demonstrated how the associated PSFs can be employed to quantify the resolution power and as an aid in survey planning.

By analogy with work carried out earlier regarding seismic data imaging and inversion (Hu et al., 2001; Sjoeberg et al., 2003; Yu et al., 2006; Takahata et al., 2013; Yang et al., 2022) and astrophysics (Xu et al., 2020), we proposed using the PSFs extracted from a regularized Gauss-Newton inversion of marine CSEM data to further deblur the inversion result in a post-processing step. The actual deblurring was carried out using the nonnegative flexible conjugate gradient least-squares (NN-FCGLS) algorithm (Gazzola et al., 2017). The feasibility of the proposed approach was demonstrated using both complex synthetic data as well as field data from the Wisting oil field in the Barents Sea.

2 General framework of the 2D CSEM inversion

2.1 MARE2DEM package

CSEM inversion was performed using the open-source inversion package MARE2DEM (Modeling with Adaptively Refined Elements 2D EM) (Key, 2016). This package was developed for 2D anisotropic modeling and inversion of both offshore and onshore CSEM and magnetotelluric (MT) data. MARE2DEM is based on the Occam approach (Constable et al., 1987), which is a variant of Gauss-Newton minimization. The starting point of the inversion scheme is a nonlinear problem formulation, which is solved iteratively by minimizing a cost function (Key, 2016; Ren and Kalscheuer, 2020)

$$\phi[\mathbf{m},\alpha]=\left[\left(\mathbf{d}-F[\mathbf{m}]\right)^{\dagger}\mathbf{W}_d^{\dagger}\mathbf{W}_d\left(\mathbf{d}-F[\mathbf{m}]\right)\right]+\alpha\mathbf{m}^{\dagger}\mathbf{W}_m^{\dagger}\mathbf{W}_m\mathbf{m}, \qquad (1)$$

where $\mathbf{d}$ of size $i = 1,2,\ldots N$ is the measured complex field data (i.e., frequency domain), $F[\mathbf{m}]$ is the corresponding model response, $\mathbf{W}_d$ is the weighting matrix for the data misfit, α is the Langrangian weight factor for the regularization term, and $\mathbf{W}_m$ is the regularization matrix. While dealing with complex fields, the Hermitian $\dagger$ (i.e., matrix transpose and complex conjugation) notation should be adopted for the matrices involved. In MARE2DEM, $\mathbf{W}_d$ is the diagonal matrix composed of the inverse of the standard error δ for each sample and $\mathbf{W}_m$ is the weighting matrix that forces smoothness on the model. The latter is obtained by use of a gradient roughness operator. In the case of anisotropic Earth models, the roughness is implemented by partitioning the model vector into anisotropic subsets (Key, 2016). In MARE2DEM, the model parameter m represents the logarithm of resistivity $\log(\rho)$ (bounded to a user-defined interval).

In practice and due to the nonlinearity of the inverse problem, the forward (modeling) operator F in Equation (1) is quasi-linearized using a Taylor series expansion. This leads to an iterative formulation where the $(k+1)^{th}$ update is given as

$$\begin{aligned}\phi_{lin}\left[\mathbf{m}_{k+1},\alpha\right] = &\left[\left(\mathbf{d}-F\left[\mathbf{m}_k\right]-\mathbf{J}\left(\mathbf{m}_{k+1}-\mathbf{m}_k\right)\right)^{\dagger}\mathbf{W}_d^{\dagger}\mathbf{W}_d\left(\mathbf{d}-F\left[\mathbf{m}_k\right]-\mathbf{J}\left(\mathbf{m}_{k+1}-\mathbf{m}_k\right)\right)\right]\\ &+\alpha\mathbf{m}_{k+1}^{\dagger}\mathbf{W}_m^{\dagger}\mathbf{W}_m\mathbf{m}_{k+1}\ ,\end{aligned} \qquad (2)$$

where $\mathbf{J}$ is the model Jacobian matrix with entries $\partial F_i(\mathbf{m}_k)/\partial m_j$. Finally, after differentiating the cost function (2) with respect to the current model and setting $\partial\phi_{lin}\left[\mathbf{m}_{k+1},\alpha\right]/\partial\mathbf{m}_{k+1}=0$, a least-squares solution is obtained after rearrangement:

$$\mathbf{m}_{k+1}=\mathbf{J}_w^{-g}\mathbf{W}_d\mathbf{d}_k\ , \qquad (3)$$

with $\mathbf{d}_k=\left[\mathbf{d}-F\left[\mathbf{m}_k\right]+\mathbf{J}\mathbf{m}_k\right]$ being the modified data vector and $\mathbf{J}_w^{-g}$ being the generalized inverse matrix defined as $\left[\mathbf{J}^{\dagger}\mathbf{W}_d^{\dagger}\mathbf{W}_d\mathbf{J}+\alpha\mathbf{W}_m^{\dagger}\mathbf{W}_m\right]^{-1}\mathbf{J}^{\dagger}\mathbf{W}_d^{\dagger}$.

In MARE2DEM, Equation (3) is solved iteratively by applying the Occam approach. This implies that the Langrangian multiplier α is optimized as part of the inversion. For more details, the reader is referred to Key (2016) and Constable et al. (1987).

In general, for an EM problem, there is a total of six different data components, which correspond to the three different directions of the magnetic and electric fields. However, in this study, we only used the embedded inline horizontal electric field (Ey), which is the most important component for marine CSEM.

2.2 Resolution matrix

If we assume a noise-free case and that the true model has been obtained from the inversion, the modified data vector can be written as

$$\mathbf{d}_k=\mathbf{d}_{true}=\mathbf{J}\mathbf{m}_{true}\ . \qquad (4)$$

The combination of Equations (3) and (4) gives then

$$\mathbf{m}_{k+1}=\mathbf{R}_M\mathbf{m}_{true}\ , \qquad (5)$$

with $\mathbf{R}_M$ being the resolution matrix, which can be written explicitly as (Ren and Kalscheuer, 2020)

$$\mathbf{R}_M=\Re\left\{\left[\mathbf{J}^{\dagger}\mathbf{W}_d^{\dagger}\mathbf{W}_d\mathbf{J}+\alpha\mathbf{W}_m^{\dagger}\mathbf{W}_m\right]^{-1}\mathbf{J}^{\dagger}\mathbf{W}_d^{\dagger}\mathbf{W}_d\mathbf{J}\right\}, \qquad (6)$$

and where $\Re$ implies taking the real part.

In a practical inversion case $\mathbf{m}_{true}$ is unobtainable. The model resolution matrix reveals how close the preferred inversion model is to the true model, which relies on the Lagrangian multiplier α. By letting α → 0, the model resolution matrix approximates the unity matrix. In this case, the inverse problem is perfectly solved if there is no noise. As a pragmatic approach, we assume that $\mathbf{m}_{k+1}$ represents the preferred inversion model if the inversion is terminated after iteration number *k*.

The resolution matrix is *not calculated* as part of the output from MARE2DEM. We have therefore developed an extension to the inversion package where this quantity is computed.

To gain further insight, we consider *a 1D case* first and decompose the corresponding resolution matrix into its column vectors:

$$\mathbf{R}_M = \left[\mathbf{r}_1 .....\mathbf{r}_j ....\mathbf{r}_M\right], \tag{7}$$

where $\mathbf{r}_j$ is the j^{th} column vector ($j = 1, 2, ...M$) and M represents the total number of 1D image points. Each column vector in Equation (7) represents now a point-spread function (PSF) associated with a corresponding fixed image point (cf. Figure 1a). The concept of a PSF is well known from imaging theory (Rossmann, 1969) and describes how much a point or pixel in an image (i.e., a model parameter) is blurred due to the imaging system (i.e., inversion in our case). A 2D image, as considered in this paper, is represented by a lexicographical ordering as illustrated in Figure 2. The resolution (blur) matrix then takes a more complex form as discussed in Section 3.2 (cf. Equation (9)). A perfectly resolved case exhibits a PSF with the value of 1 at the location of the image point and 0 elsewhere. Figures 1b and 1c show examples of a well-resolved and a poorly resolved case, respectively, for a 2D image. The PSF in Figure 1b is characterized by a small spread centered on the corresponding model parameter. However, in Figure 1c, the PSF is characterized by a large spread.

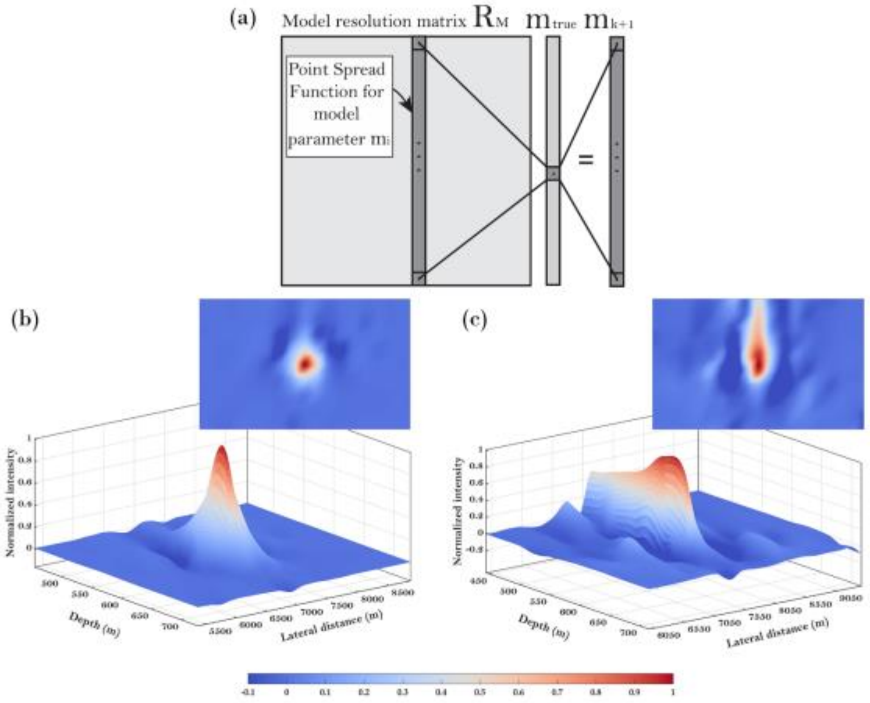

Figure 1*: (a) The relationship between the true model* $\mathbf{m}_{true}$ *and the preferred inversion model* $\mathbf{m}_{k+1}$ *expressed by the PSF (1D case). (b) and (c) are examples of PSF for a well-resolved and poorly resolved 2D case, respectively. Both PSFs have been normalized to 1 for presentation purposes.*

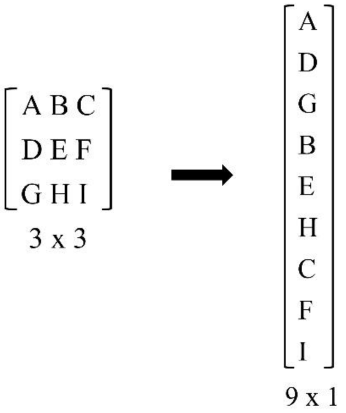

***Figure 2**: Lexicographical ordering of the 2D image (the letters indicate pixels).*

3 General framework of deblurring

3.1 Forward (blur) model

From now on, we will use the notation **A** for the resolution matrix corresponding to a lexicographic ordering of the 2D image or model. The following general relationship between the true image $\mathbf{m}$ and its blurred counterpart $\mathbf{b}$ (i.e., the output from the CSEM inversion) holds (*forward* model)

$$\mathbf{Am} = \mathbf{b} + \mathbf{n}, \tag{8}$$

where $\mathbf{A}$ is the blurring (resolution) matrix and $\mathbf{n}$ represents an additive noise term. Since $\mathbf{m}$ (and $\mathbf{b}$) is organized in lexicographical order (cf. Figure 2), the structure of the blur matrix takes a special form as discussed in the next section.

3.2 Blur matrix and a space-invariant PSF

We start by considering the case of a *space-invariant* PSF. Assume that the number of image points is $M = 2N + 1$ along each direction (and with indices running from $-N$ to N). Assume also that the PSF has the same size as the image (cf. upper part of Figure 3). The first step in forming the blur matrix $\mathbf{A}$ is to organize each row of the PSF in a Toeplitz matrix as shown in the lower part of Figure 3 for row n.

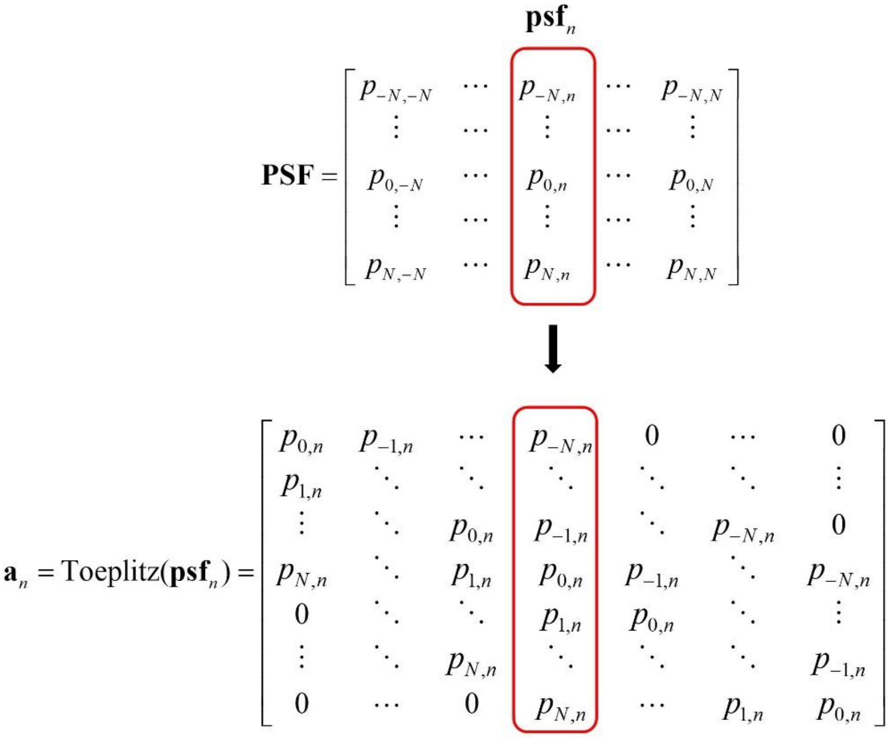

Figure 3*: First step in forming the blur matrix* $\mathbf{A}$*: each column in the space-invariant PSF (upper part of the figure) is reorganized in a Toeplitz matrix as shown in the lower part of the figure.*

The blur matrix $\mathbf{A}$ can now be constructed as a block Toeplitz matrix with Toeplitz blocks (BTTB) with zero boundary conditions (Hansen et al., 2006) and where each block element $\mathbf{a}_n \ (n = -N, \ldots\ldots -1, 0, 1 \ldots\ldots N)$ is defined in Figure 3:

$$\mathbf{A} = \begin{bmatrix} \mathbf{a}_0 & \mathbf{a}_{-1} & \cdots & \mathbf{a}_{-N} & 0 & \cdots & 0 \\ \mathbf{a}_1 & \ddots & \ddots & \ddots & \ddots & \ddots & \vdots \\ \vdots & \ddots & \mathbf{a}_0 & \mathbf{a}_{-1} & \ddots & \mathbf{a}_{-N} & 0 \\ \mathbf{a}_N & \ddots & \mathbf{a}_1 & \mathbf{a}_0 & \mathbf{a}_{-1} & \ddots & \mathbf{a}_{-N} \\ 0 & \ddots & \ddots & \mathbf{a}_1 & \mathbf{a}_0 & \ddots & \vdots \\ \vdots & \ddots & \mathbf{a}_N & \ddots & \ddots & \ddots & \mathbf{a}_{-1} \\ 0 & \cdots & 0 & \mathbf{a}_N & \cdots & \mathbf{a}_1 & \mathbf{a}_0 \end{bmatrix}. \tag{9}$$

The blur matrix **A** has dimensions $M^2 x M^2$ where $M = 2N + 1$.

3.3 Generalization to space-variant PSF (image segmentation)

To discuss a more general case characterized by space-variant PSFs, a pragmatic approach would be to subdivide the model space into space-invariant regions and perform deblurring separately for each region. This implies that each region is assigned a deblur matrix of the form given by Equation (9), but with its own representative PSF. The final image is then constructed by combining the space-invariant regions after deblurring (and with possibly some smoothing applied to avoid edge effects). A more attractive approach, however, is to construct a space-variant **A** matrix (Nagy and O’Leary, 1997). Let Figure 4 (left portion) represent an idealized case where the model space is subdivided into two regions, each of them characterized by distinct and different PSFs. To minimize edge effects, a transition zone, which defines a gradual transition between the two PSFs, has also been introduced. Figure 4 (right portion) shows the corresponding lexicographical ordering of the model parameters including the transition zone (by analogy with Figure 2).

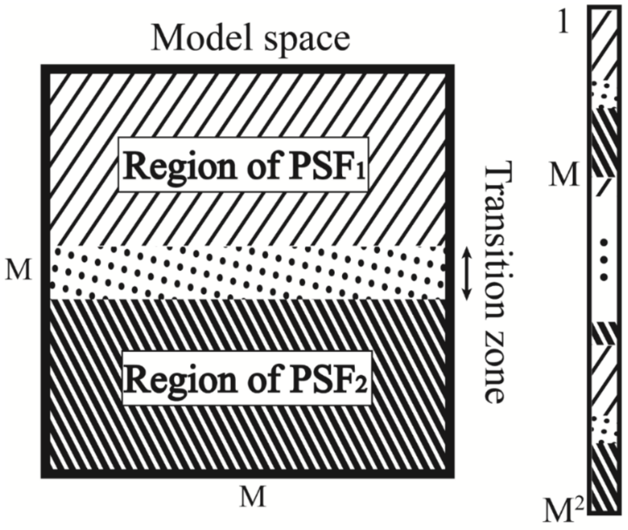

__Figure 4__: (Left) Idealized model space subdivided into two regions including a transition zone; (right) lexicographic representation of the same model space with a transition zone.

Before constructing the *space-variant* blur matrix **A,** we need to define a corresponding space-invariant blur matrix for each subregion (same form as in Equation (9)). In the idealized case shown in Figure 4, two blur matrices ($\mathbf{A}_1$ and $\mathbf{A}_2$) need therefore to be constructed. In this demonstration example, we have defined the two PSFs as simple 2D Gaussian functions with different degrees of blurring. More specifically, we chose the PSF of region 1 to introduce less blurring than the corresponding PSF of region 2. This implies that the blur matrix $\mathbf{A}_1$ has a more narrow band of values concentrated along its diagonal compared to the blur matrix $\mathbf{A}_2$ (cf. upper row in Figure 5).

The next step is to calculate a weighting matrix for each of the two regions in Figure 4 ($\mathbf{D}_1$ and $\mathbf{D}_2$). To avoid edge effects, the PSF should vary smoothly between different subregions. This can be achieved by applying linear tapering between neighboring subregions. In such a transition zone, an effective PSF is constructed as the linear combination between the two neighboring PSFs. The two weighting matrices for the idealized case in Figure 4 are shown in the middle row of Figure 5. A zoomed version of a section of the weight matrix $\mathbf{D}_2$ is also included to better visualize the smooth transition between the two subregions (i.e., no sharp edges). The final blur matrix **A** can then be constructed as the sum of the Hadamard product of the two space-invariant matrices and the associated weighting matrices

$$\mathbf{A} = \mathbf{A}_1 \odot \mathbf{D}_1 + \mathbf{A}_2 \odot \mathbf{D}_2 \quad , \tag{10}$$

where the effective blur matrix **A** is shown in the bottom row of Figure 5. A zoomed version of a section of this matrix is also shown to better illustrate the effect of the smooth transition zone introduced between the two subregions in Figure 4.

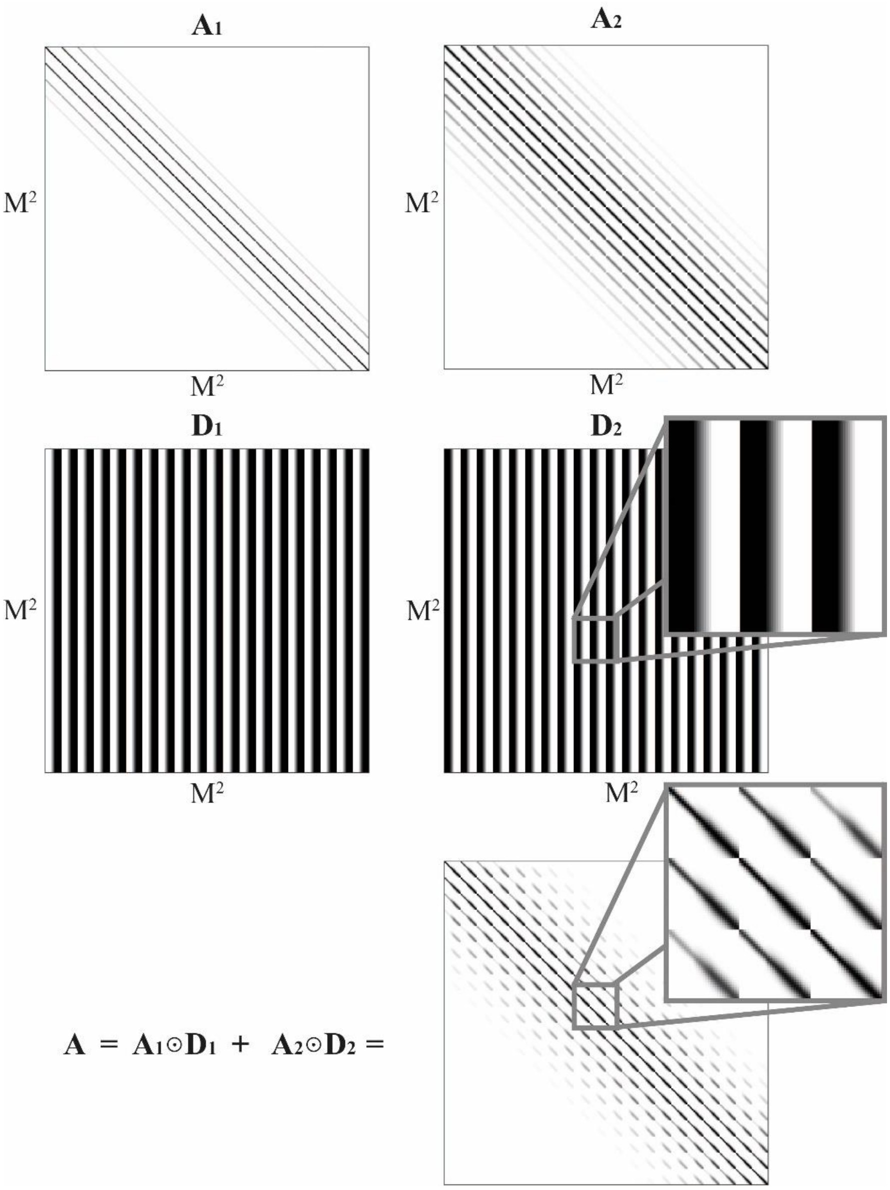

***Figure 5**: (Top row) Two space-invariant **A**-matrices corresponding to a well-resolved ($\boldsymbol{A_1}$) and smeared ($\boldsymbol{A_2}$) PSF. (Middle row) weighting matrices ($\boldsymbol{D_1}$ and $\boldsymbol{D_2}$). (Bottom row) the space-variant **A**-matrix is calculated as the sum of the Hadamard product of the two space-invariant blur matrices and the associated weighting matrices.*

As the inversion can be sensitive to input parameters (e.g., the choice of PSFs and sizes of the transition zones), developing an interactive user interface to assist in the selection of the optimized parameters is crucial. Figure 6 shows the typical plot output from this user interface (i.e., the blurred model output from the CSEM inversion along with three selected PSFs). In an interactive system, a PSF plot (Figures 6b-d) automatically updates when clicking on the corresponding cell location in the blurred model (green dots in Figure 6a). This allows users to interactively evaluate whether a given PSF is suitable, and the user can then add this PSF to a list. After selecting the optimal PSFs, the user can define boundaries and the size of the transition zones (cf. Figure 5). This set of parametric choices is then used to construct the space-variant **A** -matrix. This blur matrix **A** is stored in the memory of the user interface, allowing the user to efficiently test different sets of input parameters.

Nevertheless, the inversion is sensitive to the choice of PSFs. In the example shown in Figure 6, one of the PSFs corresponds to a poorly resolved model parameter (Figure 6b), whereas the PSFs in Figures 6c and 6d both describe a fairly well-resolved model parameter. These observations stress the important role our interactive user interface plays in controlling the quality of the selected parameters. The choice of an anomalous PSF (Figure 6b) can thus be easily avoided. In general, PSFs located (well) outside the target area should not be employed. Relevant PSFs are those near and inside the target area or structure. The PSFs in Figures 6c and 6d are examples of proper selections. It is well known that the output from a CSEM inversion is poorly resolved along the vertical direction. If the two PSFs in Figures 6c and 6d are used to construct the blur matrix, the corresponding deblurred image is expected to show improved vertical resolution. For a practical application, each PSF is delimited to a smaller area with tapering and normalization that ensures that the sum of its values inside the tapered area *adds to 1.*

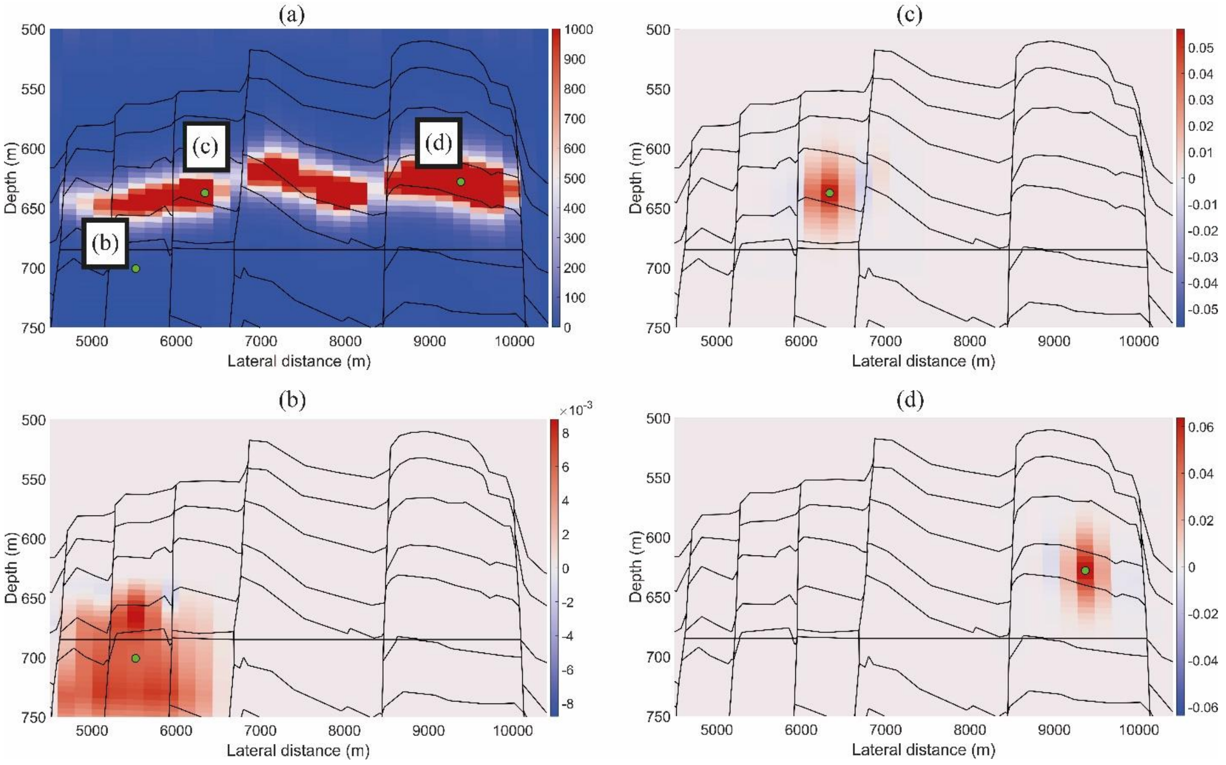

Figure 6*: (a) Example of superimposed green dots in a blurred model, indicating the location of each of the PSFs shown in (b)-(d).*

3.4 Deblurring the CSEM inversion using NN-FCGLS

In this Section, we discuss how to deblur the output from the CSEM inversion. This step represents a new inversion problem to be solved, namely the one with a forward model given by Equation (8). Several solution alternatives exist, and in this study, we used the nonnegative flexible conjugate gradient least-squares (NN-FCGLS) algorithm (Gazzola et al., 2017), which is implemented as an inner-outer scheme. The updated model of the inner iteration can be written as

$$\mathbf{m}_{k+1} = \mathbf{m}_k + \alpha_k \mathbf{p}_k \ , \tag{11}$$

where α_k is a *bounded* step size and $\mathbf{p}_k$ is a vector of direction. To fulfill the condition of nonnegativity in the solution space, the step size α_k is reduced so that $\mathbf{m}_{k+1} \ge 0 \ \ if \quad \mathbf{m}_k > 0$. In NN-FCGLS, this is accomplished using a bounded step size calculated with the following expression:

$$\begin{aligned} &\bar{\alpha}_k = \alpha_k \quad if \quad \mathbf{p}_k \ge 0 \\ &otherwise \quad \bar{\alpha}_k = \min\left\{ \alpha_k, \min_{j\in K} -\left(\mathbf{m}_k\right)_j / \left(\mathbf{p}_k\right)_j \right\} \quad , \end{aligned} \tag{12}$$

where *K* is a set of indices *j* such that $\left(\mathbf{p}_k\right)_j < 0$ and the direction $\mathbf{p}_k$ is obtained by a linear combination of at most κ_k previously computed $\mathbf{p}_j$ with j varying in { max{0, $k - \kappa_k$}, . . . , $k - 1$ }. If the maximum number of iterations k_{max} is assigned to the inner cycle, the choice $\kappa_k = k_{max}$ corresponds to a full recursion, while a lower κ_k corresponds to a truncated recursion and with $\kappa_k = 1$, only the last computed vector $\mathbf{p}_{k-1}$ is used. The outer cycle relies on suitable restarts to avoid stagnation. For further details about the algorithm, the reader is referred to Gazzola et al. (2017). In this study, we employed a code taken from the MATLAB library *IR Tools* (Gazzola et al., 2019).

Because the NN-FCGLS method enforces a nonnegativity constraint at each iteration, we consider that this algorithm will produce a more accurate approximate solution when the output from the CSEM inversion is a true nonnegative (i.e., log(ρ) and the resistivity ρ is bounded by $\rho \ge 1$ Ohm-m) like in this case. The proposed deblurring approach is based on PSFs extracted from the resolution matrix associated with a linearized approximation of the original nonlinear problem. Thus, this procedure does not represent an exact solution to the blurring problem and the results obtained should always be treated with caution.

3.5 Blind deconvolution as a benchmark method

No precalculated PSFs are needed for blind deconvolution. This implies that the blur matrix $\mathbf{A}$ is now unknown, and the blind deconvolution technique estimates both the PSFs and the unknown “true” image $\mathbf{m}$ (Ayers and Dainty, 1988; Krishnamurthy et al., 1995; Holmes et al., 2006). To solve this joint problem in an efficient manner, the maximum likelihood estimation (MLE) principle is employed (van Trees, 1968). The main idea is to search for a statistical solution that maximizes the likelihood function, given some observations. Thus, the parameter values obtained (i.e., PSF and $\mathbf{m}$) are most likely to lead to the observed data. For more details, the reader is referred to Krishnamurthy et al. (1995) and Biggs and Andrews (1997).

In this paper, we applied blind deconvolution to benchmark our proposed approach, using the MATLAB routine *deconvblind*.

4 Data demonstrations

4.1 Wisting oil field

The Wisting oil field is located in the southwestern Barents Sea. The reservoir is highly segmented and very shallow (approximately 250 m below the seafloor), and contains oil in sandstone from the late Triassic (Fruholmen Formation) and early Jurassic (Nordmela and Stø Formations) periods.

In this Chapter, we start by considering an idealized model of the Wisting field that can serve as a complex controlled-data case. Such a synthetic data set is vital to perform quality control in the proposed deblurring approach. The controlled-data example is then followed by a case where CSEM field data acquired across the Wisting field is employed.

4.2 Complex synthetic model

Figure 7 shows a plot of the synthetic model color-coded with vertical resistivity. Although the model includes anisotropy in most layers, we focus here on vertical resistivity because the CSEM method is known to be most sensitive to this polarization. For more details about the construction of the synthetic model, the reader is referred to Thorkildsen and Gelius (2023). Synthetic marine CSEM data were generated using the model shown in Figure 7, employing the MARE2DEM package in a forward-modeling mode. Five receivers evenly deployed on the seafloor at a 3000m interval were used for the calculations. On the transmitter side, approximately 180 source positions were simulated using a spatial sample interval of around 200m. Moreover, a total of 11 frequencies ranging from 0.2 to 12 Hz were included. Random noise with a standard deviation equal to 1% of the data amplitude was added to each recording.

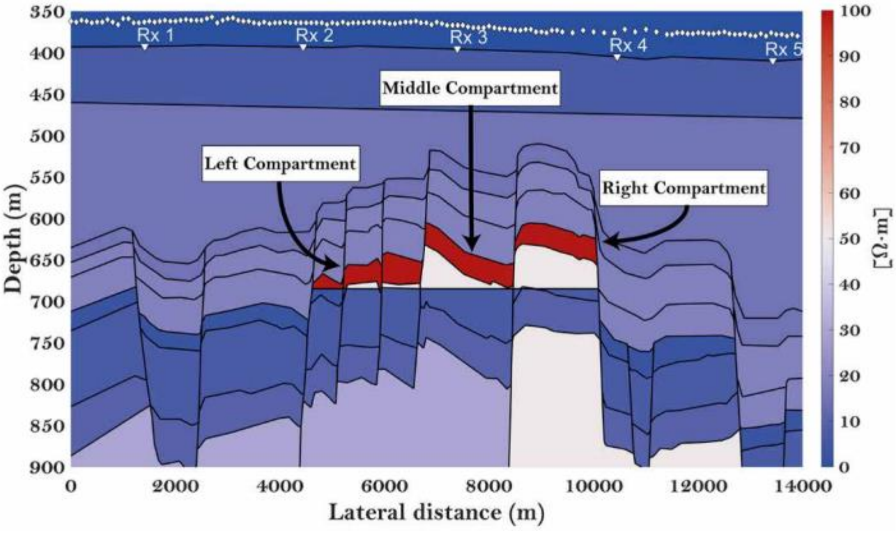

***Figure 7**: 2D synthetic model color-coded with vertical resistivity.*

The blurred model obtained from the CSEM inversion is displayed in Figure 8a. The inversion was characterized by a smooth transition from the low resistivity background to the high resistivity inside the reservoir. During the inversion, we constrained the model update to a rectangular area enclosing the main reservoir, while keeping the rest of the model unchanged. We also employed a vertical sample interval of 5 m, which is denser than that normally employed in CSEM inversion. This was performed to enhance the deblurring effect from a visualization point of view. When compared to the “true” model in Figure 7, the inversion was able to reproduce the main features of the reservoir. However, the main resistive structure was too shallow for both the left and (parts of) the middle compartment. The white vertical lines introduced in Figure 8a indicate the borders between the different subregions employed when constructing the space-variant blur matrix **A** (transition zones not shown). In addition, ideal PSFs were introduced along the red frame surrounding the target region to constrain the outer parts of the image. An ideal PSF is a point-spread function that takes the value of 1 at the corresponding parameter location and 0 elsewhere.

If we employ the proposed deblurring approach, we generally expect to observe *a better-resolved reservoir along the vertical direction (i.e., thinner)*. A direct comparison between the output from the CSEM inversion (Figure 8a) and the corresponding deblurred image obtained from NN-FCGLS (Figure 8b) supports this assumption. A total of six PSFs were employed during deconvolution (their actual locations are represented by the superimposed green dots in Figure 8). After deblurring, the target structure appeared thinner overall and the right compartment showed the greatest change in resolution. This was also expected because that part of the reservoir is known to be the most poorly resolved. On the other hand, the result of blind deconvolution (Figure 8c) exhibited no resolution enhancement but rather the opposite. Note, however, that the blind deconvolution technique applied can only handle the case of a space-invariant (*and unknown*) PSF.

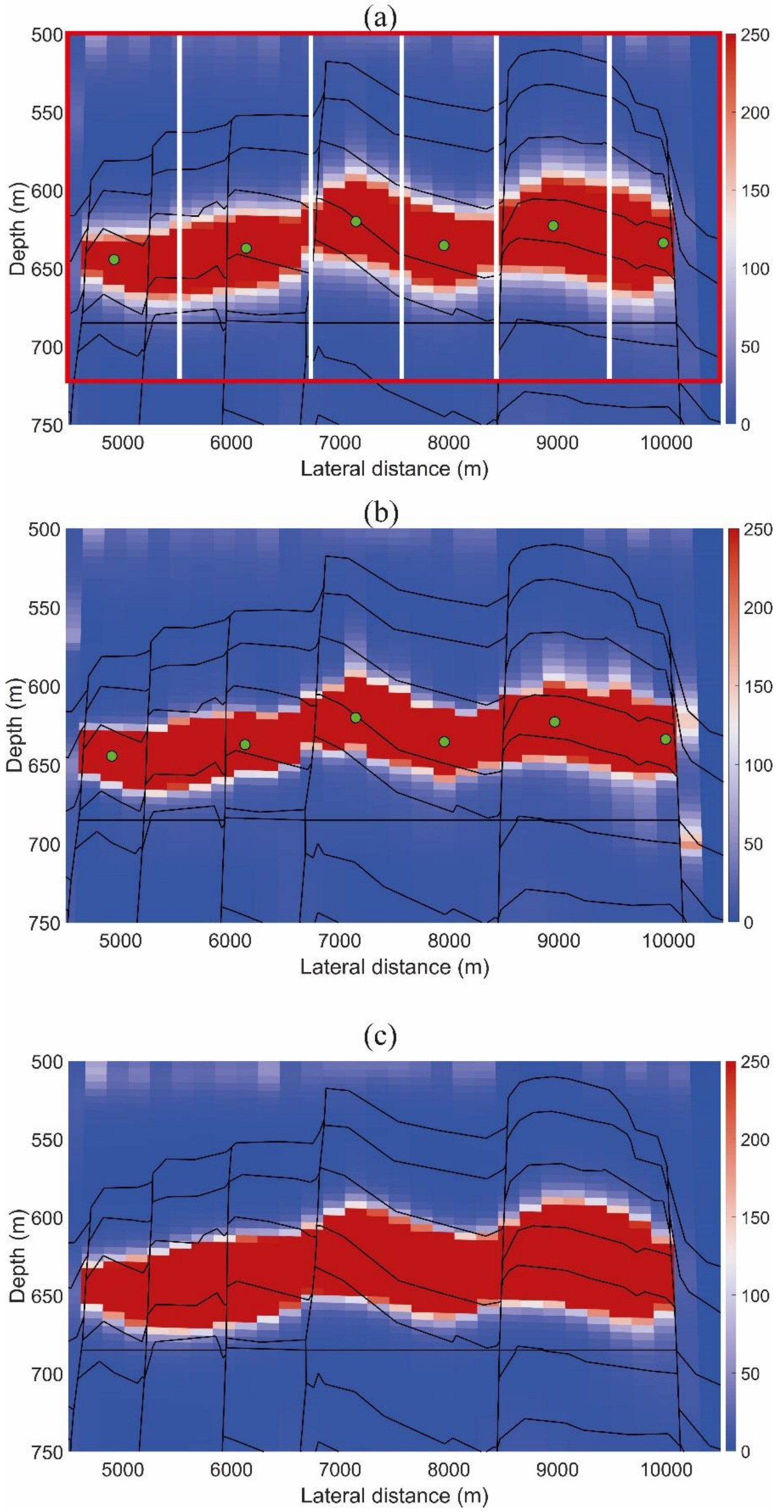

***Figure 8**: (a) Blurred output from CSEM inversion of data generated in the complex synthetic model shown in Figure 7. The white vertical lines introduced indicate the borders between the different subregions employed when constructing the space-variant blur matrix. (b) Deblurred model obtained from NN-FCGLS after 12 iterations. (c) Output from blind deconvolution. Color scale between 0 and 250 Ohm-m resistivity.*

4.3 CSEM field data

To demonstrate the effectiveness of the proposed method on field data, the proposed deblurring approach was applied to a 2D CSEM line extracted from the BSMC08W 3D survey acquired across the Wisting oil field during the summer of 2008 (with similar acquisition parameters as in the synthetic model case). We used data corresponding to a frequency range of 0.2 to 12 Hz (total of 23 frequencies) as the input for the CSEM inversion.

Figure 9a shows the blurred model obtained from an unconstrained CSEM inversion. This result was achieved after cubic interpolation of the originally coarser output grid resulting from MARE2DEM. This coarser inversion grid was sampled at 200 m laterally and 30 m vertically and was chosen in collaboration with the industry to ensure a reasonable computational time. However, the interpolated grid was sampled at 50 m laterally and 5 m vertically. Resampling of the image (and also selected PSFs) was performed to ensure that the deblurring step would be stable (otherwise, very few grid points would define both the blurred image and the corresponding PSFs). Figures 9a through c show superimposed arrows indicating an estimate of the average reservoir thickness (about 40 m).

Figure 9b displays the deblurred image obtained after six iterations of the NN-FCGLS method. A total of three carefully selected PSFs were employed during deconvolution (their actual locations are represented by the superimposed green dots in Figure 9). The overall effect of deconvolution is that the reservoir has become thinner and with sharper boundaries. In addition, the right portion of the reservoir, which was more poorly resolved, appears slightly uplifted. Due to the coarse sampling of the original inversion grid and the fact that Wisting is a thin reservoir, this field data example represents a limiting case. However, the vertical resolution of the deblurred image has still improved and is now closer to the known average reservoir thickness. Thus demonstrating the potential of the proposed method. By directly comparing the deblurred or deconvolved result (Figure 9b) with the result obtained through blind deconvolution (Figure 9c), it is clear that the latter technique does a poor job of deblurring. Employing blind deconvolution actually produces a less resolved image than the original input.

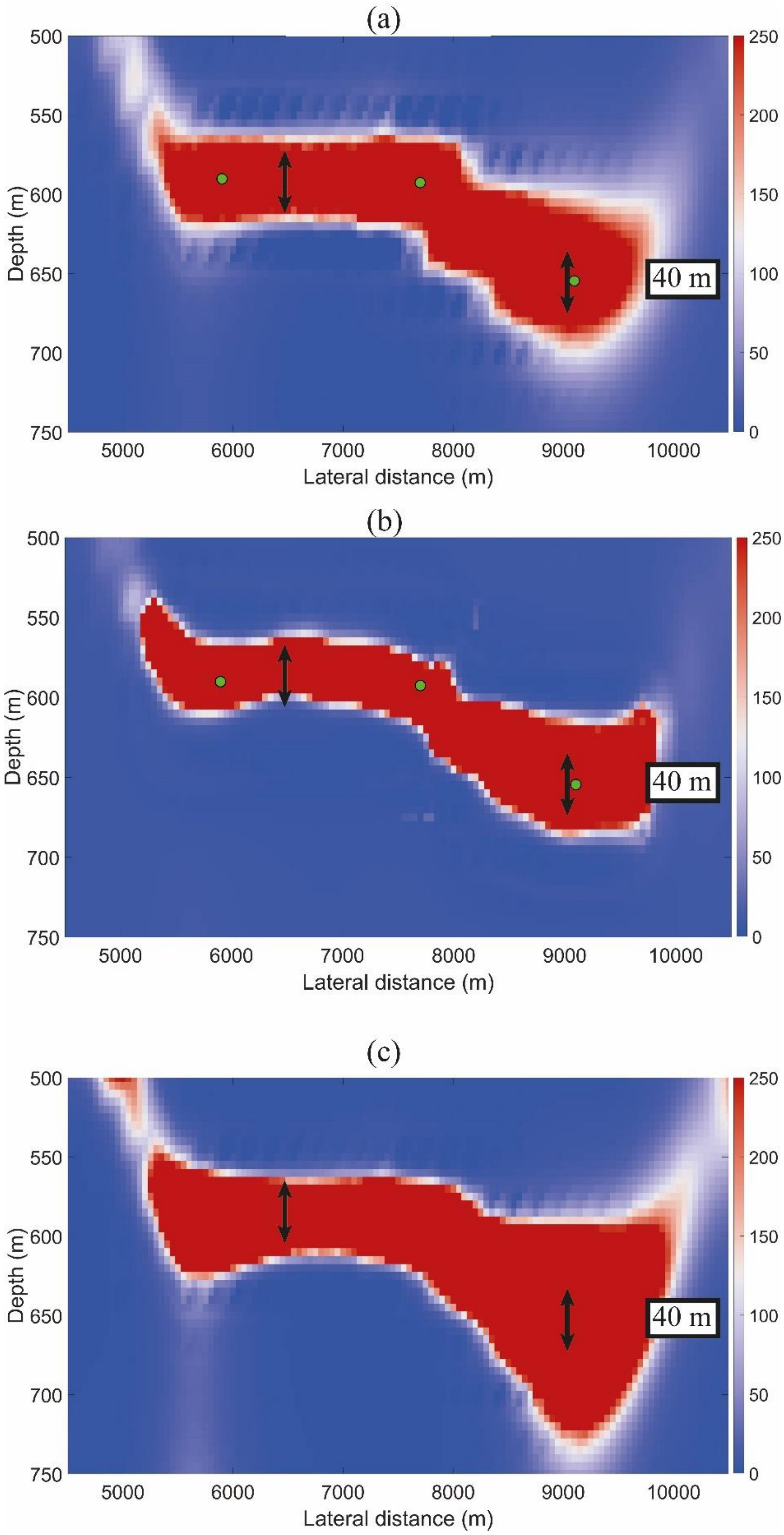

Figure 9*: (a) Blurred output from the CSEM inversion of field data. (b) Deblurred model obtained from NN-FCGLS after six iterations. (c) Output from blind deconvolution. Color scale between 0 and 250 Ohm-m resistivity.*

5 Discussion and conclusions

Here, we investigated the feasibility of applying deblurring as a post-processing technique to enhance the resolution of the model output from a CSEM inversion. We developed a portfolio of supporting software for extracting the model resolution matrix associated with the CSEM inversion (MARE2DEM) and built the corresponding blur matrix, which can be used to correct the blurring described by the space-invariant PSFs. The actual deblurring was carried out using the nonnegative flexible gradient least-squares (NN-FCGLS) algorithm. Applications to both synthetic and field data demonstrated the potential of the proposed approach. Blind deconvolution was employed as a benchmark method and was shown to perform much poorer when applied to the same two data sets.

CSEM inversion is rather computer-intensive. For the data examples shown here, the inversion typically took several days to complete (within a 1% RMS error). Deblurring, on the other hand, is a very fast technique. The combined process of constructing the space-variant blur matrix $\mathbf{A}$ and running the actual deblurring was typically completed within minutes. Thus, repeated deblurring using different PSF choices is feasible.

Future work should address the optimal choice of PSFs for a given problem, and investigate further challenges associated with iterative convergence and the particular choice of inversion algorithm.

6 Author contributions

VS-T: methodology, construction of the Wisting synthetic model, inversion of CSEM synthetic and field data, calculation of the resolution matrix and PSFs, and manuscript writing. LJ-G: concepts and methodology, manuscript writing, and revision.

7 Funding

This work was funded by the Research Centre for Arctic Petroleum Exploration (ARCEX) and the Norwegian Research Council (project number 228107).

8 Acknowledgments

The authors acknowledge EMGS ASA for providing the field data and Dr. Kerry Key for making the MARE2DEM package publicly available. The authors would also like to thank Silvia Gazzola, Per Christian Hansen, and James G. Nagy for making their software library IR Tools open access.

9 Conflict of interest

Both authors declare that the research was conducted in the absence of any commercial or financial relationships that could be construed as a potential conflict of interest.

10 References

Alumbaugh, D. L., and Newman, G. A. (2000). Image appraisal for 2-D and 3-D electromagnetic inversion. *Geophysics*, **65(5)**, 1455–1467.

Ayers, G. R., and Dainty, J. C. (1988). Iterative blind deconvolution method and its applications. *Optics Letters*, **506 13(7)**, 547–549.

Biggs, D. S., and Andrews, M. (1997). Acceleration of iterative image restoration algorithms. *Applied Optics*, **530 36(8)**, 1766–1775.

Bjørke, A.K., Hansen, K.R., and Morten, J.P. (2020). Recovering stratigraphy orientation using TTI 3D CSEM Gauss-Newton inversion. *SEG Technical Program Expanded Abstracts*: 560–564.

Brown, V., Hoversten, M., Key, K., and Chen, J. (2012). Resolution of reservoir scale electrical anisotropy from marine CSEM data. *Geophysics,* **77(2)**, E147–E158.

Chrapkiewicz, K., Wilde-Piórko, M., Polkowski, M., and Grad, M. (2020). Reliable workflow for inversion of seismic receiver function and surface wave dispersion data: A “13 BB Star” case study. *Journal of Seismology*, **548 24(1)**, 101–120.

Constable, S.C. (2010). Ten years of marine CSEM for hydrocarbon exploration. *Geophysics*, **75(5)**, 75A67–75A81.

Constable, S.C., Parker, R.L., and Constable, C.G. (1987). Occam’s inversion: A practical algorithm for generating smooth models from electromagnetic sounding data. *Geophysics,* **52(3),** 289–300.

Ellingsrud, S., Eidesmo, T., Johansen, S., Sinha, M. C., MacGregor, L. M., and Constable, S. (2002). Remote sensing of hydrocarbon layers by seabed logging (SBL): Results from a cruise offshore Angola. *The Leading Edge,* **21(10)**, 972–982.

Fichtner, A., and Leeuwen, T. V. (2015). Resolution analysis by random probing. *Journal of Geophysical Research: Solid Earth,* **120(8)**, 5549–5573.

Friedel, S. (2003). Resolution, stability and efficiency of resistivity tomography estimated from a generalized inverse approach. *Geophysical Journal International*, **153(2),** 305–316.

Gazzola, S., Hansen, P.C., and Nagy, J.G. (2019). IR Tools: A MATLAB package of iterative regularization methods and large-scale test problems. *Numer Algor,* **81**, 773–811.

Gazzola, S., and Wiaux, Y. (2017). Fast nonnegative least squares through flexible Krylov subspaces. *SIAM Journal on Scientific Computing,* **39(2)**, A655–A679.

Grayver, A. V., Streich, R., and Ritter, O. (2014). 3D inversion and resolution analysis of land-based CSEM data from the Ketzin CO_2 storage formation. *Geophysics,* **79(2),** E101–E114.

Hansen, P.C., Nagy, J.G., and O’Leary, D.P. (2006). *Deblurring Images. Matrices, Spectra and Filtering.* Society for Industrial and Applied Mathematics (SIAM).

Holmes, T. J., Biggs, D., and Abu-Tarif, A. (2006). Blind deconvolution. In *Handbook of Biological Confocal Microscopy* (pp. 468–487). Springer, Boston, MA.

Hu, J., Schuster, G.T, and Valasek, P.A. (2001). Poststack migration deconvolution. *Geophysics*, **66(3),** 939–952.

Jackson, D. D. (1972). Interpretation of inaccurate, insufficient and inconsistent data. *Geophysical Journal International*, **28(2)**, 97–109.

Jakobsen, M., and Tveit, S. (2018). Distorted born iterative T-matrix method for inversion of CSEM data in anisotropic media. *Geophysical Journal International,* **214,** 1524–1537.

Kalscheuer, T., Juanatey, M., Meqbel, N., and Pedersen, L. B. (2010). Non-linear model error and resolution properties from two-dimensional single and joint inversions of direct current resistivity and radiomagnetotelluric data. *Geophysical Journal International*, **182(3)**, 1174–1188.

Key, K. (2016). MARE2DEM: a 2-D inversion code for controlled-source electromagnetic and magnetotelluric data. *Geophysical Journal International,* **207(1),** 571–588.

Krishnamurthy, V., Liu, Y. H., Bhattacharyya, S., Turner, J. N., and Holmes, T. J. (1995). Blind deconvolution of fluorescence micrographs by maximum-likelihood estimation. *Applied Optics*, **34(29)**, 6633–6647.

Mattsson, J. (2015). Resolution and precision of resistivity models from inversion of towed streamer EM data. *SEG Technical Program Expanded Abstracts*.

Mckay, A., Mattson, J., and Du, Z. (2015). Towed streamer EM-reliable recovery of sub-surface resistivity. *First Break*, **33(4).**

Menke, W. (2012). *Geophysical Data Analysis: Discrete Inverse Theory: MATLAB edition* (Vol. 45). Academic Press.

Nagy, J. G., and O'Leary, D. P. (1997). Fast iterative image restoration with a spatially varying PSF. In *Advanced Signal Processing: Algorithms, Architectures, and Implementations* VII (Vol. 3162, pp. 388-399). SPIE.

Nguyen, A.K., Nordskag, J.I., Wiik, T., Bjørke, A.K., Boman, L., Pedersen, O.M., Ribaudo, J., and Mittet, R. (2016). Comparing large-scale 3D Gauss-Newton and BFGS CSEM inversions. *SEG Technical Program Expanded Abstracts*: 872–877.

Ren, Z., and Kalscheuer, T. (2020). Uncertainty and resolution analysis of 2D and 3D inversion models computed from geophysical electromagnetic data. *Surveys in Geophysics,* **41(1),** 47–112.

Rossmann, K. (1969). Point spread-function, line spread-function, and modulation transfer function. Tools for the study of imaging systems. *Radiology,* **93(2),** 257–272.

Routh, P. S., and Miller, C. R. (2006). Image interpretation using appraisal analysis. In *Symposium on the Application of Geophysics to Engineering and Environmental Problems* (pp. 1812–1820). Society of Exploration Geophysicists.

Røsten, T., Johnstad, S.E., Ellingsrud, E., Amundsen, H.E.F., Johansen, S., and Brevik, I. (2003). A sea bed logging (SBL) calibration survey over the Ormen Lange gas field. *EAGE Technical Program Expanded Abstracts*: P058.

Sjoeberg, T. A., Gelius, L. J., and Lecomte, I. (2003). 2-D deconvolution of seismic image blur. *SEG Technical Program Expanded Abstracts*.

Takahata, A.K., Gelius, L., Lopes, R., Tygel, M., and Lecomte, I. (2013). 2D spiking deconvolution approach to resolution enhancement of prestack depth migrated seismic images. *EAGE Technical Program Expanded Abstracts*: Th 06 07.

Thorkildsen, V.S., and Gelius, L.-J. (2023). Electromagnetic sensitivity: A CSEM study based on the Wisting oil field. To appear in *Geophysical Journal International*.

Um, E. S., and Alumbaugh, D. L. (2007). On the physics of the marine controlled-source electromagnetic method. *Geophysics,* **72(2),** WA13–WA26.

Van Trees, H.L. (1968). *Detection, Estimation and Modulation Theory (Part I).* Wiley, New York.

Wang, F., Morten, J.P., and Spitzer, K. (2018). Anisotropic three-dimensional inversion of CSEM data using finite-element techniques on unstructured grids. *Geophysical Journal International,* **213 (2),** 1056–1072.

Xu, L., Sun, W-Q., Yan, Y-H., and Zhang, W-Q. (2020). Solar image deconvolution by generative adversarial network. *Research in Astronomy and Astrophysics,* **20(11),** 170–179.

Yang, J., Huang, J., Zhu, H., McMechan, G., and Li, Z. (2022). An efficient and stable high-resolution seismic imaging method: Point-spread function deconvolution. *Journal of Geophysical Research: Solid Earth*, 127, e2021JB023281.

Yu, J., Hu, J., Schuster, G.T, and Estill, R. (2006). Prestack migration deconvolution. *Geophysics,* **71(2),** S52–S63.